



UNIVERSITEIT•STELLENBOSCH•UNIVERSITY  
jou kennisvennoot • your knowledge partner

# A Permittivity Measurement System for High Frequency Laboratories

by

Johannes Izak Frederik Marais



*Thesis presented at the University of Stellenbosch in  
partial fulfilment of the requirements for the degree of*

Master of Science in Engineering (Electronic Engineering with  
Computer Science)

Department Electrical and Electronic Engineering  
University of Stellenbosch  
Private bag X1, 7602 Matieland

Study leader: Prof. K.D. Palmer

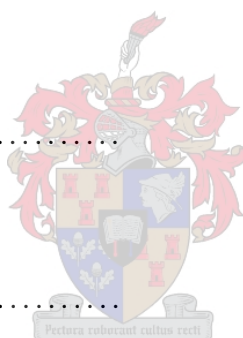
December 2006

# Declaration

I, the undersigned, hereby declare that the work contained in this thesis is my own original work and that I have not previously in its entirety or in part submitted it at any university for a degree.

Signature: .....

J.I.F. Marais



Date: .....

# Abstract

The open-ended coaxial probe is revisited as a broadband measurement system for general high frequency permittivity measurements. Three coaxial probes were developed that are suited for the measurement of both liquids and solids. The components of a permittivity measurement system were investigated and improvements were made to the coaxial probe where needed. This includes the development of a full wave code with great calculation time improvements without sacrificing accuracy. This code allows measurements to be performed in a high frequency laboratory and the permittivity extracted without any mentionable delay. A capacitance model that better describes the impedance of an open-ended coaxial line is also suggested that can be used for real-time permittivity extraction over a limited frequency range.

Calibration formed a vital part of the project and great time was spent developing a TRL and a SOLT calibration set for the coaxial probe geometry. The combination of the TRL and SOLT standards also allows measurement of the residual errors after calibration and is used in an uncertainty analysis of the extracted permittivity.

Well known materials such as PTFE, PVC, methanol and water were measured to test the probes. The measured dielectric constants are all within 3% of values quoted in literature. The loss term of the samples are also in good agreement with the expected values.

# Samevatting

Die oopgeslote koasiale probe word ondersoek as 'n wye band permitiwiteitmeetstelsel wat algemeen gebruik kan word in 'n hoë frekwensie laboratorium. Drie koaksiale probes is ontwikkel wat geskik is om beide vastestowwe en vloeistowwe te meet. Die komponente van 'n permitiwiteitmeetstelsel is ondersoek en verbeteringe is aangebring waar nodig om die koaksiale probe geskik te maak vir akkurate materiaal metings binne aanvaarbare tye. Dit sluit onder andere die ontwikkeling van 'n sagteware program in wat hoër orde modulusse in ag neem wanneer die weerkaatskoeffisiënt bereken word. Die verkorting van berekenings tye met dié kode stel die gebruiker in staat om metings in 'n laboratorium te maak en dan sonder 'n lang vertraging die materiaal eienskappe te onttrek. Die verbetering in spoed is verkry sonder om die akkuraatheid van die berekening te verlaag.

Kalibrasie van die stelsel vorm 'n groot deel van die projek. 'n SOL en 'n TRL kalibrasiestel is vir die koaksiale probe ontwikkel sodat baie akkurate metings gemaak kan word. Die kombinasie van die twee kalibrasiestelle stel ons in staat om die meet onsekerheid in die materiaal eienskappe te bepaal.

Bekende materiale, soos PTFE, PVC, metanol en water, is gemeet en vergelyk met waardes uit die literatuur. Die gemete diëlektriese konstantes verskil met minder as 3% met die van die waardes uit die literatuur. Die gemete verliese vergelyk ook baie goed met die verwagte waardes.

# Acknowledgements

There are a few people I would like to thank for their help and support. Without the following acknowledgements this thesis would not be complete.

Firstly I would like to thank Professor Palmer for his guidance, patients and enthusiasm. A special thanks also goes to Professor Reader and his friends at NIST, especially Micheal Janezic, for their help in developing and testing the full wave code that forms part of this project. Thank you to Professor van Niekerk for his advice and suggestions with respect to measurement and calibration.

Without the excellent technical staff at SED this project would not be possible. Thank you Wessel, Lincoln and Ulrich.

Thank you to Martin Siebers for your help with measurements in the Antenna Lab.

Thanks to everyone at Chemical Engineering for supplying me with measurement samples. Thanks Lafras!

To everyone in the "Molshoop", thanks for allowing me to keep you out of work. Thanks Wernich, Johnathan and Martin. A special thanks goes to Paul who has shared his knowledge and discoveries with me in the past two years. It has been fun!

Lastly, I would like to thank my friends and family. The love and support from both the Uys and Otto families have carried me through my studies. Thank you Maret for your everlasting love and encouragement. Your assistance in proofreading this thesis is greatly appreciated.

# Contents

<b>Declaration</b>	<b>ii</b>
<b>Abstract</b>	<b>iii</b>
<b>Samevatting</b>	<b>iv</b>
<b>Acknowledgements</b>	<b>v</b>
<b>Contents</b>	<b>vi</b>
<b>List of Figures</b>	<b>ix</b>
<b>List of Tables</b>	<b>xiv</b>
<b>Abbreviations and Symbols</b>	<b>xv</b>
<b>1 Introduction</b>	<b>1</b>
1.1 Thesis layout . . . . .	1
<b>2 Theory</b>	<b>3</b>
2.1 Electromagnetic Wave Propagation . . . . .	3
2.2 Material descriptions and notations . . . . .	6
2.2.1 Complex permittivity . . . . .	6
2.2.2 Conductivity . . . . .	9
2.3 Dielectric Modelling . . . . .	11
2.3.1 Lorentz resonances . . . . .	12
2.3.2 Debye relaxation . . . . .	12
2.3.3 Cole-Cole . . . . .	13
2.3.4 Cole-Davidson . . . . .	13
2.3.5 Havriliak-Negami . . . . .	14
2.3.6 Power series . . . . .	15
2.4 Conclusion . . . . .	15



<b>3</b>	<b>Permittivity measurement systems</b>	<b>16</b>
3.1	Permittivity measurement techniques . . . . .	17
3.1.1	Transmission lines . . . . .	18
3.1.2	Capacitive plates . . . . .	19
3.1.3	Resonant structures . . . . .	19
3.1.4	Free space measurements . . . . .	20
3.1.5	Coaxial probes . . . . .	20
3.2	Extracting material properties from reflection measurement . . . . .	23
3.2.1	Direct inversion . . . . .	24
3.2.2	Indirect inversion . . . . .	25
3.3	Flat flanged coaxial probes . . . . .	27
3.3.1	Calculating the reflection coefficient . . . . .	28
3.3.2	Simplified equivalent models . . . . .	36
3.3.3	Extracting permittivity . . . . .	42
3.4	Probe with extruding centre pin . . . . .	43
3.4.1	Calculating the reflection coefficient . . . . .	44
3.4.2	Equivalent circuit model . . . . .	45
3.4.3	Extracting permittivity . . . . .	46
3.5	Conclusion . . . . .	47
<b>4</b>	<b>Design</b>	<b>49</b>
4.1	Probe sensitivity . . . . .	49
4.2	Sources of measurement error . . . . .	52
4.2.1	Frequency range . . . . .	52
4.2.2	Finite ground . . . . .	55
4.2.3	Finite sample size . . . . .	55
4.2.4	Lift-off & surface roughness . . . . .	58
4.3	Design & Construction . . . . .	60
4.4	Conclusion . . . . .	62
<b>5</b>	<b>Calibration</b>	<b>63</b>
5.1	Calibration . . . . .	63
5.2	SOLT Calibration and Standards . . . . .	65
5.2.1	Specifying SOL calibration standards for 8510c VNA . . . . .	66
5.2.2	Two-tier SOL calibration . . . . .	67
5.2.3	SOL standards . . . . .	69
5.3	TRL Calibration and Standards . . . . .	74
5.3.1	TRL standards . . . . .	75
5.4	Alternative calibration procedures . . . . .	78
5.5	Calibration repeatability and verification . . . . .	79
5.5.1	Repeatability . . . . .	80
5.5.2	Verification . . . . .	80
5.6	Uncertainty and Accuracy . . . . .	84
5.6.1	Measurement uncertainty . . . . .	84

5.6.2	Measurement error due to incorrect calibration . . . . .	85
5.7	Conclusion . . . . .	87
<b>6</b>	<b>Measurement</b>	<b>89</b>
6.1	Measured Samples . . . . .	89
6.1.1	Solids . . . . .	90
6.1.2	Liquids . . . . .	91
6.2	SMA-Probe . . . . .	92
6.2.1	Solids . . . . .	92
6.2.2	Liquids . . . . .	93
6.3	N-Probe . . . . .	97
6.3.1	Solids . . . . .	97
6.3.2	Liquids . . . . .	98
6.4	7/16-Probe . . . . .	102
6.4.1	Solids . . . . .	102
6.4.2	Liquids . . . . .	106
6.5	7/16-Probe with extended centre pin . . . . .	106
6.6	Conclusion . . . . .	108
<b>7</b>	<b>Conclusion</b>	<b>113</b>
7.1	Recommendations . . . . .	114
	<b>Appendices</b>	<b>115</b>
<b>A</b>	<b>Calculations</b>	<b>116</b>
A.1	Modal analysis of a short cavity termination . . . . .	116
A.2	Reflection from a coaxial line terminating in a non-magnetic material . . .	119
A.2.1	Quasi-static solution . . . . .	119
A.3	Equations for direct permittivity extraction . . . . .	121
A.3.1	Quasi-static . . . . .	121
A.3.2	Constant fringing capacitance . . . . .	121
A.3.3	Four capacitor model . . . . .	122
A.3.4	New model . . . . .	123
<b>B</b>	<b>Tables &amp; Data</b>	<b>124</b>
B.1	Calibration Definitions . . . . .	124
B.1.1	SOL . . . . .	124
B.1.2	TRL . . . . .	124
	<b>Bibliography</b>	<b>126</b>



# List of Figures

2.1	Wave illustrating attenuation due to the loss factor. . . . .	5
2.2	Permittivity of a hypothetical material illustrating the effect of polarization. . .	7
2.3	Conductor and parameters describing resistance. . . . .	10
2.4	Argand diagram of Debye model with and without electrical conductivity. . .	13
	(a) Debye model . . . . .	13
	(b) Debye model with increasing electrical conductivity. . . . .	13
2.5	Argand diagram illustrating the character of Cole-Cole model . . . . .	14
2.6	Argand diagram illustrating the character of Cole-Davidson model. . . . .	14
3.1	Diagram of components in a permittivity measurement system. . . . .	16
3.2	Illustration of a rectangular waveguide used for material characterization. . .	19
3.3	Illustration of a parallel plate used for material characterization. . . . .	19
3.4	Illustration of a rectangular resonant cavity used for material characterization.	20
3.5	Illustration of a free space material measurement set-up. . . . .	21
3.6	Configurations used for coaxial permittivity measurements. . . . .	21
3.7	Three types of the open-ended coaxial probe . . . . .	22
3.8	Waveguide and aperture feed of a coaxial probe . . . . .	26
3.9	Illustration of iterative computer simulation . . . . .	26
3.10	Illustration of a lookup table . . . . .	27
3.11	Diagram of an open-ended coaxial line showing the probe dimensions. . . . .	28
3.12	Coaxial probe terminated with layered media. . . . .	29
3.13	Simulations of reflection coefficient of an open-ended coaxial line into air. . .	34
3.14	Simulations and calculations of the reflection coefficient of an open-ended coaxial line. . . . .	35
3.15	Capacitance of SMA size coaxial probe in air. . . . .	36
3.16	Normalized capacitance of SMA sized coaxial probe with different samples. . .	37
3.17	Diagram illustrating fringing fields of a coaxial probe. . . . .	37
3.18	Model for coaxial line. . . . .	38
3.19	Least squares fit of model with constant fringing capacitance to full-wave solution. . . . .	39
	(a) Normalized capacitance of model and correct solution. . . . .	39
	(b) Percentage error in normalized capacitance. . . . .	39

3.20	Equivalent circuit of capacitors for inhomogeneous dielectric and a open-ended coaxial line. . . . .	40
3.21	Least squares fit of model with series and parallel capacitors to full-wave solution. . . . .	40
	(a) Normalized capacitance of model and correct solution. . . . .	40
	(b) Percentage error in normalized capacitance. . . . .	40
3.22	Least squares fit of new model to full-wave solution. . . . .	41
	(a) Normalized capacitance of model and correct solution. . . . .	41
	(b) Percentage error in normalized capacitance. . . . .	41
3.23	Illustration of coaxial probe with extended centre pin showing all dimensions.	44
3.24	Simulated reflection of a 7/16-sized coaxial line with 10 mm extended centre pin using different solvers and meshing in CST. . . . .	45
	(a) Magnitude . . . . .	45
	(b) Phase . . . . .	45
3.25	Equivalent circuit using Inductor and Capacitor of an extended pin coaxial probe. . . . .	45
3.26	Least squares fit of model to the time domain simulated data from CST. . . . .	46
	(a) Capacitance of model and simulation. . . . .	46
	(b) Percentage difference in capacitance. . . . .	46
3.27	Exact and calculated real permittivity and loss factor . . . . .	47
	(a) $\epsilon_r = 4, \tan \delta = 0.1$ at 300MHz . . . . .	47
	(b) $\epsilon_r = 36, \tan \delta = 0.1$ at 100MHz . . . . .	47
4.1	Sensitivity of SMA probe at 1 GHz. . . . .	50
	(a) $S_{\epsilon_r}^{\phi}$ . . . . .	50
	(b) $S_{\tan \delta}^{\Gamma}$ . . . . .	50
4.2	Unnormalised sensitivity of SMA probe at 1 GHz. . . . .	51
	(a) $\phi S_{\epsilon_r}^{\phi}$ . . . . .	51
	(b) $\Gamma S_{\tan \delta}^{\Gamma}$ . . . . .	51
4.3	Unnormalised sensitivity of SMA probe over frequency and relative permittivity. . . . .	52
	(a) $S_{\epsilon_r}^{\phi}$ . . . . .	52
	(b) $S_{\tan \delta}^{\Gamma}$ . . . . .	52
4.4	Illustration of radiated energy in finite size sample. . . . .	53
4.5	Simulated phase measurements for different probe sizes and configurations. . . . .	54
4.6	Change in impedance of a small monopole antenna immersed in water at 2.45 GHz as a function of ground radius. . . . .	55
4.7	Illustration of minimum sample size for accurate measurements. . . . .	56
	(a) Flat flanged probe . . . . .	56
	(b) Extended pin probe . . . . .	56
4.8	Calculated permittivity and loss factor for MUT with different radii. . . . .	57
	(a) $\epsilon_r = 4$ and $\tan \delta = 0$ . . . . .	57
	(b) $\epsilon_r = 36$ and $\tan \delta = 0$ . . . . .	57

4.9	The calculated permittivity and loss factor for MUT with changing height. . . . .	57
	(a) $\epsilon_r = 4$ and $\tan \delta = 0$ . . . . .	57
	(b) $\epsilon_r = 36$ and $\tan \delta = 0$ . . . . .	57
4.10	Illustration of lift-off. . . . .	58
4.11	Effect of lift-off on extracted permittivity for two sample materials. . . . .	59
	(a) $\epsilon^* = 2(1 - 0.01i)$ . . . . .	59
	(b) $\epsilon^* = 10(1 - 0.01i)$ . . . . .	59
4.12	Measured surface profiles of the SMA and N-probe. . . . .	60
	(a) SMA-probe. . . . .	60
	(b) N-probe. . . . .	60
4.13	Measured surface profile of 7/16 probe. . . . .	60
4.14	Photograph of coaxial probes and the supporting mechanical jig. . . . .	61
5.1	Graphical representation of a calibration model where all errors are lumped together in error boxes. . . . .	64
5.2	Graphical representation of a shifted measurement plane. . . . .	65
5.3	Smith-chart showing the position of the SHORT, OPEN and LOAD standards. . . . .	66
5.4	Error model of an one-port system. . . . .	68
5.5	Photograph of coaxial probe standards used for SOL calibration. . . . .	69
5.6	Illustration of probe with cylindrical OPEN standard. . . . .	70
5.7	Measured response of OPEN standard compared to calculated response. . . . .	71
	(a) Magnitude . . . . .	71
	(b) Phase . . . . .	71
5.8	Illustration of probe with SHORT standard. . . . .	72
5.9	Measured response of SHORT standard compared to ideal response. . . . .	72
	(a) Magnitude . . . . .	72
	(b) Phase . . . . .	72
5.10	Illustration of LOAD standards. . . . .	74
	(a) Matching dimensions. . . . .	74
	(b) Mismatched dimensions. . . . .	74
5.11	Reflection from SMA LOAD standard. . . . .	74
	(a) Magnitude . . . . .	74
	(b) Smith-chart . . . . .	74
5.12	Illustration of probes forming the THRU standard. . . . .	76
5.13	Time and frequency domain response of the THRU standard. . . . .	76
	(a) Time domain reflection from THRU connection. . . . .	76
	(b) Frequency domain response of gated THRU. . . . .	76
5.14	Frequency response of SMA transition. . . . .	77
5.15	Illustration of probes with the REFLECT standard. . . . .	78
5.16	Illustration of probes with the LINE standard. . . . .	79
5.17	Time domain response of the LINE standard. . . . .	79
5.18	Other ways to calibrate. . . . .	80
5.19	Measured repeatability of SMA coaxial probe using the LOAD standard. . . . .	81
5.20	Residual directivity error. . . . .	83

(a)	Illustration. . . . .	83
(b)	Measured residual directivity for SOL and TRL calibration. . . . .	83
5.21	Residual source match error measurement. . . . .	83
(a)	Residual source match vector. . . . .	83
(b)	Example measurement. . . . .	83
5.22	Measured residual error for SOL and TRL calibration. . . . .	84
5.23	Circle of uncertainty for uncertainty of -20dB, -30dB and -40dB. . . . .	86
(a)	Uncertainty on the Smith-chart. . . . .	86
(b)	Enlarged Smith-chart. . . . .	86
5.24	Diagram illustrating how the magnitude uncertainty is calculated. . . . .	86
5.25	Diagram illustrating how the phase uncertainty is calculated. . . . .	87
6.1	Measured permittivity of PTFE using the SMA-probe. . . . .	93
6.2	Measured permittivity of PVC using the SMA-probe. . . . .	94
6.3	Measured permittivity of Polyester using the SMA-probe. . . . .	94
6.4	Measured permittivity of PVDF using the SMA-probe. . . . .	95
6.5	Measured permittivity of Methyl alcohol using the SMA-probe. (a) Measured, (b) Uncertainty, (c) Grant[1], (d) Belhadj-Tahar[2], (e) Jordan[3]. . . . .	96
6.6	Argand diagram of the measured permittivity of Methyl alcohol using the SMA-probe. (a) Measured, (b) Uncertainty, (c) Grant[1], (d) Belhadj-Tahar[2], (e) Jordan[3]. . . . .	97
6.7	Measured permittivity of water over from 100 MHz to 8 GHz using the SMA- probe. (a) Measured, (b) Uncertainty bars, (c) Cole-Cole model form literature at 15 °C, (d) 20 °C, (e) 25 °C. . . . .	98
6.8	Measured permittivity of water form 100 MHz to 3 GHz using the SMA- probe. (a) Measured, (b) Uncertainty bars, (c) Cole-Cole model form literature at 15 °C, (d) 20 °C, (e) 25 °C. . . . .	99
6.9	Measured permittivity of PTFE using the N-probe . . . . .	100
6.10	Measured permittivity of PVC using the N-probe . . . . .	100
6.11	Measured permittivity of Polyester using the N-probe . . . . .	101
6.12	Measured permittivity of PVDF using the N-probe . . . . .	101
6.13	Measured permittivity of Methyl alcohol using the N-probe. (a) Measured, (b) Grant[1], (c) Belhadj-Tahar[2], (d) Jordan[3]. . . . .	102
6.14	Argand diagram of the measured permittivity of Methyl alcohol using the N-probe. (a) Measured, (b) Grant[1], (c) Belhadj-Tahar[2], (d) Jordan[3]. . . . .	103
6.15	Measured permittivity of water from 100 MHz to 6 GHz using the N-probe. (a) Measured, (b) Cole-Cole model form literature at 15 °C, (c) 20 °C, (d) 25 °C. . . . .	103
6.16	Measured permittivity of water from 100 MHz to 3 GHz using the N-probe. (a) Measured, (b) Cole-Cole model form literature at 15 °C, (c) 20 °C, (d) 25 °C. . . . .	104
6.17	Measured permittivity of PVC using the 716 probe . . . . .	104
6.18	Measured permittivity of Polyester using the 716 probe. . . . .	105
6.19	Measured permittivity of PVDF using the 716 probe. . . . .	105
6.20	Measured permittivity of Methyl alcohol using the 7/16-probe. (a) Measured, (b) Grant[1], (c) Belhadj-Tahar[2], (d) Jordan[3]. . . . .	106

6.21 Argand diagram of the measured permittivity of Methyl alcohol using the 7/16-probe. (a) Measured, (b) Grant[1], (c) Belhadj-Tahar[2], (d) Jordan[3]. . . 107

6.22 Measured permittivity of water form 130 MHz to 3 GHz using the 7/16-probe. (a) Measured, (b) Cole-Cole model form literature at 15 °C, (c) 20 °C, (d) 25 °C. 107

6.23 Measured permittivity of water from 130 MHz to 300 MHz using the 7/16-probe. (a) Measured, (b) Cole-Cole model form literature at 15 °C, (c) 20 °C, (d) 25 °C. . . . . 108

6.24 Measured permittivity of air using the 7/16 probe with extended centre pin. . 109

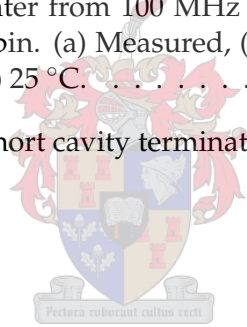
6.25 Measured permittivity of Methyl alcohol from 100 MHz to 1.5 GHz using the 7/16-probe with extended centre pin. (a) Measured, (b) Grant[1], (c) Belhadj-Tahar[2], (d) Jordan[3]. . . . . 109

6.26 Measured permittivity of Methyl alcohol from 100 MHz to 500 MHz using the 7/16-probe with extended centre pin. (a) Measured, (b) Grant[1], (c) Belhadj-Tahar[2], (d) Jordan[3]. . . . . 110

6.27 Measured permittivity of water from 100 MHz to 3 GHz using the 7/16-probe with extended centre pin. (a) Measured, (b) Cole-Cole model form literature at 15 °C, (c) 20 °C, (d) 25 °C. . . . . 111

6.28 Measured permittivity of water from 100 MHz to 300 MHz using the 7/16-probe with extended centre pin. (a) Measured, (b) Cole-Cole model form literature at 15 °C, (c) 20 °C, (d) 25 °C. . . . . 112

A.1 Illustration of probe with a short cavity termination. . . . . 116



# List of Tables

1	List of symbols representing order of magnitude . . . . .	xv
2	List of abbreviations . . . . .	xv
3.1	Calculation times for NIST permittivity extraction code. . . . .	29
3.2	Calculation time of quasi-static solution by Misra. . . . .	30
3.3	Calculation time of full-wave solution by Mosig. . . . .	34
3.4	Calculation times for NIST permittivity extraction code. . . . .	42
3.5	Calculation times for full wave secant permittivity extraction. . . . .	43
3.6	Element values for equivalent circuit model of pin extended probe. . . . .	47
4.1	Probe dimensions. . . . .	62
4.2	Frequency ranges in air. . . . .	62
6.1	Permittivity of solid samples quoted in literature . . . . .	90
6.2	Permittivity of liquid samples quoted in literature . . . . .	91
6.3	Measured average permittivity of solid samples (SMA-probe). . . . .	93
6.4	Measured Debye model parameters of liquid samples (SMA-probe). . . . .	96
6.5	Measured average permittivity of solid samples (N-probe). . . . .	99
6.6	Measured Debye model parameters of liquid samples (N-probe). . . . .	102
A.1	Coefficients used to approximate the elliptic integral of the first kind. . . . .	120
B.1	SOL Calibration Definitions for 8510c VNA . . . . .	125

# Abbreviations and Symbols

**Table 1:** List of symbols representing order of magnitude

Symbol	Name	Value	Symbol	Name	Value
a	atto	$10^{-18}$	k	kilo	$10^3$
f	femto	$10^{-15}$	M	Mega	$10^6$
p	piko	$10^{-12}$	G	Giga	$10^9$
n	nano	$10^{-9}$	T	Tera	$10^{12}$
$\mu$	mikro	$10^{-6}$	P	Peta	$10^{15}$
m	milli	$10^{-3}$	E	Exa	$10^{18}$

**Table 2:** List of abbreviations

Abbr.	Meaning	Abbr.	Meaning
V	Volt	VNA	Vector Network Analyser
A	Ampere	SOLT	Short-Open-Load-Thru
F	Farad	TOSM	Thru-Open-Short-Match
H	Henry	TRL	Thru-Reflect-Line
m	metre	MUT	Material Under Test
dB	decibel	DUT	Device Under Test
Hz	Hertz	AMT	Antenna Modelling Theorem
$\Omega$	Ohm	TEM	Transverse Electromagnetic
DC	Direct Current	TE	Transverse Electric
AC	Alternating Current	TM	Transverse Magnetic
SMA	Standard Military Adapter	HP	Hewlett Packard
US	University of Stellenbosch	NIST	National Institute of Standards and Technology

# Chapter 1

## Introduction

This thesis presents the analysis and development of a wide band permittivity measurement system for use in a high frequency laboratory. For the probe to be useful to a large spectrum of microwave engineers, it should be able to measure a wide range of materials over a wide frequency range and require only minimum sample preparation.

The design and development of microwave devices requires knowledge of the materials. The electrical properties of these materials are often unknown and has to be measured. Many permittivity measurement systems are used, but they are generally not well suited to measure both liquids and solids. Their frequency ranges are limited and they require extensive sample preparation. There is a need for a general permittivity measurement system that can measure a range of materials over a large frequency spectrum with minimal sample preparation. The price that has to be paid to measure a large range of materials over a large frequency range is accuracy. If the permittivity can be measured with an accuracy of 5% or 10%, this should be sufficient.

### 1.1 Thesis layout

Chapter 2 starts by introducing the Maxwell field equations. Concepts and terminology is introduced to describe the interaction of electromagnetic fields with non-magnetic dielectric materials and also the effect dielectric materials have on electromagnetic fields. The origin of polarisation and the various methods used to describe the dielectric properties of materials over a large frequency range are investigated.

Chapter 3 presents the components of a permittivity measurement system and the factors that should be considered when choosing a system that is best suited for the application. Calculation of the reflection coefficient from an open-ended coaxial probe is



investigated to find an accurate, but fast computational code. Simple capacitance models are also considered for fast permittivity extraction.

Sensitivity and measurement errors due to restrictions on sample and ground plane size are discussed in chapter 4. Errors introduced through sample lift-off is also investigated. The chapter ends with a description of the probes that have been designed and built.

Chapter 5 is all about calibration, accuracy and repeatability. Two calibration methods are explored and compared to each other in terms of calibration effectiveness. The residual errors after calibration are measured and this information is used to estimate the measurement uncertainty that is later related to permittivity uncertainty.

Well known materials are measured in chapter 6 and compared to expected permittivity values found in literature. This allows the probe performance to be compared to results predicted in chapters 3 to 5.

Conclusions and recommendations are made in chapter 7 to further improve the measurement system.



# Chapter 2

## Theory

This chapter provides some background theory and concepts that will be used later in this thesis. Other concepts are presented as required. Before permittivity can be measured it is important to understand exactly what permittivity is and how it affects electromagnetic fields. Section 2.1 presents Maxwell's field equations and derives concepts such as wavelength and propagation velocity[4][5][6]. The origin and various representations of permittivity and conductivity are presented in section 2.2. This section is of particular interest since there are a few notations which can cause confusion when different sources are consulted. The chapter is concluded with a summary of dielectric models that can be used to describe material permittivity over an appreciable frequency range.



### 2.1 Electromagnetic Wave Propagation

Maxwell's equations describe the behaviour of electromagnetic fields. The differential form of Maxwell's equations in free space are given by (2.1.1), (2.1.2), (2.1.3) and (2.1.4).

$$\nabla \times \mathbf{H} = \mathbf{J} + \frac{\partial \epsilon_0 \mathbf{E}}{\partial t} \quad (2.1.1)$$

$$\nabla \times \mathbf{E} = -\frac{\partial \mu_0 \mathbf{H}}{\partial t} \quad (2.1.2)$$

$$\nabla \cdot \epsilon_0 \mathbf{E} = \rho \quad (2.1.3)$$

$$\nabla \cdot \mu_0 \mathbf{H} = 0 \quad (2.1.4)$$

In a polarisable medium the current density term in Ampère's law expands to include a polarisation current density,  $\mathbf{J}_p = \frac{\partial \mathbf{P}}{\partial t}$ , along with the unpolarised current density  $\mathbf{J}_u =$

$\sigma\mathbf{E}$ . Ampère's law then becomes

$$\nabla \times \mathbf{H} = \mathbf{J}_u + \mathbf{J}_p + \frac{\partial \epsilon_0 \mathbf{E}}{\partial t} \quad (2.1.5)$$

$$= \mathbf{J}_u + \frac{\partial (\mathbf{P} + \epsilon_0 \mathbf{E})}{\partial t} \quad (2.1.6)$$

$$= \mathbf{J}_u + \frac{\partial \mathbf{D}}{\partial t} \quad (2.1.7)$$

where  $\mathbf{D}$  is the electric displacement flux density. All further derivation assumes a time-harmonic excitation. The unpolarised current density is due to electrical conductivity. The loss of a dielectric may also be considered as an equivalent conductor loss called dielectric conductivity,  $\omega\epsilon''$ . The dielectric conductivity or dielectric damping is discussed further in section 2.2.2. Equation (2.1.1) can be written in general form using a complex permittivity that incorporates conductivity due to unbounded electric charges.

$$\epsilon^* = \epsilon' - j \left( \epsilon'' + \frac{\sigma_e}{\omega} \right) \quad (2.1.8)$$

$$\nabla \times \mathbf{H} = j\epsilon^* \omega \mathbf{E} \quad (2.1.9)$$

Ampère and Faraday's laws are now combined to investigate the effect permittivity has on the propagation of electromagnetic waves in a non-magnetic material. The propagation of a wave in an unbounded medium is found by eliminating either the magnetic or electric field in (2.1.9) and (2.1.2). The magnetic field has been eliminated here and the resulting wave equation is given by (2.1.10).

$$\nabla^2 \mathbf{E} = -\epsilon^* \mu_0 \omega^2 \mathbf{E} \quad (2.1.10)$$

For a wave propagating in the positive  $z$ -direction the wave equation can be simplified to (2.1.11).

$$\frac{\partial^2 \mathbf{E}}{\partial z^2} = -\epsilon^* \mu_0 \omega^2 \mathbf{E} \quad (2.1.11)$$

The solution to (2.1.11) for a plane wave travelling in the positive  $z$ -direction with a radial frequency  $\omega$ , where  $\omega = 2\pi f$ , is given by (2.1.12). The propagation of the wave is described by the complex propagation factor  $\gamma^*$  which is easily related to the complex

permittivity of the medium.

$$\mathbf{E} = E_0 e^{j\omega t - \gamma^* z} = E_0 e^{-\alpha z} e^{j(\omega t - \beta z)} \quad (2.1.12)$$

$$\gamma^* = \alpha + j\beta = j\omega \sqrt{\epsilon^* \mu_0} \quad (2.1.13)$$

The real and imaginary parts of  $\gamma^*$  are known as the attenuation factor,  $\alpha$ , and the phase factor,  $\beta$ , respectively. Figure 2.1 shows the effect of the attenuation factor on the propagating electromagnetic wave.

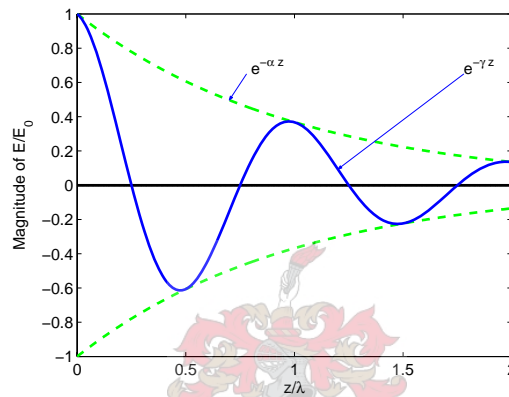


Figure 2.1: Wave illustrating attenuation due to the loss factor.

It is seen from (2.1.12) that electromagnetic waves propagate through an unbounded medium defined by  $\epsilon^*$  with a complex velocity  $v^* = \frac{1}{\sqrt{\epsilon^* \mu_0}}$ . The ratio of the complex velocity of a wave to the velocity of a wave in vacuum ( $c = \frac{1}{\sqrt{\epsilon_0 \mu_0}}$ ) is defined as the complex index of refraction ( $n$ ).

$$n^* = \frac{c}{v^*} = \sqrt{\frac{\epsilon^* \mu_0}{\epsilon_0 \mu_0}} = \sqrt{\frac{\epsilon^*}{\epsilon_0}} \quad (2.1.14)$$

A related parameter that is often used in the literature is the wavenumber,  $k$ . The wavenumber is easily related to the propagation factor. This relationship is given by (2.1.15).

$$k = \frac{\gamma^*}{j} = \beta - j\alpha \quad (2.1.15)$$

The wavelength is defined as the distance that a wave propagates in one period. It is seen from (2.1.12) that the wave has a wavelength which is given by (2.1.16). This is done

by noting that the exponential function repeats every  $2\pi$ .

$$\lambda = \frac{2\pi}{\beta} \quad (2.1.16)$$

The phase velocity is given by (2.1.17). The phase velocity can also be written in terms of the wavelength and frequency as seen in (2.1.17).

$$v = \frac{dz}{dt} = \frac{\omega}{\beta} = \lambda f \quad (2.1.17)$$

## 2.2 Material descriptions and notations

The electrical properties of materials are described using a complex permittivity and electrical conductivity. This section will also look at the definitions of permittivity, electrical and dielectric conductivity. The frequency dependence of these parameters, as well as the relationship between the parameters, are discussed. Further details on this topic can be found in [6, p. 26]

### 2.2.1 Complex permittivity, $\epsilon^*$

When an electric field is applied to a material, the material reacts to the applied field. Different materials react in different ways and through a variety of mechanisms. Permittivity describes this reaction of the bound electrons of the material to an applied electric field. The polarisation density term in (2.1.5) can be written in terms of a molecular polarisation ( $\alpha_T$ ). Molecular polarisation describes the polarisation of each individual molecule.

$$\mathbf{P} = \epsilon_0 \chi_e \mathbf{E} = N \alpha_T \mathbf{E}_{loc} = N \alpha_T g \mathbf{E} \quad (2.2.1)$$

where  $N$  is the number of molecules and  $g$  is the ratio between the local and applied electric field [7]. The applied and local field may differ due to the effect of surrounding molecules. If the molecules are well separated and do not interact with each other,  $g$  is unity. Molecular polarisation is an effect of several different mechanisms. These mechanisms are electronic-, ionic- and dipole polarization.

$$\alpha_T = \alpha_e + \alpha_i + \alpha_d \quad (2.2.2)$$

These mechanisms are generally separated into high frequency resonances and lower frequency relaxations. Electronic and ionic polarizations are resonances. Electronic polarization,  $\alpha_e$ , is caused by the shift of the electron cloud relative to its positive nucleus.

This can be further separated by considering the effect of valence electrons in the outer electron bands and electrons in the inner electron bands. Ionic polarization,  $\alpha_i$ , is due to the displacement of positive and negative ions from their neutral positions.

Dipole polarization is a relaxation mechanism,  $\alpha_d$ . The electric field tends to align the dipoles compared to their usual random positions. Dipole movement is more viscous and this causes the polarization to be a relaxation and not a resonance (similar to an over damped mechanical system in comparison to an under damped mechanical system). Figure 2.2 illustrates the effect relaxations and resonances have on material permittivity[5].

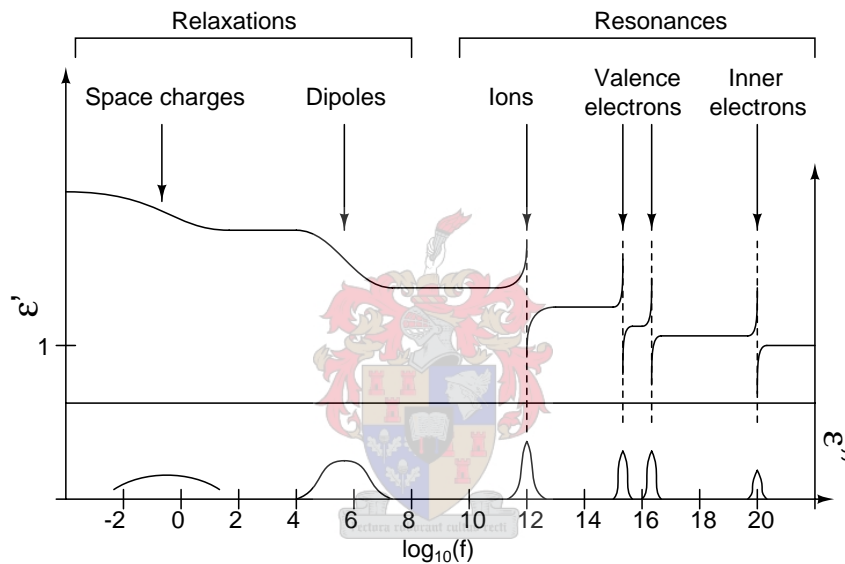


**Figure 2.2:** Permittivity of a hypothetical material illustrating the effect of polarization.

Now that the origin of polarization has been introduced, the methods which are used to describe these mechanisms can be investigated. Complex permittivity can be and has been defined in many ways in the literature. These different definitions can cause a lot of confusion when working from different sources. A good summary of terms and symbols used in the literature is given by Rimbi[8] and some of these points are repeated here to prevent possible confusion. The main difference in notation is the way that electrical conductivity is treated. It can be included with the dielectric conductivity or defined as a separate parameter. This has already been illustrated in section 2.1 when the unpolarised current density was included with the dielectric conductivity.

Complex permittivity can be defined as

$$\epsilon^* = \epsilon' - j \left( \epsilon'' + \frac{\sigma_e}{\omega} \right) \quad (2.2.3)$$

where

- $\epsilon'$  Dielectric constant
- $\epsilon''$  Dielectric loss factor
- $\sigma_e$  Electrical conductivity
- $\epsilon_0$  Dielectric constant of a vacuum

The dielectric constant,  $\epsilon'$ , is a measure of a material's ability to store electrical energy. The imaginary term in (2.2.3) represents the effective dielectric loss (heat) in the material. The effective dielectric loss is due to ohmic conduction loss as well as polarization caused by an alternating electric field in the material. Dielectric materials usually have a low electrical conductivity,  $\sigma_e$ , and it is often included in the dielectric conductivity term. The dielectric conductivity term now represents all the losses caused by any energy consuming process in the material.

$$\epsilon^* = \epsilon' - j\epsilon'' \quad (2.2.4)$$

The permittivity of a material is often normalized to the permittivity of a vacuum. The relative permittivity is defined as

$$\epsilon_r^* = \frac{\epsilon^*}{\epsilon_0} = \kappa^* = (\kappa' - j\kappa'') = (\epsilon_r' - j\epsilon_r'') \quad (2.2.5)$$

where

- $\kappa' = \epsilon_r'$  Relative dielectric constant
- $\kappa'' = \epsilon_r''$  Relative dielectric loss factor.

The complex relative permittivity can also be expressed in terms of an electric susceptibility,  $\chi_e$ . The electric susceptibility is defined as [9][10]

$$\chi_e = \epsilon_r^* - 1 \quad (2.2.6)$$

A related quantity of interest is the loss tangent, defined by [9] as

$$\tan \delta = \frac{\omega \epsilon'' + \sigma_e}{\omega \epsilon'} = \frac{\text{energy dissipated per cycle}}{\text{energy stored per cycle}} \quad (2.2.7)$$

This allows the complex permittivity to be written as in (2.2.8).

$$\epsilon^* = \epsilon_0 \epsilon_r' (1 - j \tan \delta) \quad (2.2.8)$$

### Relationship between $\epsilon'$ and $\epsilon''$

The real and imaginary parts of permittivity are not independent of one another. It can be shown that both  $\epsilon'$  and  $\epsilon''$  are described by the same decay function,  $\Phi$ [5]. For sinusoidal fields in linear media the permittivity is given by (2.2.9) and (2.2.10). These equations can be rewritten so that the decay function is the subject. It can then be substituted into the other equation to find the Kramers-Kronig relations in (2.2.11) and (2.2.12). These equations are valid for any type of dispersion. The Kramers-Kronig relations show that dispersion is an analytic necessity of causality without any physical mechanisms suggested [11]. They allow one of the parameters to be obtained provided that the other is known over the entire frequency range.

$$\epsilon'(\omega) = \epsilon_\infty + (\epsilon_s - \epsilon_\infty) \int_0^\infty \Phi(u) \cos(\omega u) du \quad (2.2.9)$$

$$\epsilon''(\omega) = (\epsilon_s - \epsilon_\infty) \int_0^\infty \Phi(u) \sin(\omega u) du \quad (2.2.10)$$

$$\epsilon'(\omega) = \epsilon_\infty + \frac{2}{\pi} \int_0^\infty \frac{x \epsilon''(x)}{x^2 - \omega^2} dx \quad (2.2.11)$$

$$\epsilon''(\omega) = \frac{2\omega}{\pi} \int_0^\infty \frac{\epsilon'(x) - \epsilon_\infty}{x^2 - \omega^2} dx \quad (2.2.12)$$

$$(2.2.13)$$

In the above equations  $\epsilon_s$  and  $\epsilon_\infty$  represent respectively the static and high frequency dielectric constant of the material.

### 2.2.2 Conductivity, $\sigma$

Electrical conductivity is a measure of the ease that free electrons can move (current) through a material under an applied force or potential gradient ( $-\frac{dV}{dx} = E$ , electric field)[12]. The geometry of a conductor can be separated from its electrical property, electrical conductivity ( $\sigma_e$ ), by defining the conductor resistance as (2.2.14). An illustration of a cylindrical conductor and its parameters is shown in Figure 2.3.

$$R = \frac{l}{\sigma_e A} \quad (2.2.14)$$



where

- $R$  Resistance of the conductor [ $\Omega$ ]
- $l$  Length of the cylindrical conductor [m]
- $A$  Area of the conductor's cross section [ $m^2$ ]
- $\sigma_e$  Electrical conductivity [ $\Omega^{-1}m^{-1}$ ]

Conductivity of a material may be the result of motion of several types of charged carriers and can be expressed as a sum of all the contributions[12].

$$\sigma_e = \sum n_i q_i \mu_i \quad (2.2.15)$$

where

- $n_i$  The number of charge carriers of type  $i$
- $q_i$  The charge of a charge carrier of type  $i$
- $\mu_i$  The mobility of type  $i$  charge carriers.

When the source in Figure 2.3 has a frequency other than zero (DC), the effective area in (2.2.14) is reduced by the skin effect. The reduced electrical penetration depth caused by the skin effect reduces the area term in (2.2.14) and thus leads to an increase in the conductor's resistivity. This shows that electrical conductivity is not a function of frequency. The effective area as seen by the charged carriers is reduced by the skin effect leading to increased conductor resistance at high frequencies.

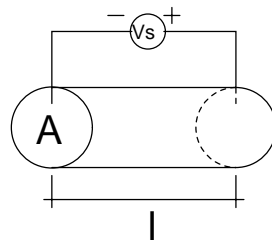


**Figure 2.3:** Conductor and parameters describing resistance.

Dielectric conductivity or dielectric damping factor is defined as[9]

$$\sigma_d = \omega \epsilon'' \quad (2.2.16)$$

It is clear that dielectric conductivity, unlike ohmic conductivity, is a function of frequency.

These two conductivity terms are combined so that the total effective conductivity is then given by 2.2.17. It is not possible to distinguish between electric and dielectric conductivity loss when the loss of a material is measured.

$$\sigma = \omega\epsilon'' + \sigma_e \quad (2.2.17)$$

At high frequencies it is easier to assume  $\sigma_e = 0$  and define conductivity as a total conductivity. The dielectric loss factor is then due to ohmic and dielectric loss[10]. Von Hippel completely ignores ohmic conductivity and defines

$$\sigma = \omega\epsilon'' \quad (2.2.18)$$

as the total conductivity. This notation works well when it is not necessary to know the origin of the loss and the frequency of excitation is much higher than zero (DC). In this thesis, measurements are made at frequencies far above 1MHz and the loss at these frequencies, as well as the dielectric constant, needs to be determined. The notation in (2.2.18) is more suited for this situation, since measurements at DC are not going to be performed and the total loss of the material is of importance.

## 2.3 Dielectric Modelling

The source of dielectric effects have been discussed and it was shown that dispersion is an analytical necessity for causality. In this section some suggested methods to describe dielectrics over a substantial frequency range is discussed. These models allow a material to be described by only a few parameters. It also allows for data interpolation between measurements. A suitable model is fitted through the measured data and can, in doing so reduce the effect of measurement and random errors. Unfortunately these descriptions are not suitable for all materials and usually describe only one mechanism. Thus a model suitable for the measured material has to be chosen and checked to ensure that it can describe the material over the required frequency range with adequate precision.

Some of the mechanisms described below have been derived from models of molecules and their interaction with an applied electric field, while other models are empirical and have been suggested after measurement of many different materials. Some materials have more than one mechanism influencing the permittivity over a small frequency range. This situation can be catered for by allowing the model to consist of a summation of elementary models.

### 2.3.1 Lorentz resonances

The Lorentz model for polarization is similar to that of a mechanical spring where damping is proportional to the velocity of oscillation[7]. An applied electric field causes a displacement of charge. The restoring force together with inertia causes a resonance. A generalised expression for  $j$  resonances at  $\omega_j$  is given by 2.3.1.  $F_j$  is a measure of the strength of the  $j$ th resonance. The summation of all resonances form the total polarisation density.

$$\alpha_j = \frac{F_j}{(\omega_j^2 - \omega^2) + j\omega\Gamma_j} \quad (2.3.1)$$

The Lorentz model is more suited to ionic and electronic polarization at high frequencies than with relaxation of dipoles and multi-poles at microwave frequencies. This is illustrated in Figure 2.2.

### 2.3.2 Debye relaxation

The relaxation characteristics of gasses and fluids at microwave frequencies are described by the Debye model. The Debye model has been derived for freely rotating spherical polar molecules in a predominantly non-polar background. Debye used *Mosotti's* hypothesis of a conductive sphere, to simplify the problem. Mosotti postulated that the additional individual field effects of the surrounding molecules will mutually cancel[10] and can be assumed to be zero. The Debye model is given by (2.3.2)[5], where  $f_r$  is the relaxation frequency.

$$\epsilon^* = \epsilon_\infty + \frac{\epsilon_s - \epsilon_\infty}{1 + j\frac{f}{f_r}} \quad (2.3.2)$$

A useful graphical representation of permittivity is the Argand diagram, where the real and imaginary part of  $\epsilon_r^*$  is plotted against each other by eliminating the frequency variable. An Argand diagram of the Debye relation is shown in Figure 2.4(a). It is clear that the Debye model forms a semi circle with the origin on the real axis.

This model also assumes that the material conductivity is negligible. In most cases the material has a low electrical conductivity, but the effect on conductivity can be seen on an Argand diagram shown in Fig 2.4(b). As would be expected, the electrical conductivity affects the loss term at lower frequencies.

The Debye model also assumes that only one relaxation time exists, which will be the case of a homogeneous material consisting of spherical molecules. If the molecules are

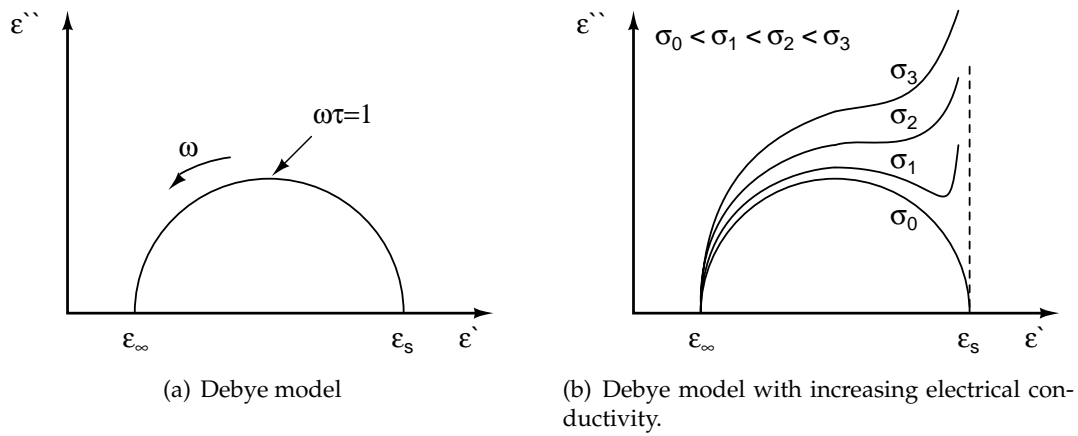


Figure 2.4: Argand diagram of Debye model with and without electrical conductivity.

not spherical, multiple relaxation times can exist. This can be modelled by the superposition of two or three Debye models with differing relaxation times.

### 2.3.3 Cole-Cole

The Cole-Cole model is similar to the Debye model, but uses one more parameter to describe the material. The examination of many dielectrics which are not in good agreement with the Debye model lead to the empirical modification of the Debye model to describe measured dielectric data[13]. This empirical formulation is given by (2.3.3).

$$\epsilon^* = \epsilon_\infty + \frac{\epsilon_s - \epsilon_\infty}{1 + (j\omega\tau_0)^{1-\alpha}} \tag{2.3.3}$$

The Cole-Cole model is a circular arc with its origin below the real axis as shown in Figure 2.5. This model reduces to the Debye model when  $\alpha = 0$ . The Cole-Cole model has been used to successfully model amorphous solids and many liquids[14] as well as water saturated rocks[15].

### 2.3.4 Cole-Davidson

Other modifications to the Debye model have also been suggested. One of these modifications is the Cole-Davidson model[5] given by Equation (2.3.4). The Cole-Davidson model has been used when the Argand diagram represents a skewed arc as illustrated in Figure 2.6. The Cole-Davidson model has been noted to work well with liquids and solid

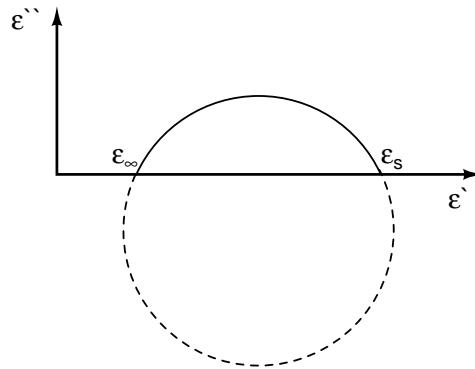


Figure 2.5: Argand diagram illustrating the character of Cole-Cole model

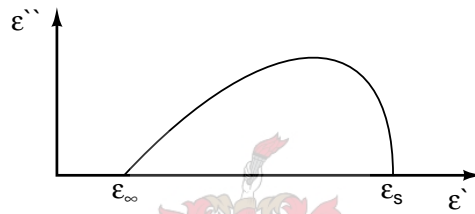


Figure 2.6: Argand diagram illustrating the character of Cole-Davidson model.

polymers[14]. The Cole-Davidson model reduces to the Debye model when  $\alpha = 1$ .

$$\epsilon^* = \epsilon_\infty + \frac{\epsilon_s - \epsilon_\infty}{(1 + i\omega\tau_0)^\alpha} \quad (2.3.4)$$

### 2.3.5 Havriliak-Negami

A more general model which has been used is a combination of the Cole-Cole and Cole-Davidson model. This model is the Havriliak-Negami model and is given by (2.3.5)[14]. This model reduces to the Cole-Cole model when  $\beta = 1$  and the Cole-Davidson model when  $\alpha = 0$ . With both  $\alpha = 0$  and  $\beta = 1$  the model reduces to the Debye model. The Havriliak-Negami model should be able to model many materials since it is a combination of two models that have been successfully used to model liquids, solids and semi-solids. The model complexity is increased compared to the Cole-Cole and Cole-Davidson models by requiring one more parameter that needs to be determined.

$$\epsilon^* = \epsilon_\infty + \frac{\epsilon_s - \epsilon_\infty}{(1 + (j\omega\tau_0)^{1-\alpha})^\beta} \quad (2.3.5)$$

### 2.3.6 Power series

A model used to describe materials does not have to be derived from the mechanism the model describes. Often a constant or a straight line is a good approximation for the permittivity of the material in the frequency range of interest. A more general description than a constant is a power series[14]. The number of terms in the power series can be varied until adequate agreement between the measurement and the model is achieved.

$$\epsilon^* = A_1 + \frac{A_2}{(1 + j\omega\tau_2)} + \frac{A_3}{(1 + j\omega\tau_2)^2} \quad (2.3.6)$$

## 2.4 Conclusion

It was shown that an increased permittivity shortens the wavelength in a dielectric and slows down the propagating electromagnetic wave. The greatest effect on the wavelength and velocity is due to the real part of the permittivity, but the loss factor also has a small influence on these parameters. The attenuation of the wave is governed by the imaginary part of the complex permittivity.

The confusion about electrical conductivity and the inclusion or exclusion of this parameter in complex permittivity has been discussed. When the DC conductivity is not of importance it is more convenient to include losses due to electrical conductivity with the dielectric conductivity. The imaginary term of the complex permittivity then represents all losses due to any energy consuming process.

A variety of models to describe the electrical properties of materials have been presented. These can be used to describe the materials over an appreciable frequency range. Most of the models describe a resonance, relaxation or a combination of mechanisms. These models can only be used effectively when the resonance or relaxation is within the measured frequency range. Often the best description for the permittivity of a material is a constant or a straight line. None of these models should be forced to fit the measurements, but a compact description is possible when they are in good agreement.

## Chapter 3

# Permittivity measurement systems

A permittivity measurement system can be divided into two main groups, namely measurement and extraction. Measurement has to do with the hardware which is used to do the physical measurement, while extraction refers to the methods used to determine the permittivity from the measurements. A diagram representing the components of a permittivity measurement system is illustrated in Figure 3.1.

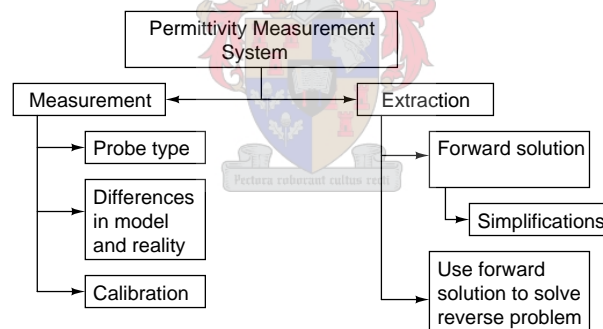


**Figure 3.1:** Diagram of components in a permittivity measurement system.

First a suitable measurement technique has to be chosen that can perform measurements in accordance with the application requirements. Once the measurement technique is known, the various methods that can be used to extract the permittivity from the measurements have to be explored.

Section 3.1 starts with a summary of important factors to consider when sifting for a measurement technique. Some general permittivity measurement methods are discussed and the best suited method for a high frequency laboratory is chosen. The problem of finding the permittivity for a given reflection coefficient is discussed in section 3.2. The

best method depends on available solutions to the forward problem, namely finding the reflection coefficient when the sample permittivity is known. Numerous formulations to the forward problem for a flat flanged coaxial probe are presented in section 3.3. This section also investigates possible simplified models that could lead to faster permittivity extraction. In section 3.4 the reflection from a coaxial probe with an extended centre pin is examined and a circuit model for this probe derived.

### 3.1 Permittivity measurement techniques

Many methods have been employed to determine the electrical properties of materials. These methods include transmission-line techniques, coaxial apertures, surface-waves, dielectric resonators, open resonators, parallel plates and others[16][17]. Good reviews of some of these methods along with advantages and disadvantages are given in [18, chap. 5], [19] and [20]. A few of the significant factors to consider when choosing a measurement technique are:

- Frequency range: Measurement techniques are generally divided into broadband and narrowband measurements. The narrowband techniques are in general more accurate, but only allow measurements at a single or a few frequencies. The measurement techniques are also limited in frequency due to limited sample size.
- Measurement of permittivity, permeability or both: Although only material permittivity has to be measured for this thesis, a technique that can measure both would be advantageous.
- Material properties: Some measurement techniques can measure inhomogeneous and anisotropic materials, where other methods assume that the material is homogeneous, isotropic or both.
- Destructive or non-destructive: Sample preparation may require that the sample be machined to fit the measurement probe. This effectively destroys the sample for further use.
- Accuracy: Accuracy is an important factor for any measurement system. Inaccurate results have limited use.
- Material form or shape: Some techniques are more suited for solids, while others require the material to be a liquid or a semi-solid (powder). A measurement technique may be more suitable for some shapes than others.



- Material preparation: Sample preparation often takes longer than the measurement and data extraction combined. This makes a measurement which requires little sample preparation ideal.
- Measurement ease: Difficult or time consuming measurements increase the chances of error. If measurements have to be performed often, it is definitely advantageous to have a fast and easy measurement system.

The factors mentioned have to be considered in the light of the intended application. To illustrate this, an example is useful. A capacitive plate measurement requires a large, flat, smooth sheet of sample material. This may be a tall order in most applications, but is perfect for measuring printed circuit boards and other dielectric sheets.

Some of the most widely used techniques[17][16] are briefly discussed in the sections that follow with specific reference to the factors mentioned. The factors which are considered most important to a high frequency laboratory is undoubtedly measurement ease, material preparation, accuracy and a broad frequency range.

### 3.1.1 Transmission lines

Transmission line techniques include all techniques where the sample material forms part of a transmission line. Transmission line techniques take advantage of the fact that propagation in a transmission line in the presence of discontinuities is well understood and readily calculated. The sample material is machined to fit tightly in the transmission line. It is important that the air gaps between the sample and transmission line walls are reduced as far as possible. The reflected and transmitted signals are measured with a vector network analyser (VNA). The impedance and loss of the transmission line are then related back to the sample permittivity. Broadband measurements can be made that depend on the transmission line used and the sample length. Coaxial lines allow measurement at lower frequencies, since the two conductors allow a TEM propagation mode to exist. The requirement for an annulus shaped material for coaxial line measurements increases the required sample preparation. Less sample preparation is required for rectangular waveguides and can be used into the millimetre frequency range. The low frequency limit of single conductor waveguides is frequency cut-off of the non-TEM modes. Practical sample sizes also limit low frequency measurements, since the waveguides and samples increase as the required frequency decreases. An illustration of a rectangular waveguide with a sample material that could be used for permittivity measurement is shown in Figure 3.2. Samples can be solids, liquids or semi-solids. The sample is as-

sumed to be homogeneous, but anisotropic samples can be measured by ensuring that only specific propagation modes exist.

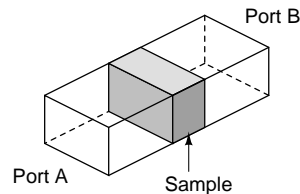


**Figure 3.2:** Illustration of a rectangular waveguide used for material characterization.

### 3.1.2 Capacitive plates

Capacitive plates are used in conjunction with impedance or LCR meters to determine the electrical properties of thin slabs at frequencies below 100 MHz. The measured capacitance and loss is used to calculate the sample permittivity since the sample thickness and plate size is known. The capacitive plates are usually large, circular and parallel so that fringing effects are minimized and small enough to be ignored. The fringing effects are also limited by using guarding to force a specified field distribution through the sample[21]. The capacitor does not have to be two parallel plates. An interesting design has been implemented by Rüttschlin[21] where cylindrical borehole samples were measured. Capacitive plates are not well suited for measurement of liquids, gels or semi-solids (powder) and the frequency range is limited to radio frequencies.

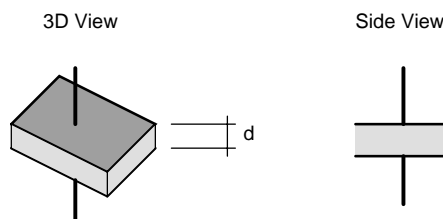


**Figure 3.3:** Illustration of a parallel plate used for material characterization.

### 3.1.3 Resonant structures

A resonant cavity is often used for material measurements and is considered to be accurate. A thin sample is placed in a resonant structure so that the fields inside are only slightly changed. This perturbation causes a slight change in resonant frequency and

quality factor that can be related to the material properties. Resonant cavities can be used to measure either sample permittivity or permeability. If the sample is placed at a magnetic field maximum, the sample permeability is measured. In the same way, permittivity measurements are performed with the material at an electric field maximum. This method is well suited for measurement of small low-loss solids. Depending on the resonant structure used, liquids and semi-solids can also be measured. Resonant methods are limited to one or a few frequency points. This makes broadband measurements time consuming. The low frequency limit for these measurements are practically sized resonant structures.

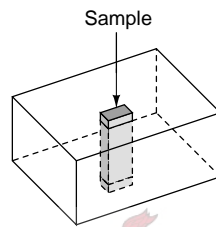


**Figure 3.4:** Illustration of a rectangular resonant cavity used for material characterization.

#### 3.1.4 Free space measurements

Free space methods are used to measure large flat slabs without contact by focusing microwave energy at the sample and measuring the reflected and transmitted signals. The fact that the measurement is non-destructive and does not require any contact with the sample allows the sample to be heated and subjected to other hostile environments. Calibration of a free space measurement set-up has been reported to be challenging[17], but a calibration routine called Gate-Reflect-Line (GRL) has been shown to perform accurate calibration and allow accurate measurements. Sample size and shape are limiting factors for free space measurements and this technique is generally used at high microwave frequencies. The sample is assumed homogeneous, but anisotropic magnetic materials can be measured. The method is obviously not well suited for the measurement of liquids and gels.

#### 3.1.5 Coaxial probes

The coaxial probe is actually a subset of the transmission line methods, but is considered separately here. There are a few possible configurations that have generally been used

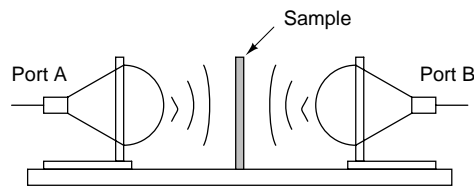


**Figure 3.5:** Illustration of a free space material measurement set-up.

for coaxial probe measurements. A comprehensive summary of coaxial probe configurations can be found in [22]. Most of these methods require extensive sample preparation to ensure that the sample fits snugly in the coaxial line. The sample is assumed homogeneous and isotropic. Some common configurations are illustrated in Figure 3.6(a)-(f). Figure 3.6(a) represents the type of transmission line measurements discussed in section 3.1.1 where both transmission and reflection measurements are performed. The other methods rely on reflection measurements only. It can thus be assumed that less accurate extraction is possible since less data is available for analysis. Especially loss parameter extractions are less accurate when transmission measurements are not performed. The methods illustrated in Figures 3.6(a)-(d) and (f) require careful sample preparation to minimise any air gaps between the sample and conductors.

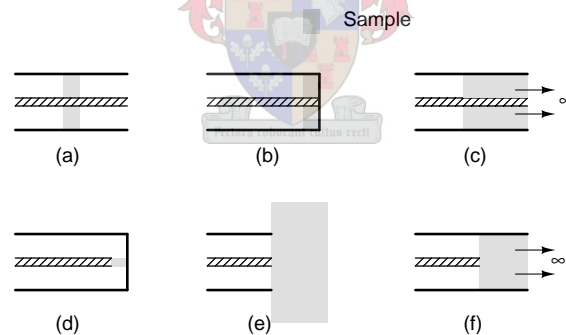


**Figure 3.6:** Configurations used for coaxial permittivity measurements.

The open-ended coaxial line, Figure 3.6(e), is an exception to this. The probe is held flush against the sample and the only requirement is that the sample is machined flat and smooth to ensure good contact with the probe face. The reflection coefficient from the coaxial line terminated in a sample material is measured and related to the sample permittivity. The method offers non-destructive, broadband permittivity measurements to be performed with reasonable measurement ease.

The open-ended coaxial line has been used with a few minor alterations, depending on the target sample. Some of these are illustrated in Figure 3.7. The unflanged probe,

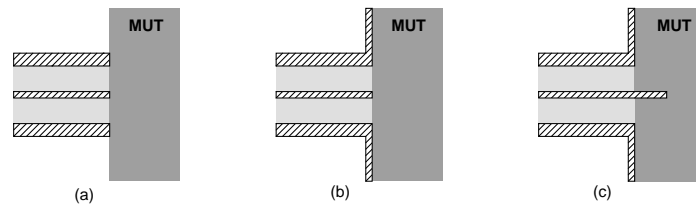


**Figure 3.7:** Three types of the open-ended coaxial probe. (a)No flange (b)Flanged (c)Extending centre pin

illustrated in Figure 3.7(a), is ideal for measurement of biological tissue since the probe can be inserted into the sample for true *in vivo* measurements. The probe has also been converted to an elliptical probe for increased sensitivity at low frequencies as well as easy insertion into gels and biological tissue. This configuration is not well suited for measurement of solids and semi-solids. Some fringing fields exist in the region around the probe which do not penetrate the sample and leads to inaccurate results. The probe also needs to be held flush against a solid and this is difficult without a supporting flange.

The flanged probe, Figure 3.7(b), is more suitable for measurement of solids, semi-solids, gels and fluids. The flange ensures that the electric fields exist only in the region in front of the probe where the sample is located. The flange supplies a good mechanical support for materials and also allows for easier calibration since it can be used to attach calibration standards to the probe face, thus allowing calibration at the measurement plane.

The centre pin of the coaxial probe, Figure 3.7(c), can also be extended into the sample material. This forces more electric field lines to pass through the sample and thus better interrogation of the material is obtained. The extruding centre pin requires more material preparation in solids, since a hole has to be drilled that fits snugly around the pin.

The fact that the open-ended coaxial probe with a flange is able to measure solids, semi-solids, gels and liquids non-destructively over a broad frequency range makes this probe ideal for general permittivity measurements in a high frequency laboratory. The measurement also requires the least amount of sample preparation of all the methods discussed. Although accuracy is lower than some of the other techniques, this may be overlooked because of all the other benefits that the coaxial probe has to offer. The best suited probe for a high frequency laboratory has been found, now the measured reflection coefficient has to be related to the sample permittivity.

## 3.2 Extracting material properties from reflection measurement

In order to extract the material permittivity from the measured reflection coefficient, the problem has to be inverted. This assumes that a solution exists to calculate the reflection coefficient for a given sample permittivity. The complexity and availability of the forward solution plays a great role when determining the best inversion method. If it is known which methods are available to invert the problem, finding a suitable solution to the forward problem is easier. The extraction methods can be divided into two main classes, namely direct and indirect inversion. They differ greatly with respect to accuracy, speed and adaptability.

- **Accuracy:** Accuracy is always important, but the accuracy of the measurement should be kept in mind. There is no sense in using an extremely accurate inversion method when the measurements can not be performed to the same accuracy level or better.
- **Speed:** Some methods are not well suited for real-time data extraction, but real-time data extraction is not always required. Extraction times of a few seconds or even minutes should be sufficient for a high frequency laboratory.
- **Adaptability:** Some methods require that large amounts of pre-processing be done. This makes small changes in probe configuration difficult to accommodate because all pre-processing has to be repeated. This is an important aspect during the design of the probe, but once the probe is completed and in use the adaptability becomes less important.

Material models can also be used to improve the data extraction when valid assumptions about the material characteristics can be made. This greatly speeds up data extraction since only a few parameters have to be determined to fully describe the appropriate model and thus less measurement points are required. To illustrate this, an example is helpful. If a liquid were to be measured and it is known that the liquid's permittivity can accurately be described by a Debye model and the measured frequency range is close to the relaxation frequency of the sample, only four parameters have to be determined. These four parameters are sufficient to describe the permittivity of the material completely over the frequency range. The measurement may consist of more than four points. This means that the system is over-determined and the parameters can be found through a least squares fit of the measurements. This approach is only useful when assumptions about the material can be made and would not be of great use to a general

high frequency laboratory where the material is completely unknown. If after measurement it is seen that the material property can be described by one of the models in section 2.3, the results can be fitted to the appropriate model. The data extraction methods discussed here are point by point data extraction methods, this means that the permittivity at each frequency point is extracted individually.

### 3.2.1 Direct inversion

Direct inversion is used when a formula can be derived for the reflection coefficient,  $\rho$ , in terms of the sample permittivity. The formula is then inverted so that the sample permittivity becomes the subject of the equation. The solution of the equation directly determines the permittivity.

$$\rho = f(\omega, \epsilon^*) \quad (3.2.1)$$

$$\epsilon^* = f^{-1}(\omega, \rho) \quad (3.2.2)$$

The greatest advantage of direct inversion is speed. It is the ideal method to use if at all possible. Unfortunately the requirement for a simple closed form solution may be a tall order. An approximation to the correct solution can also be used. The accuracy of the extracted permittivity then becomes a function of the approximation accuracy.

When the reflection coefficient can be found for the probe in air, but not in an arbitrary medium, the problem can be simplified by utilizing the Deschamps antenna modelling theorem (AMT). The AMT for non-magnetic materials can be expressed as [23]

$$\frac{Z(\omega, \epsilon^*)}{\eta} = \frac{Z(n\omega, \epsilon_0)}{\eta_0} \quad (3.2.3)$$

where

$$w = 2\pi f \quad \text{Angular frequency}$$

$$\eta = \sqrt{\mu_0/\epsilon^*} \quad \text{Complex intrinsic impedance of the dielectric medium}$$

$$\eta_0 = \sqrt{\mu_0/\epsilon_0} \quad \text{Complex intrinsic impedance of free space}$$

$$\epsilon_0 \quad \text{Permittivity of free space}$$

$$\epsilon^* = \epsilon' - j\epsilon'' \quad \text{Complex permittivity of dielectric medium}$$

$$n = \sqrt{\epsilon^*/\epsilon_0} \quad \text{Complex index of refraction}$$

Equation (3.2.3) states that the terminal impedance of an antenna in a dielectric medium,  $Z(\omega, \epsilon^*)$ , at radial frequency  $\omega$ , normalized to the intrinsic impedance of the dielectric

medium is equal to the terminal impedance of an antenna in free space,  $Z(n\omega, \epsilon_0)$ , at radial frequency  $n\omega$ , normalized to the intrinsic impedance of free space. The equation can be simplified and written in terms of terminal admittances,

$$Y(\omega, \epsilon^*) = nY(n\omega, \epsilon_0). \quad (3.2.4)$$

Equation (3.2.3) enables us to extract the material properties of a sample material, if an accurate analytical solution can be found for the terminal impedance of the antenna (probe) in free space. This method differs from the previous method in that only the free space case needs to be considered. Solutions for the impedance of antennas in free space are usually much less complicated than solutions for antennas in an arbitrary medium. The AMT has a few restrictions that could render it useless in some circumstances. The theorem is only valid when the material surrounding the probe is infinite in extent, the probe is made from perfectly conducting material and is fed from a region that is small in terms of the operating frequency[24]. The restriction that the sample has to be infinite in size can be approximated if the field is mostly contained inside the sample. The required sample size needed to approximate an infinite material is discussed in section 4.2.3. The probe has to be made from a perfect conducting material to ensure that the boundary conditions do not change due to a change in permittivity. Deschamps also notes that the theorem is strictly not valid for aperture antennas because one can not find integration paths in the medium such that the integral of electric- and magnetic fields represent, respectively, voltage and current. The proof can be extended to an antenna fed by means of a two-conductor waveguide, a coaxial line for instance, supporting a TEM wave provided that the change of medium is carried out inside the waveguide. Figure 3.8(a) and (b) show diagrams of coaxial probes where the change in medium takes place inside the waveguide. This would require the material under test to fill some part of the waveguide, making measurement of solids difficult. If the change in medium does not take place inside the waveguide, higher order modes are generated which are not accommodated by the AMT. This situation is illustrated in Figure 3.8(c) and (d).

Even in situations where the AMT is not used or is not strictly valid, it is an intuitive description of the impedance characteristic of an antenna or probe when the surrounding permittivity changes.

### 3.2.2 Indirect inversion

Indirect methods, as the name suggests, do not invert the problem directly. The forward solution is used to find the correct permittivity. Indirect inversion is useful when the for-



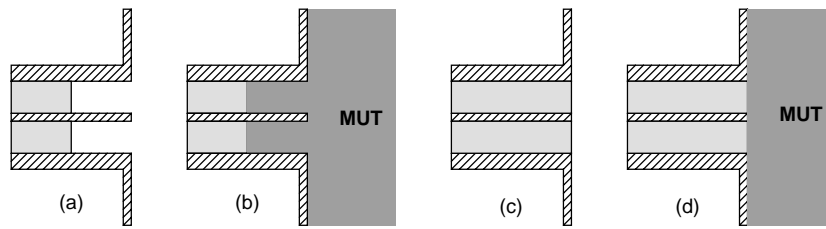


Figure 3.8: Waveguide and aperture feed of a coaxial probe

ward problem can not be simplified so that it can be inverted. The forward solution could be a simulation or a complicated full wave calculation that incorporates more than one propagation mode. Results derived using indirect methods are also more stable when the reverse solution is ill-natured. This is the case when large changes in permittivity cause only small changes in the reflection coefficient.

### Iterative calculation

Fast computers and decreasing simulation and calculation times allow a permittivity to be "guessed" and then compared to measurements until a satisfactory level of agreement is achieved. Solving the forward problem can be time consuming. Iterative calculation then leads to extremely long extraction times. This method would probably not be used for real-time applications because of the unpredictable delay between measurements and results. An effective way to "guess" the permittivity can greatly reduce extraction times. Permittivity does not change instantaneously. This means that the permittivity calculated for the previous frequency point is a good initial "guess" for the current frequency point.

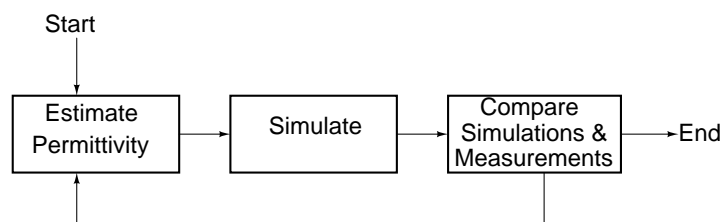


Figure 3.9: Illustration of iterative computer simulation

### Lookup table

The speed of data extraction can be greatly improved by pre-calculating many permittivity and frequency combinations. The results are saved to file and during measurements the permittivity can be found by interpolating the values calculated off-line. This method reduces the time to extract the permittivity drastically, since time consuming calculations only need to be performed once for each probe and are performed beforehand. This is an effective solution when accurate, high speed results are required for a probe configuration that does not often change. A change in the probe configuration would require that a new lookup table be calculated.

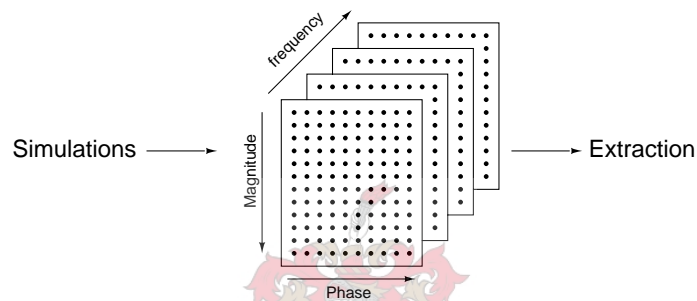


Figure 3.10: Illustration of a lookup table

### Artificial neural networks

The use of artificial neural networks (ANNs) have also been proposed[25] as an inversion approach. The speed of the neural network is used in real-time calculations while the accuracy of full-wave analytical solutions or simulations is taken advantage of during the off-line training phase. This does not lead to any understanding of the probe and there is no way to be sure that the results are correct. It shifts the problem from finding an analytical solution to adequate training of an ANN. This method does not lend itself to easy adjustment when the probe geometry changes since all the training has to be repeated. This approach is similar to the lookup table, although ANNs usually require less calculation during training than a lookup table requires for effective interpolation.

## 3.3 Flat flanged coaxial probes

A diagram of the open-ended coaxial line with associated dimensions is illustrated in Figure 3.11. The coaxial line has an inner and outer radius  $a$  and  $b$  respectively and is

filled with a dielectric with permittivity  $\epsilon_c$ . The material over the aperture is assumed to be linear, isotropic, homogeneous, non-magnetic and has a relative complex permittivity  $\epsilon_m$ . The flange is circular with radius  $g$ .

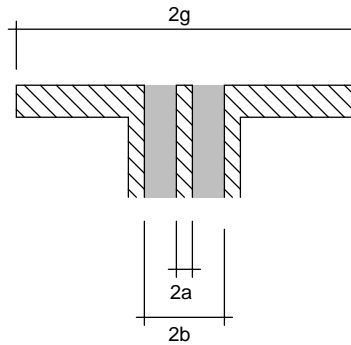


**Figure 3.11:** Diagram of an open-ended coaxial line showing the probe dimensions.

### 3.3.1 Calculating the reflection coefficient

The calculation of input impedance of a coaxial line open to a semi-infinite space has been addressed by many authors. They range from static solutions to quasi-static solutions[26][27], full wave solutions[28] and even a full wave solution that accommodates layered media[29]. Each of these calculation methods have been examined in this thesis and compared in terms of speed and accuracy.

All calculations have been performed on a AMD Athlon XP 2400(2GHz) with 1 GB RAM running Windows XP. The codes have been written in Matlab except the full wave solution from NIST which is a compiled executable.

#### Full wave solution with lift-off (NIST)

A full-wave solution has been derived by Baker-Jarvis *et al.*[29] at the National Institute for Standards and Technology (NIST) that accommodates layered media as illustrated in Figure 3.12. This solution has been used to investigate the error caused by imperfect contact of samples with the probe, known as lift-off. This is done by allowing region (2) in Figure 3.12 to represent the air between the sample in region (3) and the probe.

The solution is based on Hankel transforms in order to match the fields at the material interfaces. Only the TEM mode is assumed to propagate in the coaxial line, while higher order  $TM_{0n}$  modes exist at the interface of the coaxial probe and in the materials outside the coaxial line. Numerical calculation limits the amount of higher order modes that

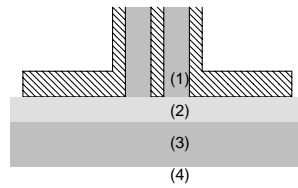


Figure 3.12: Coaxial probe terminated with layered media.

can be used in the solution, but only a few (less than 10) higher order modes need to be considered for the solution to converge.

This formulation is considered to be the most accurate and other calculations and simulations in this thesis are compared to it to determine their accuracy.

The calculation has not been implemented as part of this thesis, since it has already been implemented by NIST. They have supplied us with the compiled code for educational purposes. Calculations have been performed at ten frequencies. The average time in seconds for each frequency point is listed in Table 3.1 next to the number of  $TM_{0n}$  modes used in the calculation. It is seen that calculation time increases drastically when the number of modes is increased.

Table 3.1: Calculation times for NIST permittivity extraction code.

$TM_{0n}$ modes	Calculation [s/p]
5	2.0
10	6.47

### Quasi-static solution

A quasi-static analysis of an open-ended coaxial line terminated by a semi-infinite medium has been done by Misra [27] and Marcuvitz [26]. The quasi-static solution by Marcuvitz is valid only for the homogeneous problem where the permittivity of the material inside the coaxial line and the sample are the same. The analysis by Misra is based on a variational calculus to render the problem stationary. The normalized admittance of the probe at the interface is calculated without any regard for higher order modes in the coaxial line that could be generated at the interface. The solution is then further approximated by rewriting the exponential term as a power series and using only the first four terms of the power series. This is a reasonable approximation because the quasi-static solution is only expected to be valid at low frequencies. The admittance of a coaxial line

is then used to find the terminal admittance of the probe. The admittance of the probe is given by (3.3.1).

$$Y_L = j \frac{2\omega\epsilon_m}{[\ln(\frac{b}{a})]^2} \left[ I_1 - \frac{k^2 I_3}{2} \right] + \frac{k^3 \pi \omega \epsilon_m}{12} \left[ \frac{b^2 - a^2}{\ln(\frac{b}{a})} \right]^2 \quad (3.3.1)$$

$$I_1 = \int_a^b \int_a^b \int_0^\pi \frac{\cos(\phi')}{R} d\phi' d\rho' d\rho \quad (3.3.2)$$

$$I_3 = \int_a^b \int_a^b \int_0^\pi \cos(\phi') R d\phi' d\rho' d\rho \quad (3.3.3)$$

$$R = \sqrt{\rho^2 + \rho'^2 - 2\rho\rho' \cos(\phi')} \quad (3.3.4)$$

The integrals  $I_1$  and  $I_3$  need to be calculated numerically, but they only need to be calculated once for a specific probe since they are dependent only on the dimensions of the probe. A more complete explanation of the calculation as well as a method to numerically integrate  $I_1$  and  $I_3$  is presented in Appendix A.2.1.

The solution is a simple polynomial and is calculated almost instantly. The integration and calculation times are listed in Table 3.2.

**Table 3.2:** Calculation time of quasi-static solution by Misra.

Integration [m:s]	Calculation [s/p]
0:13	$< 10^{-6}$



### Full wave solution

A full wave solution of the reflection from an open-ended coaxial line has been developed by Mosig *et al.*[28]. The effect of lift-off is not considered, thus assuming a perfect contact between the sample and the probe. The solution is based on point matching theory. A number of equations are written in terms of the unknown reflections for modes at the interface between the sample and the coaxial line. These equations are then simultaneously solved for points on the aperture.

The modes that can exist in a symmetric coaxial line are the propagating TEM mode as well as non-propagating  $TM_{0n}$  modes. The solution is only valid at frequencies where the  $TM_{0n}$  modes are not propagating in the coaxial line. The radial distribution for the dominant TEM mode ( $n = 0$ ) is given by (3.3.5).  $N_0$  is the normalizing factor of the TEM

radial function.

$$f_0(\rho) = \frac{N_0}{\rho} \quad (3.3.5)$$

$$N_0 = \frac{1}{\sqrt{\ln(b/a)}} \quad (3.3.6)$$

The modal radial distributions for the higher order  $\text{TM}_{0n}$  modes ( $n \geq 1$ ) are given by (3.3.7).  $J_n(x)$  is the  $n^{\text{th}}$  order Bessel function of the first kind and  $Y_n(x)$  is the  $n^{\text{th}}$  order Bessel function of the second kind. The normalizing factors for these radial function are given by  $N_n$ . The modal radial functions form an orthonormal set.

$$f_n(\rho) = N_n [J_1(p_n\rho)Y_0(p_na) - Y_1(p_n\rho)J_0(p_na)] \quad (3.3.7)$$

$$N_n = \frac{\pi p_n}{\sqrt{2}} \left[ \frac{J_0^2(p_na)}{J_0^2(p_nb)} - 1 \right]^{-\frac{1}{2}} \quad (3.3.8)$$

The eigenvalues,  $p_n$ , are calculated from (3.3.9) to satisfy the boundary conditions inside the coaxial line.

$$Y_0(p_na)J_0(p_nb) = J_0(p_na)Y_0(p_nb) \quad (3.3.9)$$

The propagation factors,  $\gamma_n$ , are then calculated from ( $c_0$  is the velocity of light),

$$\gamma_n = \sqrt{p_n^2 - \epsilon_c(w/c_0)^2}. \quad (3.3.10)$$

Point matching is performed by ensuring continuity of the magnetic field across the boundary at the interface between the probe and the sample ( $z = 0$ ),

$$\mathbf{H}_\phi(\rho, z = 0^-) = \mathbf{H}_\phi(\rho, z = 0^+). \quad (3.3.11)$$

This leads to

$$\sum_{n=0}^{\infty} \mathbf{R}_n \mathbf{T}_n = 1 \quad (3.3.12)$$

$$\mathbf{T}_n = \frac{f_n(\rho)/\gamma_n + (\epsilon_m/\epsilon_c)\mathbf{I}_n}{f_0(\rho)/\gamma_0 - (\epsilon_m/\epsilon_c)\mathbf{I}_0} \quad (3.3.13)$$

$$\mathbf{I}_n = \frac{1}{2\pi} \int_a^b f_n(\rho') \rho' \int_0^{2\pi} \frac{e^{-j(\omega/c_0)\sqrt{\epsilon_m}R}}{R} \cos(\psi) d\psi d\rho' \quad (3.3.14)$$

$$R = \sqrt{\rho^2 + \rho'^2 - 2\rho\rho' \cos(\phi')} \quad (3.3.15)$$

The exact resolution of the problem would require continuity of the magnetic field over the entire coaxial aperture,  $a < \rho' < b$ . This would require an infinite series of  $\text{TM}_{0n}$  modes to be matched at an infinite number of points. On a computer a finite number of modes,  $N$ , is considered on  $N$  circles within the aperture. The solution is found by solving the set of linear equations in (3.3.12).

The selection of the points where matching is done plays an important role to ensure fast convergence of the reflection coefficient. Mosig found that internal and external distribution of the points lead to an upper and lower bound on the reflection coefficient. He suggested the use of an arithmetic mean of internal and external distribution. The radial positions are then given by (3.3.16),

$$\rho_r = a + \frac{b-a}{2} \left[ \frac{r-1}{N-1} + \frac{2r-1}{2N} \right], \quad (3.3.16)$$

where  $r = 1, 2, \dots, N$ .

A comparison with the full-wave solution by Baker-Jarvis *et al.*[29] indicates that better agreement is achieved by using an internal distribution as given by (3.3.17),

$$\rho_r = a + (b-a) \left[ \frac{2r-1}{2N} \right]. \quad (3.3.17)$$

This is how far Mosig developed the formulation. The problem with the solution is the numerical integration required for  $\mathbf{I}_n$  is time consuming and the calculation has to be repeated for a change in frequency or sample permittivity. A few simplifications and approximations have been made in this thesis that greatly increases calculation speed.

Integration of (3.3.14) with respect to  $\psi$  over the range  $[0, 2\pi]$  can be reduced to  $[0, \pi]$  since the function inside the integral is symmetric around  $\pi$ .

$$\mathbf{I}_n = \frac{1}{\pi} \int_a^b f_n(\rho') \rho' \int_0^\pi \frac{e^{-j(\omega/c_0)\sqrt{\epsilon_m}R}}{R} \cos(\psi) d\psi d\rho' \quad (3.3.18)$$

The singularity in (3.3.14) should also be removed to increase the speed of numerical integration. The extracted singularity can then be calculated using the elliptical function

of the first kind as in section A.2.1,

$$\begin{aligned} \mathbf{I}_n &= \frac{2}{\pi} \int_a^b f_n(\rho') \rho' \frac{K(p^2)}{\rho + \rho'} d\rho' \\ &+ \frac{1}{\pi} \int_a^b f_n(\rho') \rho' \int_0^\pi \frac{\cos(\psi) e^{-j(\omega/c_0)\sqrt{\epsilon_m}R} - 1}{R} d\psi d\rho'. \end{aligned} \quad (3.3.19)$$

The exponent under the integral in (3.3.19) can be expanded into a power series,

$$e^x = 1 + x + \frac{x^2}{2!} + \frac{x^3}{3!} + \frac{x^4}{4!} + \dots \quad (3.3.20)$$

The second term in the power series reduces to zero during integration over  $\psi$ . After the power series expansion the frequency and permittivity can be taken outside the integral.

$$\begin{aligned} \mathbf{I}_n &= \frac{2}{\pi} \int_a^b f_n(\rho') \rho' \left[ \frac{K(p^2)}{\rho + \rho'} \right] d\rho' \\ &+ \frac{1}{\pi} \int_a^b f_n(\rho') \rho' \int_0^\pi \frac{\cos(\psi) - 1}{R} d\psi d\rho' \\ &+ \frac{1}{\pi} \sum_{x=2}^{M-1} \frac{(-j(\omega/c_0)\sqrt{\epsilon_m})^x}{x!} \left[ \int_a^b f_n(\rho') \rho' \int_0^\pi R^{x-1} d\psi d\rho' \right] \end{aligned} \quad (3.3.21)$$

The numerical integration need now be performed only once for a probe, since the integrand only depends on the probe geometry and not the sample permittivity or frequency. The frequency, sample permittivity and coaxial line permittivity can easily be changed and then equation (3.3.13) solved to find the new reflection coefficient without any further numerical integration. It is necessary to use more terms for the power series than used for the quasi-static solution since the solution is valid at higher frequencies.

This method requires  $MN^2$  integrations to be performed, where  $M$  is the number of terms in the power series and  $N$  is the number of  $TM_{0N}$  modes considered. This shows the linear relationship between the number of exponent terms used and the time required for calculating the integrals. It also shows that the calculation effort increases quadratically with an increase in  $TM_{0n}$  modes.

Calculation times have been measured using an average of 100 calculation points. These times are listed in Table 3.3. It was found that 15 power series terms are sufficient to accurately approximate the exponential.

### Simulation

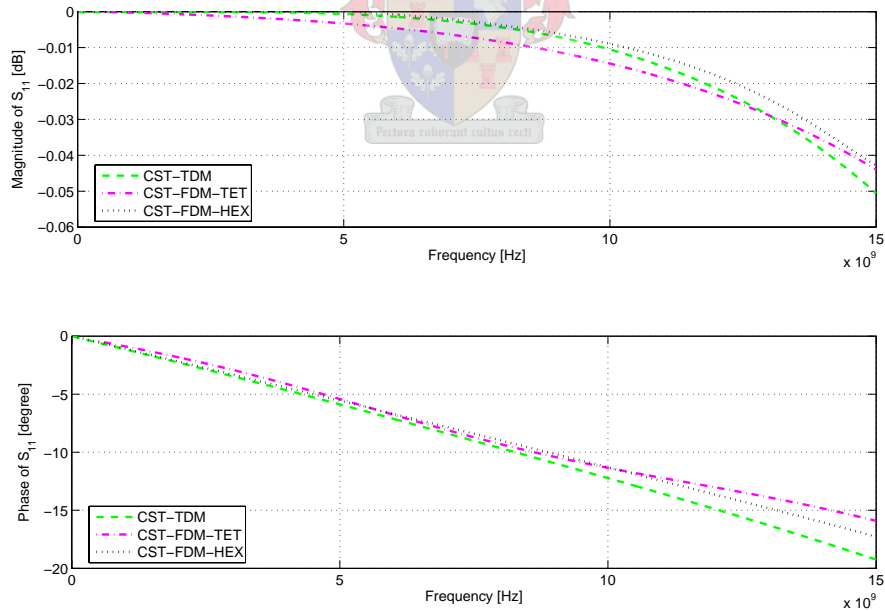
Simulations of an open-ended coaxial probe and a sample material have been performed using CST<sup>®</sup> Microwave Studio. CST<sup>®</sup> is the simulation package of choice because it



**Table 3.3:** Calculation time of full-wave solution by Mosig.

$TM_{0n}$ modes	Power series terms	Integration [m:s]	Calculation [s/p]
5	15	0:54	0.0150
10	15	6:32	0.0160

allows different types of meshing as well as having three different solvers. These solvers can then be compared to each other as an indication of accuracy and confidence of the simulations. In all simulations the results have been tested for convergence with respect to meshing and energy left in the system. Mesh refinements were done using the "expert" system suggested by CST<sup>®</sup>. Simulations have been performed using the time-domain and frequency domain solver. The eigen-mode solver was not applicable to this type of simulation since it can not be used in unbounded problems. A hexahedral mesh with the perfect boundary approximation(PBA) was used for time-domain simulations, while hexahedral and tetrahedral meshing was used for frequency-domain simulations. All simulations converged locally, but they did not converge globally to the same point. The simulation results differ by up to 15%. The simulated reflection coefficient of a SMA-sized coaxial probe in air is shown in Figure 3.13.

**Figure 3.13:** Simulations of reflection coefficient of an open-ended coaxial line into air.

Simulations have also been performed by Gajda *et al.*[30] using the Method of Moments (MOM) and Finite Element Method (FEM). The capacitance of the two methods differed by more than 5%. The FEM code differed from measurements by almost 10%, while the MOM code differed by 4% from measurements. This indicates that simulations have to be used with care and the accuracy compared to a full-wave solution.

### Comparison of calculation methods

The magnitude and phase of a SMA-sized coaxial line open to air has been calculated using all the methods and is displayed in Figure 3.14. The two full-wave solutions are in excellent agreement. The difference in reflection coefficient is less than -40dB. These are difficult to distinguish in the diagram because they are practically the same over the entire frequency range.

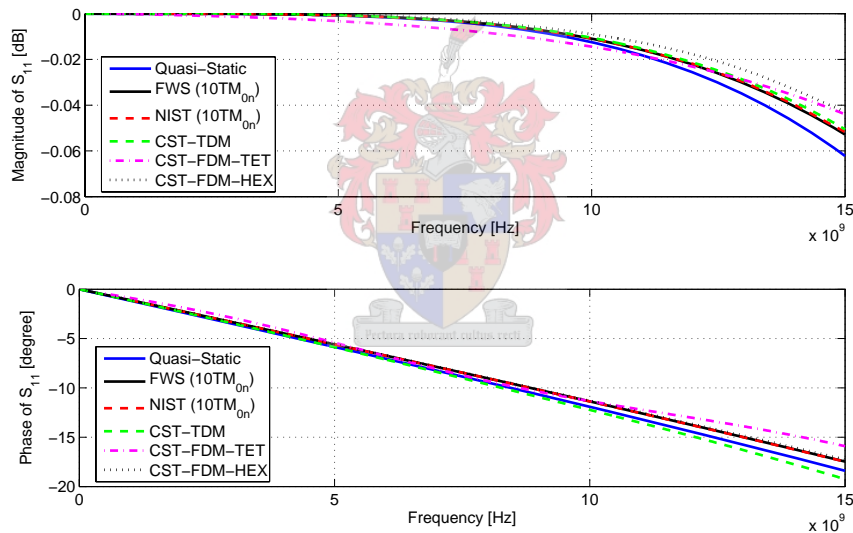


**Figure 3.14:** Simulations and calculations of the reflection coefficient of an open-ended coaxial line.

It is clear that the quasi-static solution is not in good agreement with the full-wave solutions. The quasi-static solution starts deviating from the full-wave solution at frequencies above 2 GHz. It is expected that the solution becomes less accurate with an increase in frequency and this is also seen in Figure 3.14. This shows that the higher order  $TM_{0n}$  modes, that are generated at the interface of the coaxial line, is significant even at low frequencies.

The most accurate simulation results were obtained using a frequency domain simulation with hexahedral meshing. The time domain simulation is in good agreement up to 3 GHz, but thereafter it deviates greatly.

The three calculation methods that have delivered good results are two full-wave solutions and the hexahedral frequency domain simulation. The simulation is the most time consuming, followed by the code developed at NIST. The fastest accurate calculation is the full-wave solution by Mosig with the approximations made in this thesis to reduce numerical integration time.

### 3.3.2 Simplified equivalent models

The impedance of an open-ended coaxial probe is similar to a single capacitor. This is only a first order approximation and the validity of this and other more complicated models are presented here. If a simple, yet accurate, model of the probe can be found, the Deschamps antenna modelling theorem can be used to find the sample permittivity fast. The capacitance of a probe can change as a function of frequency and sample permittivity. The capacitance over frequency of a SMA-size probe is shown in Figure 3.15. The capacitance changes by more than 5% from DC to 15 GHz. If the probe is only used over half this frequency range, the deviation reduces to 1.5%. This means that the probe can be accurately modelled as a constant capacitance at low frequencies.

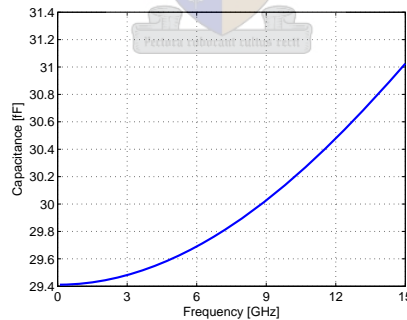


**Figure 3.15:** Capacitance of SMA size coaxial probe in air.

The capacitance also changes due to changes in sample permittivity. This capacitance can be normalized with respect to the permittivity. The normalized capacitance should remain constant unless higher order modes are generated that are not described by the simple capacitor model. Figure 3.16 shows the normalized capacitance of a SMA-size probe at 1 GHz. The single capacitor model clearly is a poor approximation for samples

with a dielectric constant of less than 20. The normalized capacitance changes by more than 14% for changes in permittivity from 1 to 80. Samples with dielectric constants above 20 can be approximated with a constant normalized capacitance without being in error by more than 1%. The nature of the fringing capacitance has also been investigated by Gajda *et al.*[30] through simulation and they came to the same conclusion.

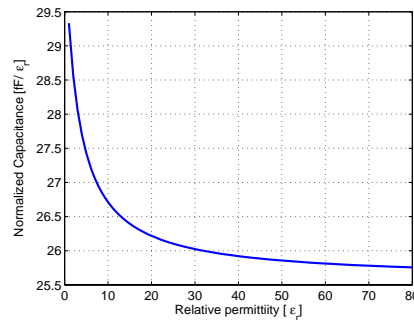


**Figure 3.16:** Normalized capacitance of SMA sized coaxial probe with different samples.

The change in normalized capacitance is due to the electric fields close to the face of the probe being distorted. Electric fields exist easier in a medium with high permittivity. This causes the electric field to be pulled closer and into the high dielectric sample. The opposite is of course true when the sample has a lower dielectric constant compared to the dielectric of the coaxial line. In this case, some of the electric field is pulled into the coaxial line. These higher order modes that are generated at the interface is one of the limiting factors that Deschamps mentions when utilizing the antenna modelling theorem. An illustration of the distorted electric field is shown in Figure 3.17.

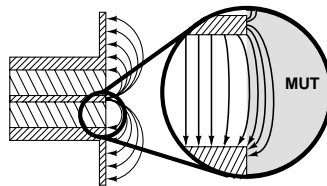


**Figure 3.17:** Diagram illustrating fringing fields of a coaxial probe.

It was seen that the input impedance of a coaxial probe can in general be represented by a lossy capacitor. The models in the sections that follow will try to incorporate the capacitance deviation due to changes in frequency and sample permittivity. The greatest deviation in capacitance has been shown to be due to fringing effects caused by different

samples placed in front of the probe. All the models, except for the rational function, assumes that the capacitance remains constant with respect to frequency. The models are thus more valid at lower frequencies or over relatively short frequency ranges.

### Constant fringing capacitance

Stuchly[31][32] included a constant capacitor to represent the extra fringing capacitance. This model is illustrated in Figure 3.18. The admittance of the probe is given by (3.3.22), where  $\epsilon_s$  is the relative permittivity of the sample.

$$Y = j\omega C_f + j\omega\epsilon_s C_0 + \omega^4 G_r \sqrt{\epsilon_s^5} \quad (3.3.22)$$

It consists of a constant fringing capacitance due to the electric fields inside the coaxial line that have been pulled out by the sample, an external lossy capacitance that is dependent on the permittivity of the sample and a radiation conductance. The radiation conductance can be ignored to further simplify the equivalent circuit, since the probe is expected to be used at frequencies where radiation is minimal.

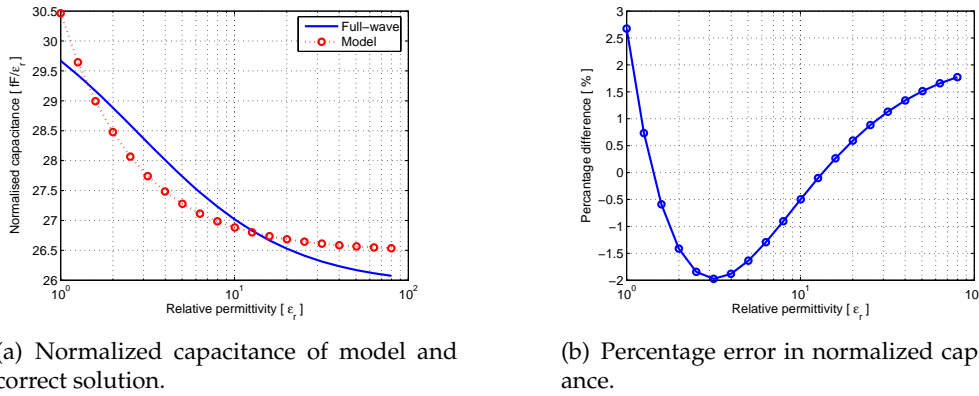
$$Y = j\omega(C_f + \epsilon_s C_0) \quad (3.3.23)$$



Figure 3.18: Model for coaxial line.

The limitation of this model is the assumption that the fringing capacitance,  $C_f$ , remains constant and is not dependent on the permittivity of the material under test. A best fit of  $Y$  in the least squares sense to the full wave solution has been performed and is plotted in Figure 3.19(a) with the correct normalized capacitance calculated with the full wave solution. The percentage error is also plotted as a function of permittivity in Figure 3.19(b). The permittivity axis is plotted on a logarithmic scale for better visualization.

It was seen that a maximum percentage error in normalized capacitance is 2.5%. This is not a big error and is a large improvement over a single capacitor model that had an error of 14%.



**Figure 3.19:** Least squares fit of model with constant fringing capacitance to full-wave solution.

#### Four capacitor model

The model suggested by Gajda[33] was expected to be more representative of the fringing capacitance of a coaxial line. This model consists of four capacitors and thus greatly increases the complexity of the equivalent circuit. The equivalent circuit is derived from analogy with a parallel-plate capacitor filled with an inhomogeneous dielectric. The equivalent circuit, neglecting fringing effects, for a configuration where the dielectric interface is tangential to the electric field, as shown in Figure 3.20(a), is two parallel capacitors. The equivalent circuit for a configuration where the dielectric interface is normal to the electric field, as shown in Figure 3.20(b), is two series capacitors. It can then be expected that for a system with normal and tangential electric fields, a combination of series and parallel capacitors can adequately represent the fringing fields. The probe with the suggested model is shown in Figure 3.20(c).

The total capacitance is then given by (3.3.24).

$$C(\epsilon_m) = \epsilon_c C_{p1} + \epsilon_m C_{p2} + \frac{\epsilon_c C_{s1} \epsilon_m C_{s2}}{\epsilon_c C_{s1} + \epsilon_m C_{s2}} \quad (3.3.24)$$

The permittivity of the coaxial line,  $\epsilon_c$ , is constant and allows (3.3.24) to be written as (3.3.25).

$$C(\epsilon_m) = C_{fp} + \epsilon_m C_0 + \frac{\epsilon_m C_{fs1}}{1 + \frac{\epsilon_m C_{fs1}}{C_{fs2}}} \quad (3.3.25)$$

The four unknowns in (3.3.25) can be found using a least squares fit of the equation to data obtained by the full-wave solution. The fitted model and the full-wave solution

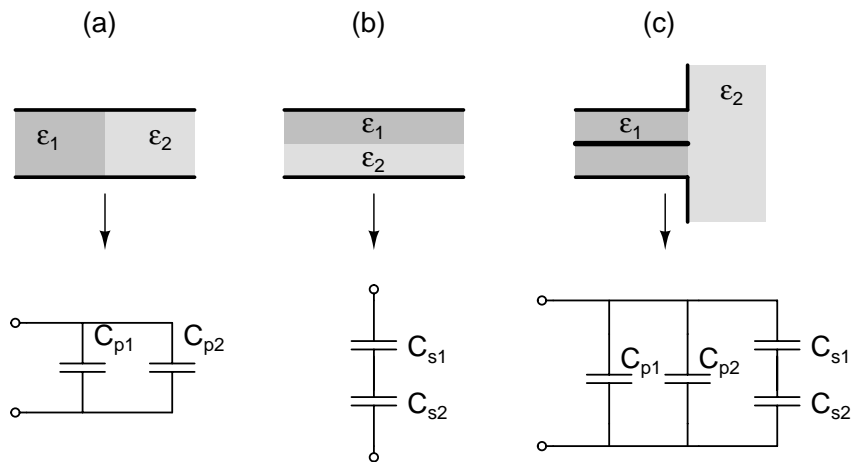
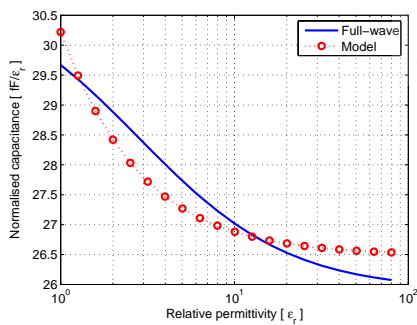
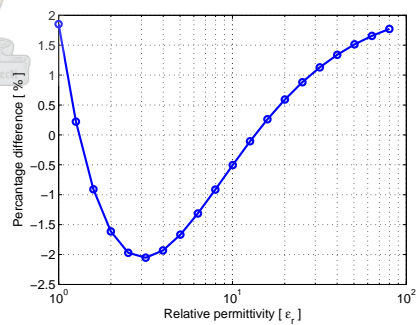


**Figure 3.20:** Equivalent circuit of capacitors for inhomogeneous dielectric and an open-ended coaxial line.

is shown in Figure 3.21(a). The percentage difference is shown in Figure 3.21(b). The maximum percentage error in normalized capacitance is 2%. It is clearly seen that this model with two more parameters is only a slight improvement over the model with a constant fringing capacitance. There is no real improvement, but the model has been greatly complicated.



(a) Normalized capacitance of model and correct solution.



(b) Percentage error in normalized capacitance.

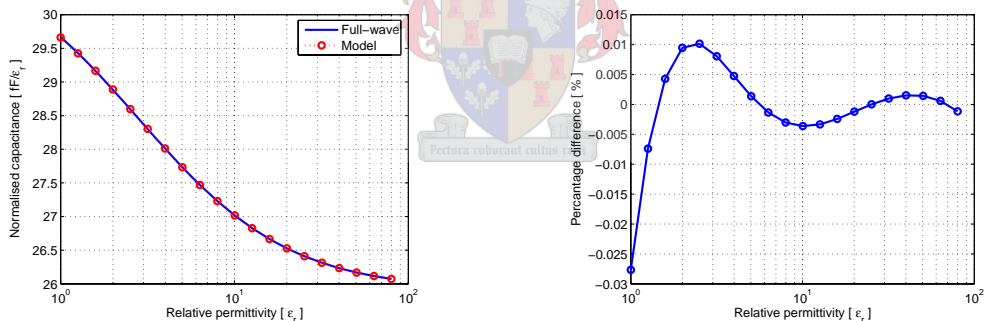
**Figure 3.21:** Least squares fit of model with series and parallel capacitors to full-wave solution.

### New function

Without looking for a circuit equivalent, other functions can be found that will better suit the shape of the normalized capacitance. A new function to describe the admittance of an open-ended coaxial line is presented in this thesis. A model that adds capacitance for low permittivity samples, but has little effect for high permittivity samples, is given by (3.3.26). This model consists of a constant capacitance term, a term proportional to the capacitance of the sample material and a third term that is inversely proportional to the sample material. The third term would increase the low frequency capacitance, but have negligible effect when samples have high permittivity.

$$C(\epsilon_m) = \epsilon_c C_f + \epsilon_m C_0 + \frac{C_2}{k + \epsilon_m} \quad (3.3.26)$$

This model has also been fitted to the full-wave solution and the results are shown in Figures 3.22(a) and 3.22(b). This model represents the capacitance from the full wave solution best and is in error by less than 0.03%. Although the complexity is increased by introducing two more parameters when compared to the constant fringing capacitance model, the accuracy also improved greatly.



(a) Normalized capacitance of model and correct solution.

(b) Percentage error in normalized capacitance.

Figure 3.22: Least squares fit of new model to full-wave solution.

### Rational function

Stuchly *et al.*[34] suggested the use of a rational function to describe the admittance of a coaxial probe. This technique has been verified by Anderson *et al.*[35] and delivered



good results. The rational function is fitted in the complex plane and includes radiation by the probe.

The rational function is given by (3.3.27). Anderson used twenty frequency points and 56 dielectric constants in the range  $1 \leq \epsilon_m \leq 80$  for the Levenberg-Marquardt fitting algorithm. An acceptable fit was obtained for  $N = M = 4$  and  $P = Q = 8$ .

$$Y(s, \epsilon_m) \approx \frac{\sum_{n=1}^N \sum_{p=1}^P \alpha_{np} (\zeta^p s^n)}{1 + \sum_{m=1}^M \sum_{q=0}^Q \beta_{mq} (\zeta^q s^m)} \quad (3.3.27)$$

$$\zeta(s) = \sqrt{\epsilon_m(s)} \quad (3.3.28)$$

Although this method has shown good results, the method of fitting data to a 32 term over 36 term rational function is questionable. This method is the most complicated with 68 unknowns that have to be determined. This model differs from the other models because the function is fitted at different frequencies and sample permittivity values. All the effects by higher order modes that are generated are included in this model, assuming a reasonable fit can be obtained.

### 3.3.3 Extracting permittivity

The method of finding the inverse solution for the different methods and models is discussed in terms of computation time, ease of use and accuracy. Not all the methods have been used to find the inverse solutions. The quasi-static approximation and the rational function is not considered, because the other methods are more accurate and more robust.

The code developed at NIST is complex because it can accommodate layered media and finite height samples. This also makes it slower. The calculation times are listed in Table 3.4. The times listed in Table 3.1 were for calculating the reflection when the sample permittivity is known. Table 3.4 list the time required to calculate the sample permittivity for a given reflection coefficient. These times depend greatly on the initial guess of the permittivity and are only an indication of expected calculation times.

**Table 3.4:** Calculation times for NIST permittivity extraction code.

TM <sub>0n</sub> modes	Extraction [s/p]
5	11.6
10	39.7

The full wave point-matching solution with the extra approximations made in this thesis is fast enough to use a zero finding algorithm to find the permittivity. The secant method[36] has been used to find the zero of (3.3.29), where  $\Gamma_c$  is the calculated reflection coefficient and  $\Gamma_m$  is the measured reflection coefficient.

$$f(\epsilon^*) = \Gamma_c - \Gamma_m \quad (3.3.29)$$

The secant method starts with two initial guesses of the permittivity close to that of air. All subsequent initial guesses for the permittivity is chosen as the extracted permittivity of the previous point. This is a good initial guess because material properties do not change drastically with frequency and are continuous functions at microwave frequencies.

The calculation times for the full wave solution are listed in Table 3.5. Two times are listed, the first is the pre-calculation required to do numerical integration and the second is the actual time (in seconds) per frequency point required to determine the permittivity. The speed improvement for 10  $TM_{0n}$  modes is more than 500 times faster when it is compared to the NIST code. The extraction time for 101 frequency points is about seven seconds, which is definitely fast enough for high frequency laboratory measurements.

**Table 3.5:** Calculation times for full wave secant permittivity extraction.

$TM_{0n}$ modes	Power series terms	Integration [m:s]	Extraction [s/p]
5	15	0:54	0.0307
10	15	6:32	0.0675

### 3.4 Probe with extruding centre pin

Another variant of the coaxial probe that is worth investigating is similar to the flat flanged probe, but with the centre conductor extended beyond the measurement plane. The construction of the probe is illustrated in Figure 3.23.

The extended centre pin requires increased sample preparation when compared to the flat flanged probe, although this is not a problem with liquid and gel measurements. This is an invasive measurement since the centre conductor extends into the sample. This invasive nature can ensure better contact between the sample and the probe and thus a better material interrogation. As in the case of the flat flanged probe, the sample material is assumed linear, homogeneous, isotropic and non-magnetic.

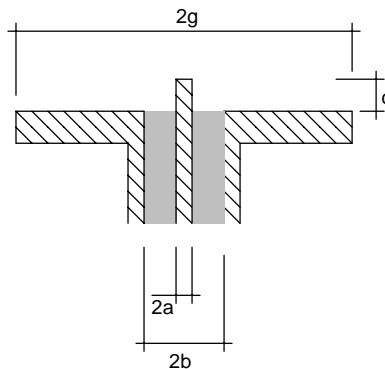


Figure 3.23: Illustration of coaxial probe with extended centre pin showing all dimensions.

### 3.4.1 Calculating the reflection coefficient

Burdette[23] suggested that the input impedance of a coaxial probe given by Tai[37, chap. 3] be used. Tai gives a simple equation for the impedance of a short monopole and then simplifies this further for a short monopole. The equation is only valid for thin antennas, where the wire length to radius ratio is large. The simplified equation is given by (3.4.1) ( $l$  is the length of the monopole,  $a$  is the wire radius and  $k = 2\pi/\lambda$ ). For the pin radius to length to be considered large, the length should be at least five times the diameter. The pin should be as short as possible to allow easy sample preparation and keep the pin far from resonance so that sample size does not become a limiting factor. Larger pins would also require a larger ground plane for the equations to be valid. Simulations have been performed with a reasonable length pin for a 7/16-size probe. The simulations were not in good agreement with Equation (3.4.1).

$$(Z_i)_{short} = 20(kl)^2 - j\frac{120}{kl} \left( \log \left( \frac{2l}{a} \right) - 1 \right) \quad (3.4.1)$$

No other analytical solutions could be found and simulations were used to determine the reflection from the probe. In order to gain confidence in the simulated results, two different solvers and two different meshes have been used and compared. The solvers are the time and frequency domain solvers in CST<sup>®</sup>. Tetrahedral and hexahedral meshing was used for the frequency domain, while the tetrahedral meshing with PBA was used for the time domain solver. All simulations were tested for local convergence and the results are summarized in Figures 3.24(a) and 3.24(b). The difference in capacitance is less than 3.7% and the difference between the time domain solver and tetrahedral frequency domain solver is about 2%. The simulations can now be used and the results assumed accurate. The time domain solver is the fastest and has been used for all further

simulations of the coaxial probe with an extended centre pin.

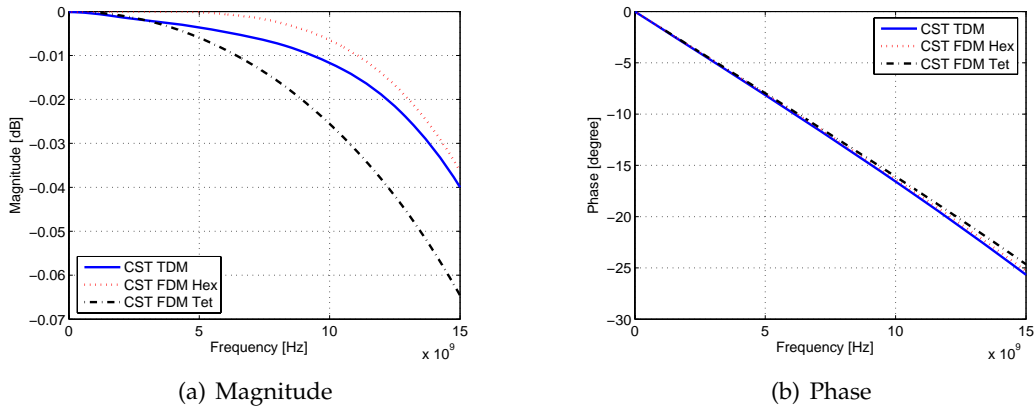


**Figure 3.24:** Simulated reflection of a 7/16-sized coaxial line with 10 mm extended centre pin using different solvers and meshing in CST.

### 3.4.2 Equivalent circuit model

An equivalent circuit can be derived from the physical topology of the probe. The centre pin would add inductance, while the electric fields from the pin to the ground add capacitance. This leads to the ladder circuit shown in Figure 3.25(a). This circuit can be approximated by 3.25(b). Radiation losses are ignored because the probe is used at low frequencies where the radiation is negligible. The fringing fields inside the coaxial line close to the interface are distorted, but the capacitance caused by the fringing fields outside the probe should be much greater. In this case  $C_f$  can be ignored, since its effect on the total capacitance is small. The admittance of the probe in air is then given by (3.4.2).

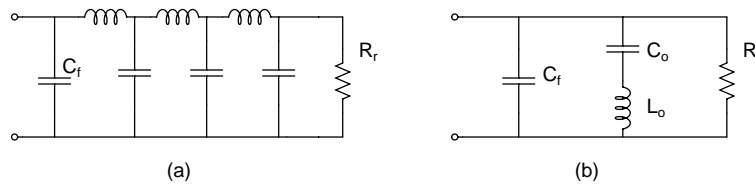


**Figure 3.25:** Equivalent circuit using Inductor and Capacitor of an extended pin coaxial probe.

$$Y(\omega) = \frac{j\omega C_0}{1 - \omega^2 L_0 C_0} \tag{3.4.2}$$

Using the antenna modelling theorem, the probe admittance in a sample material with permittivity  $\epsilon_m$  is given by (3.4.3).

$$Y(\omega, \epsilon_m^*) = \frac{j\epsilon_m^* \omega C_0}{1 - \omega^2 L_0 C_0 \epsilon_m^*} \quad (3.4.3)$$

The values of  $C_0$  and  $L_0$  can be determined by fitting (3.4.2) to the simulated admittance for the probe in a vacuum. Better results were obtained by determining the values for  $C_0$  and  $L_0$  from a higher permittivity sample. The capacitance of the probe is small and by simulating a higher capacitance allows for a better fit. The capacitance of the probe has been fitted and the results are shown in Figure 3.26(a) and 3.26(b). The maximum percentage difference between the model and the simulated data is less than 0.25%. This shows that the suggested equivalent circuit is a reasonable model.

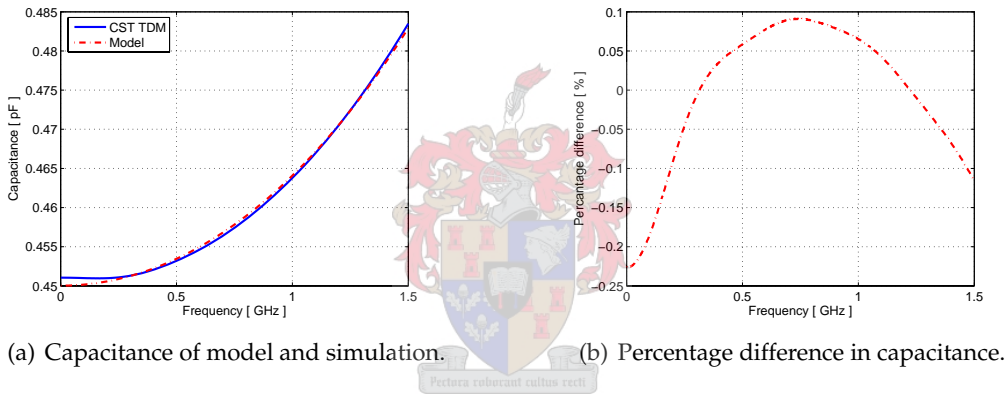


Figure 3.26: Least squares fit of model to the time domain simulated data from CST.

### 3.4.3 Extracting permittivity

The simple equivalent circuit for this probe allows that the antenna modelling theorem be used to find the material permittivity. If  $Y_m$  is the measured admittance, (3.4.4) is the sample permittivity.

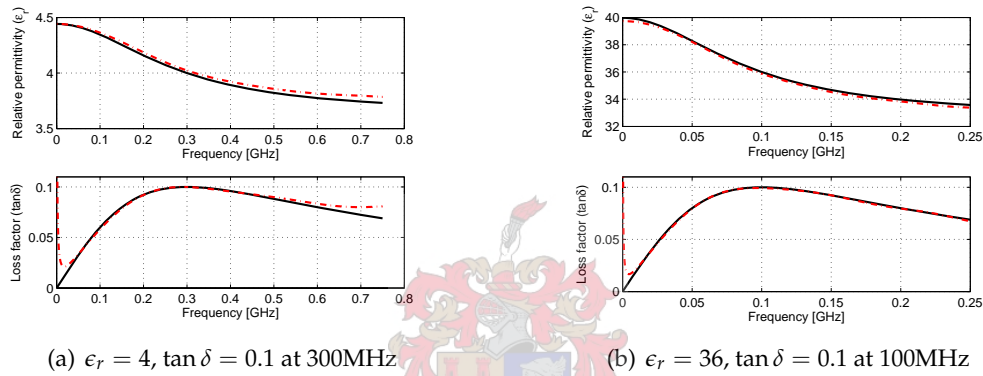
$$\epsilon_m^* = \frac{Y_m}{j\omega C_0 + Y_m \omega^2 L_0 C_0} \quad (3.4.4)$$

The values for  $L_0$  and  $C_0$  are listed in Table 3.6. Simulations have been performed on materials with well spaced dielectric constants of four and thirty six respectively. The materials have a Debye distribution and a  $\tan \delta = 0.1$  at 300MHz and 100MHz respectively.

**Table 3.6:** Element values for equivalent circuit model of pin extended probe.

$C_0$ [pF]	$L_0$ [nH]	$C_f$ [pF]	$R_r$ [ $\Omega$ ]
0.44663	1.6337	0	$\infty$

Equation (3.4.4) and the values in Table 3.6 are used to calculate the permittivity from the simulated reflections. The results are shown in Figures 3.27(a) and 3.27(b). Excellent agreement can be seen between the simulated permittivity and the extracted permittivity. Slight deviations appear at high frequencies where the radiation term increases, but the effect is small.

(a)  $\epsilon_r = 4$ ,  $\tan \delta = 0.1$  at 300MHz(b)  $\epsilon_r = 36$ ,  $\tan \delta = 0.1$  at 100MHz**Figure 3.27:** Exact(solid) and extracted(dashed) real permittivity and loss factor.

### 3.5 Conclusion

The chapter was introduced with a graphical representation of a permittivity measurement system followed by a discussion of the important factors to be considered when sifting for a general permittivity measurement system. The open-ended coaxial probe was selected as the best candidate, because it allows measurement of solids, liquids and semi-solids over a wide frequency range and permittivity range. The probe requires minimum sample preparation since the only requirement is that the sample surface be flat and smooth to ensure good contact with the probe face.

Calculation of both the forward and reverse problem has been investigated and a fast, accurate method for permittivity extraction was developed. Extraction times of less than 10 seconds for 100 frequency points is achieved on an average personal computer. These times are more than adequate for a HF laboratory.

Simplified equivalent models for extremely fast permittivity extraction over short frequency ranges have been analysed in terms of accuracy and complexity. A new model has been proposed that fits the normalised capacitance of materials with dielectric constant ranging from 1 to 80 well. This model can be used when extremely fast permittivity is required over a relatively narrow frequency range.

The coaxial probe with an extended centre pin was also investigated and an equivalent circuit model has been derived. This equivalent circuit allows the Deschamps antenna modelling theorem to be utilised to extract the sample permittivity. The permittivity extraction was tested with simulated reflections and the extracted permittivity is in good agreement with the expected permittivity.



# Chapter 4

## Design

The full wave solution developed in the previous chapter can now be used to investigate the properties of the coaxial probe. This allows intelligent design and usage choices to be made for optimum performance. It also allows an estimate of the accuracy of the measurements that can be achieved with the open-ended coaxial probe.

Section 4.1 presents the concept of sensitivity. The probe sensitivity with respect to dielectric constant and loss factor is determined. The usable frequency range of the open-ended coaxial probe is discussed in section 4.2. This section also investigates the effect of finite sized samples and limited ground planes. The influence of air between the sample and the probe is presented in section 4.2.4. The dimensions of the four probes are presented in section 4.3.



### 4.1 Probe sensitivity

Sensitivity is defined as the amount of change in performance ( $P$ ) for a small change in a parameter ( $x_i$ )[38]. Sensitivity is a linear approximation to the change in performance and is only valid for small parameter changes. Performance changes due to a large change in a parameter can not be predicted accurately with sensitivity analysis. The equation for the sensitivity of  $P$  with respect to  $x_i$  is given by  $S_{x_i}^P$  in (4.1.1). A sensitivity of  $n$  means that a 1% change in a parameter causes a  $n\%$  change in performance.

$$\begin{aligned} S_{x_i}^P &\equiv \lim_{\Delta x_i \rightarrow 0} \frac{\Delta P/P}{\Delta x_i/x_i} \\ &= \frac{x_i}{P} \frac{\partial P}{\partial x_i} \end{aligned} \tag{4.1.1}$$

Sensitivity is often used in the design of filters and other circuits to predict the effect of



non ideal components, environmental changes and ageing. For circuit and filter design, lower sensitivity is better because the circuit performance should ideally not be sensitive to element values. A measurement probe has the opposite requirement. If small changes in sample material causes a large change in measurable performance, the accuracy is higher for the same amount of measurement uncertainty. Ideally a probe is insensitive to all parameters except the one being measured.

The magnitude and phase of the reflected signal from the coaxial line are functions of loss and dielectric constant of the sample.  $S_{\epsilon_r}^{\phi}$  is shown in Figure 4.1(a) and  $S_{\tan \delta}^{\Gamma}$  is shown in Figure 4.1(b). The sensitivity of phase due to changes in loss ( $S_{\tan \delta}^{\phi}$ ) and the sensitivity of magnitude due to changes in relative permittivity ( $S_{\epsilon_r}^{\Gamma}$ ) have also been calculated, but these values are so small that they can be neglected. The probe has a sensitivity of about one for low permittivity samples. The sensitivity decreases when sample permittivity is increased beyond 20.  $S_{\epsilon_r}^{\phi}$  is seen to be unaffected by material loss.

Figure 4.1(b) clearly shows that the probe is insensitive to sample losses. This is one of the great disadvantages of the open-ended coaxial probe and probes in general that rely on reflection measurements only.  $S_{\tan \delta}^{\Gamma}$  increases rapidly when high permittivity, high loss samples are measured, but even here the sensitivity is less than 0.1.

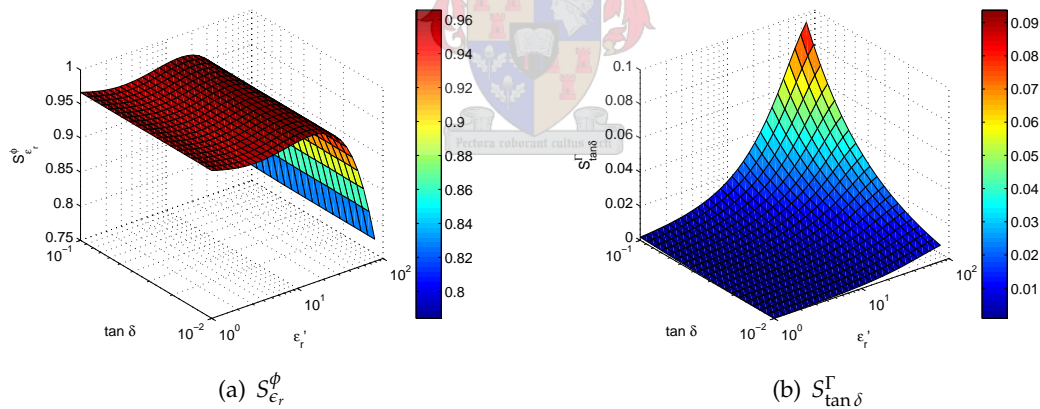


**Figure 4.1:** Sensitivity of SMA probe at 1 GHz.

Sensitivity can be misleading and a related parameter which is often used is the unnormalised sensitivity given by (4.1.2). The unnormalised sensitivity is the actual change in performance compared to the fractional change in performance in normalised sensit-

ivity.

$$US_{x_i}^P = PS_{x_i}^P = x_i \frac{\partial P}{\partial x_i} \quad (4.1.2)$$

$\phi S_{\epsilon_r}^\phi$  is shown in Figure 4.2(a). The unnormalised sensitivity increases with an increase in sample permittivity. Even though the sensitivity is unity for low permittivity materials, the measured phase is small. As the sample permittivity increases the sensitivity decreases, but the measured phase increases. The net effect is that total change in phase increases with an increase in sample permittivity.  $\Gamma S_{\tan \delta}^\Gamma$  is practically the same as  $S_{\tan \delta}^\Gamma$  because the reflection magnitude is close to unity.

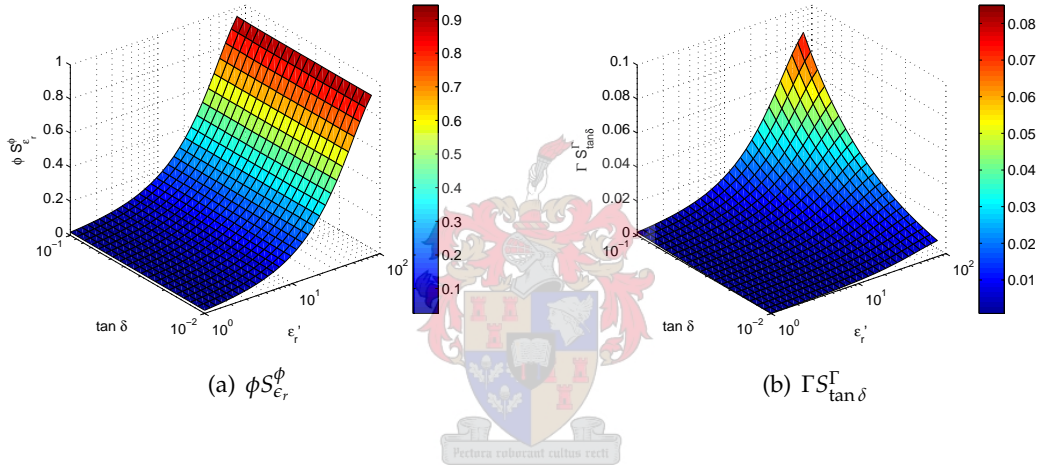


**Figure 4.2:** Unnormalised sensitivity of SMA probe at 1 GHz.

Material loss does not affect the sensitivity greatly and can be removed from the graph. Figure 4.3(a) and 4.3(b) shows the unnormalised sensitivities as a function frequency and sample permittivity. The frequency where the maximum change in performance occurs is given by the empirical formula (4.1.3) derived from these graphs. At  $f_{US_{max}}$  the unnormalised sensitivity is close to one degree.

$$f_{US_{max}} \approx \frac{15(10^7)}{(b-a)\epsilon_r} \quad (4.1.3)$$

The sensitivity of the coaxial probe is seen to be low, but this is expected since it is a broadband measurement technique that relies only on reflection measurements.

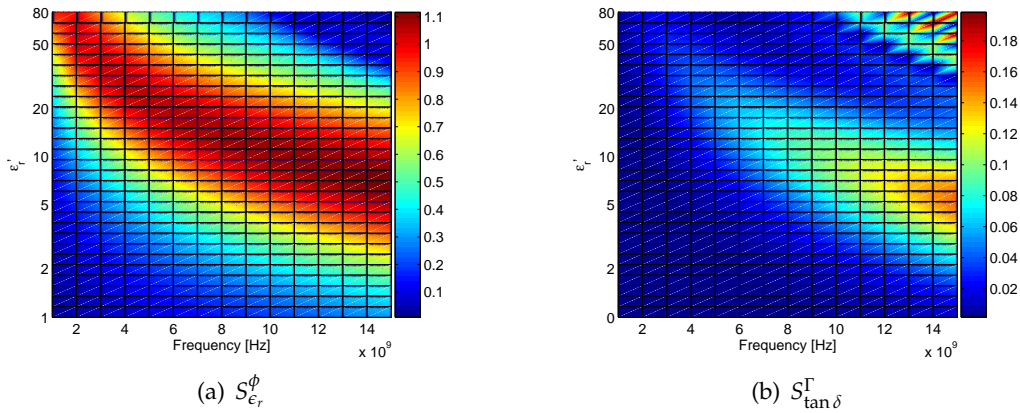


Figure 4.3: Unnormalised sensitivity of SMA probe over frequency and relative permittivity.

## 4.2 Sources of measurement error

### 4.2.1 Frequency range

The open-ended coaxial probe is not able to measure any sample at any frequency. The lower frequency limit is determined by the probe sensitivity and the measurement accuracy. The upper frequency limit is due to radiation.

#### Radiation

It was seen in section 3.2 that all data extraction methods have assumed an infinite sample size, but samples are always limited in size. An infinite sample can be approximated when little electric field exists outside the material under test (MUT) and little radiation occurs. The required sample size is discussed in section 4.2.3. The energy which the probe radiates into the MUT is partly reflected back from the sample walls and degrades the measurements. The problem is actually not radiation, but the limited sample size.

The maximum free space frequency has been chosen so that less than 0.5% of the energy is radiated. This requires that the magnitude of  $S_{11}$  be larger than  $-0.05$  dB in a vacuum. Radiation less than 0.5% is not expected to affect the measurements greatly.

$$S_{11} \geq 20 \log(1 - r) \quad (4.2.1)$$

where

$$r = 0.5\% \quad \text{Percentage allowable radiation}$$

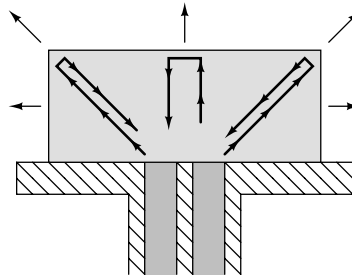
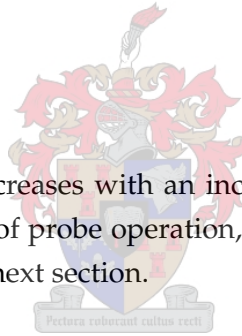


**Figure 4.4:** Illustration of radiated energy in finite size sample.

This formulation is in good agreement with a previously suggested equation by Otto[39]. An equation for the maximum usable frequency where the radiation term can be neglected is given by  $f_{rad}$  in (4.2.2). If high loss samples are measured, the effect of radiation is reduced. The free space maximum frequency can then be exceeded without a reduction in accuracy. Equation (4.2.2) is only valid for coaxial probes without an extended centre pin.

$$f_{rad} \approx \frac{21(10^6)}{(b-a)\sqrt{\epsilon_r}} \quad (4.2.2)$$

The upper frequency limit decreases with an increase in sample permittivity. This reduces the maximum frequency of probe operation, but the lower frequency limit also decreases. This is the topic of the next section.



### Measurement Accuracy

The material parameters can be extracted only as accurate as the measurement is done. Although a probe that is sensitive to the measured parameters can relieve some of the strain on the measurement accuracy, the measurement accuracy ultimately limits the accuracy of the extracted parameters. Inaccurate calibration of the VNA is discussed in detail in the next chapter and will not be repeated here. Even with a good calibration, a VNA has limited accuracy and this affects the extracted material properties.

Figure 4.2(a) shows that the low frequency sensitivity is close to unity. The measured change in phase directly related to the magnitude of the measured phase. The low frequency limit has been chosen as the point where the reflected phase from the probe is approximately 1.5 degrees. Equation 4.2.3 gives an indication of this low frequency limit and its dependence on the sample permittivity. The lower frequency limit decreases in-

versly proportional to the sample permittivity with an increase in sample permittivity.

$$f_{US_{min}} \approx \frac{21(10^5)}{(b-a)\epsilon_r} \quad (4.2.3)$$

### Multiple probes

The upper and lower frequency limit can now be used to determine the bandwidth of the probe. Equation (4.2.4) shows that the coaxial probe has a usable bandwidth of more than a decade. This is a wideband probe, but the low frequency data is not expected to be accurate. The accuracy can be increased by increasing the measured phase.

$$f_{ratio} \approx \frac{f_{rad}}{f_{US_{min}}} = 10\sqrt{\epsilon_r} \quad (4.2.4)$$

There are two ways to increase the measured phase. Larger probes have higher capacitance and thus a greater rate of change in phase when compared to a smaller probe at the same frequency. The capacitance can also be increased by allowing the centre pin to extend into the sample material. This forces more electric field to pass through the sample and thus making the probe more sensitive to sample permittivity. Both these methods lower the maximum frequency of the probe due to radiation, but allows measurement at lower frequencies. The phase of a few probes with different dimensions are shown in Figure 4.5.

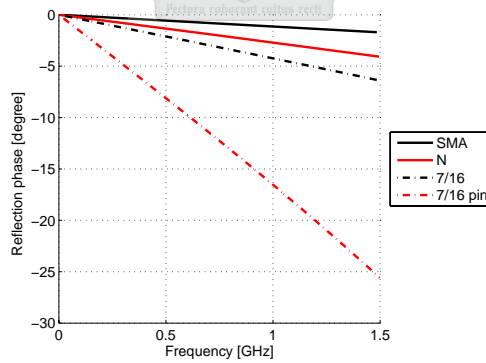


**Figure 4.5:** Simulated phase measurements for different probe sizes and configurations.

### 4.2.2 Finite ground

There has not been much research done on the effect of finite sized flanges for the flat coaxial probe, but the effect of a finite flange size of small coaxial antennas has been investigated[40]. Figure 4.6 shows the change in real and imaginary impedance as a function of ground radius for different pin lengths as predicted by Bahl and Stuchly[40]. The effect of the limited ground plane reduces as the extending centre pin length decreases. For a zero length pin, the required flange radius is small. Simulations have indicated that a flange radius of three times the coaxial line outer radius is sufficient.

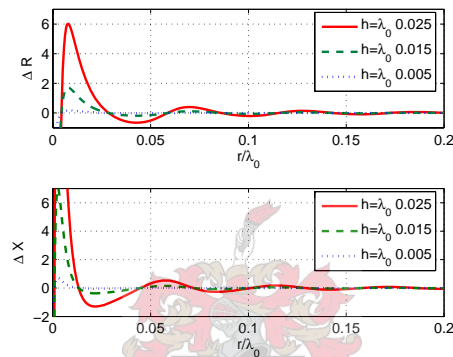


**Figure 4.6:** Change in impedance of a small monopole antenna immersed in water at 2.45 GHz as a function of ground radius.

A probe that has an extended pin requires a larger ground. Bahl and Stuchly found that a ground-plane radius of more than 0.2 of a free space wavelength has a negligible effect on the input impedance of a short monopole when the probe is immersed in water. This would require that a 7/16 size probe with a 10 mm pin should be used with a 0.4 meter ground radius. Such a large ground is impractical. The input impedance of the pin probe is calculated through simulations and the simulations do not have to assume an infinite ground. This enables us to use a smaller ground plane and accurately determine the input impedance of the short monopole.

### 4.2.3 Finite sample size

The requirement of an infinitely large sample can be relaxed by ensuring that the sample is large enough to ensure that most of the electric field is contained in the sample and radiation is negligibly small. Radiation has been kept to a minimum by limiting the maximum frequency of the probe.

The required sample size depends on many factors, but good guidelines can help to eliminate or at least minimise erroneous measurements. Simulations and tests by De Langhe *et al.*[31] have shown that for the probe without a centre pin a sample height of twice the radius of the coaxial outer diameter is sufficient to satisfy an infinite material. De Langhe also simulated the effect of finite size samples in the transverse directions. He used square samples and found that differences in reflection become small even with samples having an area in contact with the probe that is 2.5 times the area of the coaxial aperture. This means that samples with a minimum diameter of 1.5 times the diameter of the coaxial aperture is sufficient. Simulations with CST<sup>®</sup> have confirmed these results. The required sample size is illustrated in Figure 4.7(a).

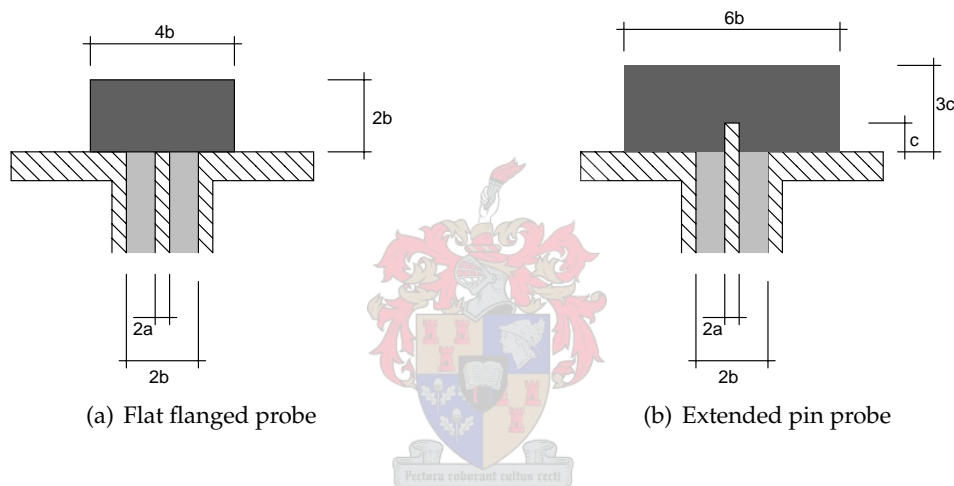


**Figure 4.7:** Illustration of minimum sample size for accurate measurements.

No literature could be found that describes the effect of finite samples when using a coaxial probe with an extended centre pin. The effect of sample size has been investigated in this thesis through simulation with CST<sup>®</sup>. The reflection coefficient has been simulated and the permittivity extracted from the simulated reflection. These are then compared to the actual permittivity of the sample used in the simulation for two distinctive permittivity samples. Figures 4.8(a) and 4.8(b) show the calculated permittivity of two samples with different radii. It is seen that a sample radius that is three times the radius of the outer coaxial conductor is sufficient to ensure a deviation of less than 1.5% in the real part of the permittivity. The imaginary part of the permittivity is affected greatly, but this is due to the probes inability to accurately measure the loss of low loss samples and not due to limited sample sizes.

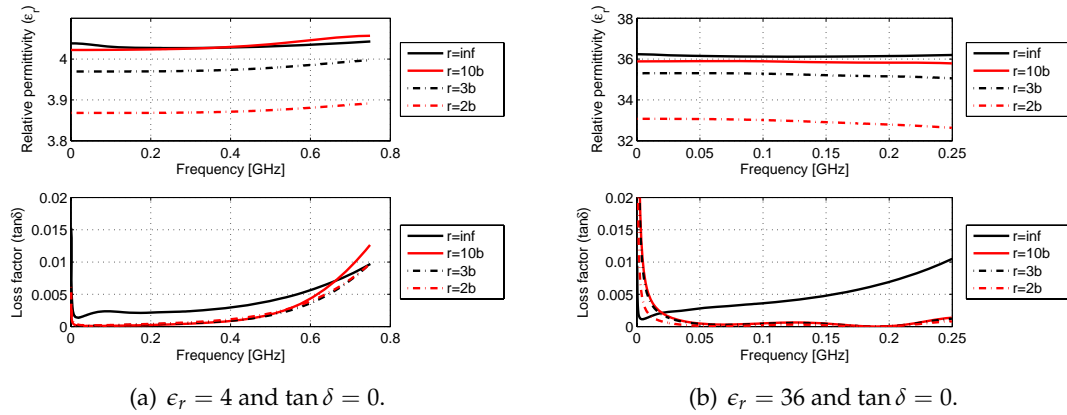


**Figure 4.8:** Calculated permittivity and loss factor for MUT with different radii. The sample height has been assumed to be infinite.

The required height of the test sample for accurate results has also been investigated through simulation in CST<sup>®</sup>. The measurements seem to be less sensitive to the height of the sample. The calculated permittivities for samples of different heights are shown in Figures 4.9(a) and 4.9(b). A sample with a height of at least three times the pin height has deviations in dielectric constant of less than 2%.

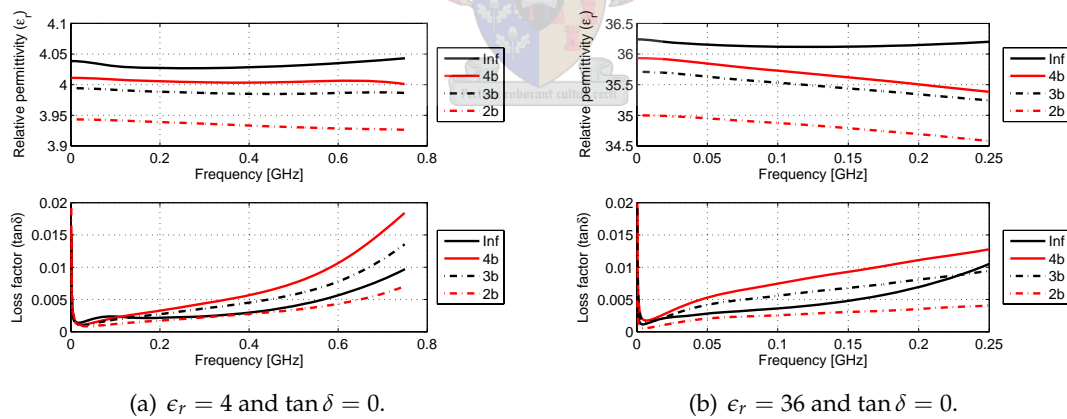


**Figure 4.9:** The calculated permittivity and loss factor for MUT with changing height. The sample radius has been assumed to be infinite in extent.

The effect of a finite sample can also be tested during measurements. When the size of the sample is too small the addition of a metallic object on the sample edge will effect the measurements and the extracted permittivity.



#### 4.2.4 Lift-off & surface roughness

Lift-off is the term used to describe the air gap between the probe and the sample being measured. The same effect is observed when the sample material has a rough surface. If the surface roughness can be measured, an average air gap can be used to model the effect of the rough surface. Lift-off and surface roughness is the greatest restriction of the coaxial probe when measuring solids.

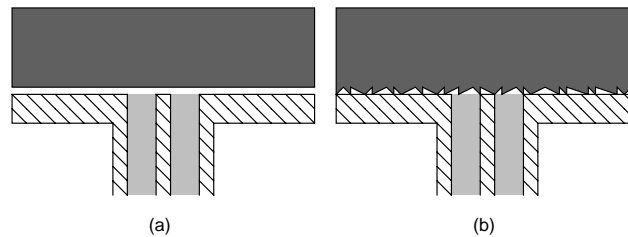


**Figure 4.10:** Illustration of lift-off.

Arai *et al.*[41] found that a sample surface should be polished down to variations less than  $0.5 \mu\text{m}$  to minimise the effect of the air layer and obtain good permittivity extraction. Baker-Jarvis *et al.*[29] also investigated the problem of lift-off in depth and also developed a code to investigate the problem. This code has been used to calculate the reflection coefficient from a SMA-size coaxial probe for two sample materials. The gap between the sample and the probe was varied from 0 to  $10 \mu\text{m}$ . The permittivity was then extracted from these reflections using the full-wave solution without an air gap. The effect on the extracted permittivity is shown in Figures 4.11(a) and 4.11(b).

A  $10 \mu\text{m}$  gap between the probe and a sample with permittivity of  $2(1 - 0.01i)$  causes the extracted permittivity to be 2.5% too low. The same gap between a sample with permittivity equal to  $10(1 - 0.01i)$  causes the extracted permittivity to be more than 15% too low. Clearly lift-off affects the high permittivity sample more. Careful investigation of the extracted permittivity also shows that the lift-off has a slightly greater effect at lower frequencies, but this is a small difference. The extracted loss shows a much greater change, but this could be expected due to the extreme insensitivity of the probe to sample loss. It is interesting to note that the extracted loss increases with an increase in frequency.

Lift-off can be modelled as a series capacitance when the air gap is small. If the lift-off can be estimated with reasonable accuracy, the NIST code can extract the permittivity with the air gap included. The code is slow and time consuming. Since the series capacitance does not change much over frequency, it can be calculated at one frequency and be removed from reflections at other frequencies. This greatly reduces the time required,

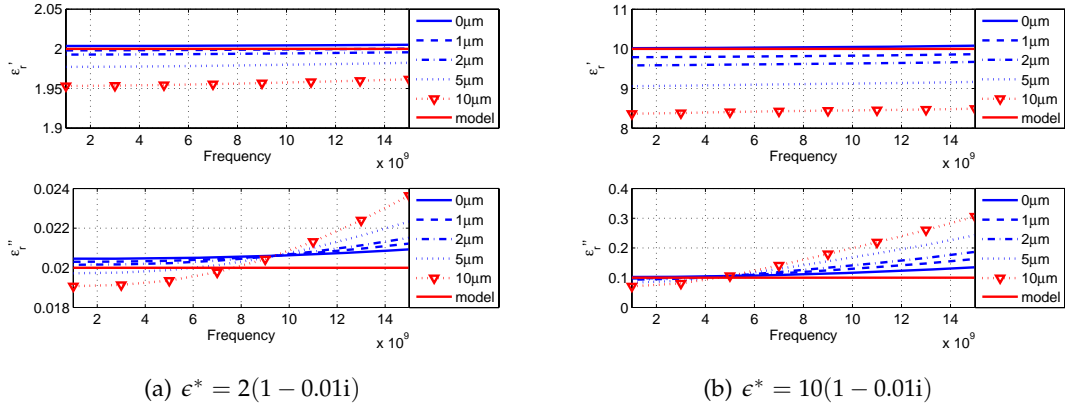


**Figure 4.11:** Effect of lift-off on extracted permittivity for two sample materials.

since only one calculation has to be performed using the forward solution and one extraction using the NIST code. First the reflection at a single frequency is used to extract the sample permittivity with an estimated lift-off. The sample permittivity is then known at that frequency. The extracted sample permittivity is used to calculate the reflection from this sample if there had been no air gap. The series capacitance caused by the air can then be calculated using (4.2.5). The measured reflection is  $\Gamma_m$  and the calculated reflection is  $\Gamma$ .

$$C_s = \frac{1}{i\omega Z_0} \frac{(1 - \Gamma_m)(1 - \Gamma)}{2(\Gamma_m - \Gamma)} \quad (4.2.5)$$

The series capacitance can now be removed from reflections at other frequencies using (4.2.6). The new reflection coefficients are now used to extract the sample permittivity over the entire measured frequency range using the faster code developed in section 3.3.1.

$$\Gamma_{new} = \frac{\Gamma_m(1 + i2\omega Z_0 C_s) - 1}{\Gamma_m i2\omega Z_0 - 1} \quad (4.2.6)$$

The sample should be machined as flat and smooth as possible to reduce the effect of lift-off. The same can be said for the probe, but due to differing thermal expansion coefficients this is not easy to ensure. Great care has been taken to assemble the probe completely and then machine the surface as flat as possible. The surface profile of three probes have been measured and are shown in Figures 4.12(a), 4.12(b) and 4.13. The surface roughness of the PTFE dielectric and ground deviate between 5 and 15  $\mu m$ . The machine used to measure the profiles have a 5  $\mu m$  accuracy and any deviations smaller

than this should be ignored. These profiles show that a sample does not have to be polished down to  $0.5 \mu\text{m}$  unless the probe can be manufactured to the same level of accuracy.

To minimise any errors due to lift-off, a 600 gram weight is placed on all samples. The weight allows a repeatable pressure to be applied to all solid samples.

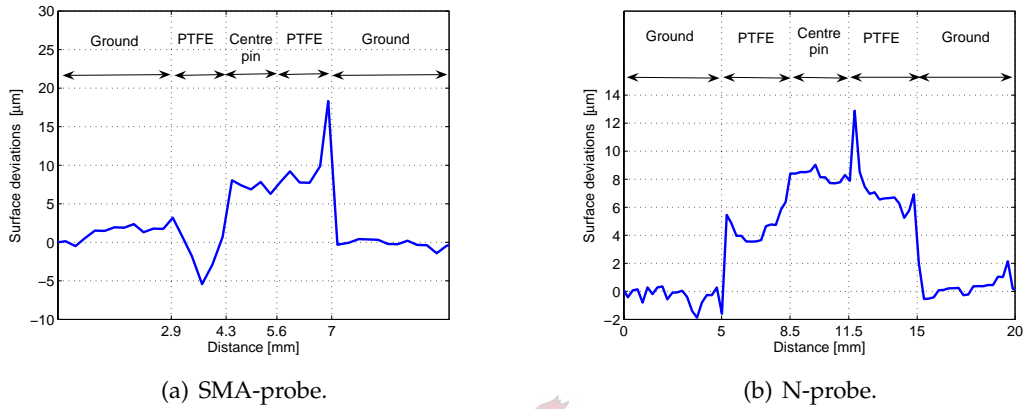


Figure 4.12: Measured surface profiles of the SMA and N-probe.

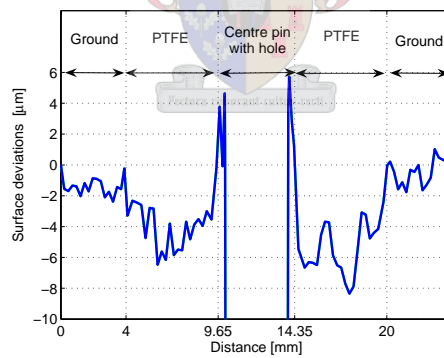


Figure 4.13: Measured surface profile of 7/16 probe.

### 4.3 Design & Construction

Three flat flanged coaxial probes have been developed with increasing dimensions and a fourth probe has an extended centre pin. The construction of these probes is important to ensure comfortable operation when measuring both solids and liquids. Large screws

tighten the calibration standards onto the probes. These screws tighten from the probe face side so that the cables are not in the way. The large base of the probe ensures that the probe set does not move and the cables are hidden to ensure that they are not touched during calibration and measurement. A photograph of the probe set is shown in Figure 4.14.



**Figure 4.14:** Photograph of coaxial probes and the supporting mechanical jig.

The probes have been developed from standard coaxial panel mount receptacles. The three coaxial connectors used are SMA, N and 7/16. These receptacles are then connected to semi-rigid coaxial lines that terminate in a SMA connector. All the probes thus have the same interface to the VNA and the components can be replaced without replacing the entire set-up. The dimensions of the coaxial apertures for these probes are listed in Table 4.1.

The probe frequency ranges in air are listed in Table 4.2. The combination of probes allows measurement over a wide frequency and sample range.

**Table 4.1:** Probe dimensions.

Probe	Pin diameter [mm]	Aperture diameter [mm]	Ground diameter [mm]
SMA	1.3	4.1	55
N	3	10	55
7/16	4.7	16	55

**Table 4.2:** Frequency ranges in air.

Probe	$f_{min}$ [GHz]	$f_{max}$ [GHz]
SMA	1.5	15
N	0.6	6
7/16	0.35	3.5
7/16 + pin	0.15	1.5

The 7/16-size probe converts into a probe with an extended centre conductor. This allows calibration without the pin and then the pin can be inserted afterwards. The pin length is 10 mm high.

#### 4.4 Conclusion

The coaxial probe has been shown to be insensitive to sample materials. The sensitivity of the probe with respect to loss of low loss samples is especially low. This is the price that has to be paid for an extremely wide band measurement. The probe has a bandwidth of more than a decade. This bandwidth is increased even further with an increase in sample dielectric constant.

The factors that can cause measurement errors have been presented and guidelines were given to ensure accurate measurements. Ground plane size is not a great factor for the probe without the extended centre pin, but can cause measurement errors for the extended centre pin probe. Minimum sample size were specified to ensure that most of the electric fields are contained inside the MUT. A fast method for calculating the sample permittivity when the lift-off can be estimated was suggested. This method uses both the fast extraction code developed in chapter 3 and the code developed at NIST.

The low sensitivity of the probe requires that measurements and associated calibrations have to be performed accurately.

# Chapter 5

## Calibration

Measurement accuracy is directly related to the accuracy of the calibration and forms a vital part of the probe design and use. Any measurement errors in turn affect the accuracy of the extracted permittivity. The insensitive nature of the open-ended coaxial probe to sample permittivity necessitates accurate measurements because small errors in the measured reflection coefficient translate into large errors in the extracted permittivity.

Section 5.1 introduces concepts and terminology of calibration. Different calibration procedures and their associated advantages and disadvantages are presented in sections 5.2 and 5.3. The calibration sets are also developed for the coaxial probe geometry. The combination of the two calibration sets allow the residual errors after calibration to be determined in section 5.5. The measured residual errors and system repeatability is then used in section 5.6 to estimate the measurement uncertainty.

### 5.1 Calibration

Calibration is a process whereby repeatable systematic errors can be measured and removed from the system through the measurement of known devices. Calibration is based on a model where the VNA can be considered a perfect reflectometer and all errors in measurement setup and VNA can be lumped together in error boxes[42]. Figure 5.1 illustrates this concept. These error boxes are the parameters that need to be determined during calibration. The process is not a simple normalization, but a mathematical model that calculates the errors by measuring well defined standards and then comparing these measurements to the expected response or calibration definitions[42].

Measurement errors are divided into two groups namely raw and residual errors. Raw errors are further separated into systematic (repeatable), random (non-repeatable)

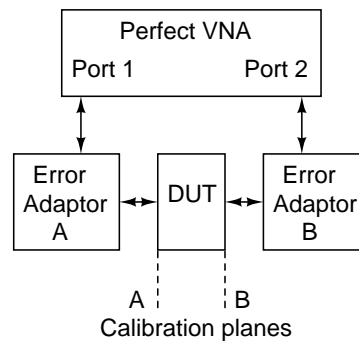


**Figure 5.1:** Graphical representation of a calibration model where all errors are lumped together in error boxes.

and drift errors. Systematic errors are caused by necessary non-ideal elements in the measurement setup that affect the signal being measured. These include losses due to cables, reflections from connectors, time delay and more. Random errors are non-repeatable errors and can not be corrected for, but they can be minimised by using an average of many measurements. Errors due to system drift can also not be corrected, since the system drift after calibration causes the errors.

Any errors in the system after calibration are collectively termed residual errors. Residual errors are caused by incorrect calibration definitions, system drift and repeatability errors. Random errors can also form part of the residual errors when their presence in the error boxes affect subsequent measurements.

Calibration removes the errors from the system due to non ideal elements. This does not mean that low quality devices should be used and then compensated for by calibration. High quality devices and connections are still required for good repeatable measurements. The smaller the error is to start with, the better the error terms can be determined and the less susceptible the system is to drift.

Calibration moves the measurement position or calibration plane closer to the device under test (DUT), so that the measurement ports of the VNA are as close to the measured device as possible. All losses, time delay and imperfect transitions are mathematically removed. It is important to remember that any calibrated measurement is processed data and should be treated as such. Unphysical measurements are possible after calibration due to incorrect compensation of error terms. A typical example illustrates this point. Passive devices can not generate energy and thus the reflections from these devices are always located inside the Smith-chart. Due to overcompensation of losses it is possible that the measurement goes outside the Smith-chart edges.

Although many calibration techniques have been developed over the years, most of

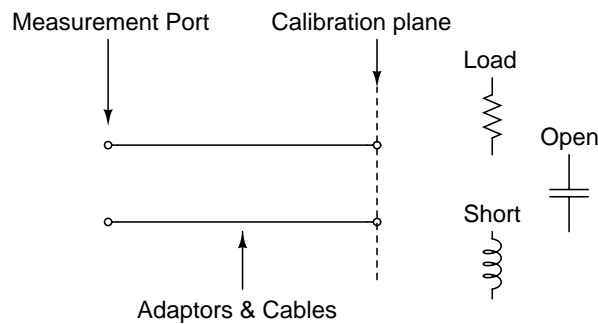


**Figure 5.2:** Graphical representation of a shifted measurement plane. Three SOL standards used during one port calibration are also illustrated.

them are more suited for two-port calibration[43]. These include SOLT, TRL, LRL, LRM, port extensions and many others. These methods differ in accuracy and ease of use, but are all based on the same principle. A number of well known devices are measured and the information used to correct subsequent measurements. Two of these methods, namely SOLT and TRL have been implemented for the coaxial probe geometry. The most common and widely used coaxial calibration technique is SOLT.

## 5.2 SOLT Calibration and Standards

SOLT is an acronym for the four standards used to calibrate a two port system. These standards are *Short*, *Open*, *Load* and *Thru*(through). The acronym TOSM is also often encountered, here the *Load* standard is called a *Match*. A one-port calibration requires only three standards to characterize the error terms. This calibration procedure is named SOL or one-port SOLT, because the THRU standard is not used during calibration. In all sections that follow the calibration standard names, such as SHORT, are written in capitals. This avoids confusion between the standard and the description.

SOLT calibration is the most popular calibration technique for coaxial environments. The standards are easily connected and torqued for repeatable measurements over a wide frequency range. The calibration procedure and mathematics are simple to understand and apply.

The three standards used for calibration can, in theory, have any reflection as long as they are distinct. In practice, the error terms are better determined when the standards are as distinct as possible. This means that the three standards should be spaced as far as possible from each other on a Smith-chart. The recommended locations on a Smith-chart for the three standards are shown in Figure 5.3.



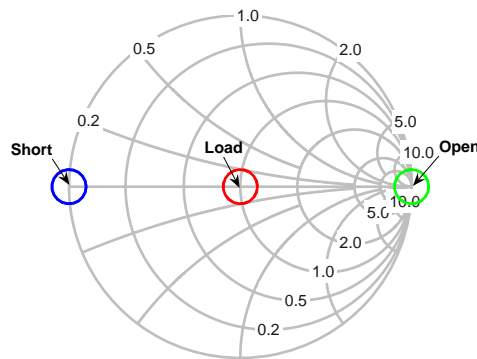


Figure 5.3: Smith-chart showing the position of the SHORT, OPEN and LOAD standards.

### 5.2.1 Specifying SOL calibration standards for 8510c VNA

Vector network analysers are able to perform calibration on measured data and then display the error corrected values. This allows the user to inspect the results during the measurements. The calibration standards have to be defined to the VNA in order to do corrections. These descriptions are known as calibration definitions. The Hewlett Packard 8510c VNA calibration definitions for the three coaxial terminations are presented in order to understand the restrictions of on-line VNA calibration[42].

All of the standards can be specified with an offset and some offset loss. A table of coefficient values for the SOL standards is supplied in Appendix B on page 124.

#### LOAD

The LOAD standard definition is either a perfect matched termination or an arbitrary constant impedance. It is impossible to describe an arbitrary changing load on a 8510c VNA. This requires that calibration be performed with a matched or a constant impedance termination. The LOAD has to be a high quality LOAD to ensure that the calibration definition and the standard is in good agreement. Kwan[44] found that the accuracy of the LOAD standard greatly effects the residuals source match error. A high quality LOAD can be simulated using a sliding load. The sliding load causes the error vector to rotate around the centre of the Smith-chart so that a perfectly matched termination can be emulated by determining the centre of the measured reflection circle. The quality of the LOAD standard then becomes a function of the load geometry and not the termination itself.

**OPEN**

The OPEN standard is defined by a cubic polynomial for the capacitance. Losses and radiation are neglected. The capacitance equation is given by (5.2.1). The reflection from the OPEN standard is converted to an impedance and then the polynomial is fitted to best describe the capacitance.

$$C(f) = C_0 + C_1f + C_2f^2 + C_3f^3 \quad (5.2.1)$$

where

$f$  Frequency [Hz]

$C_0$  Capacitance coefficient [ $10^{-15}$ F]

$C_1$  Capacitance coefficient [ $10^{-27}$ F/Hz]

$C_2$  Capacitance coefficient [ $10^{-36}$ F/Hz<sup>2</sup>]

$C_3$  Capacitance coefficient [ $10^{-45}$ F/Hz<sup>3</sup>]

**SHORT**

The SHORT standard definition is similar to the OPEN standard, except the cubic polynomial describes the inductance of the SHORT standard. The polynomial is given by (5.2.2).

$$L(f) = L_0 + L_1f + L_2f^2 + L_3f^3 \quad (5.2.2)$$

where

$f$  Frequency [Hz]

$L_0$  Capacitance coefficient [ $10^{-9}$ H]

$L_1$  Capacitance coefficient [ $10^{-24}$ H/Hz]

$L_2$  Capacitance coefficient [ $10^{-33}$ H/Hz<sup>2</sup>]

$L_3$  Capacitance coefficient [ $10^{-42}$ H/Hz<sup>3</sup>]

**5.2.2 Two-tier SOL calibration**

Two-tier SOL calibration is, as the name suggests, a process where the calibration is done after the measurement has been completed. This means that the VNA calibration is not used. This type of SOL calibration is used when the VNA can not adequately describe the calibration standards. A good example would be the use of water or some other reference material as a LOAD standard. Two-tier calibration can also be used when a high quality

LOAD is not available, but the LOAD response is known or can be determined. The three standards are measured along with the DUT. These measurements are then used later to correct the DUT measurement to obtain the DUT characteristics at the calibration plane. The obvious disadvantage is that the calibration and measurements can only be viewed off-line, once the measurements have been completed.

The error model for a one-port system is shown in Figure 5.4. The equation describing this system in terms of the three error terms, the measured reflection and the device reflection is given by (5.2.3)[43].

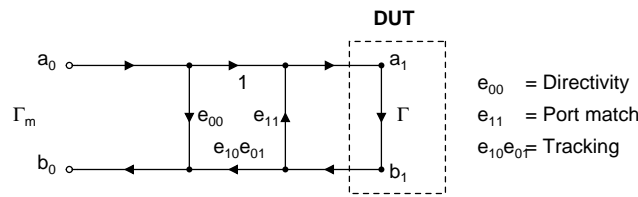


Figure 5.4: Error model of an one-port system.

$$\Gamma_M = \frac{e_{00} - \Gamma(e_{00}e_{11} - e_{10}e_{01})}{1 - e_{11}\Gamma} \quad (5.2.3)$$

Measurement of three distinct known devices, or standards, allows three equations to be solved for the three unknown error terms. The solution to the three equations are given by (5.2.4), (5.2.5) and (5.2.6).

$$e_{11} = \frac{\Gamma_1(\Gamma_{M3} - \Gamma_{M2}) + \Gamma_2(\Gamma_{M1} - \Gamma_{M3}) + \Gamma_3(\Gamma_{M2} - \Gamma_{M1})}{\Gamma_1\Gamma_2(\Gamma_{M1} - \Gamma_{M2}) + \Gamma_1\Gamma_3(\Gamma_{M3} - \Gamma_{M1}) + \Gamma_2\Gamma_3(\Gamma_{M2} - \Gamma_{M3})} \quad (5.2.4)$$

$$e_{00} = \frac{\Gamma_{M2}\Gamma_{M3}(\Gamma_1(\Gamma_3 - \Gamma_2)) + \Gamma_{M1}\Gamma_{M3}(\Gamma_2(\Gamma_1 - \Gamma_3)) + \Gamma_{M1}\Gamma_{M2}(\Gamma_3(\Gamma_2 - \Gamma_1))}{\Gamma_1\Gamma_2(\Gamma_{M1} - \Gamma_{M2}) + \Gamma_1\Gamma_3(\Gamma_{M3} - \Gamma_{M1}) + \Gamma_2\Gamma_3(\Gamma_{M2} - \Gamma_{M3})} \quad (5.2.5)$$

$$e_{10}e_{01} = \frac{(\Gamma_2 - \Gamma_3)(\Gamma_1 - \Gamma_3)(\Gamma_1 - \Gamma_2)(\Gamma_{M2} - \Gamma_{M3})(\Gamma_{M1} - \Gamma_{M3})(\Gamma_{M1} - \Gamma_{M2})}{[\Gamma_1\Gamma_2(\Gamma_{M1} - \Gamma_{M2}) + \Gamma_1\Gamma_3(\Gamma_{M3} - \Gamma_{M1}) + \Gamma_2\Gamma_3(\Gamma_{M2} - \Gamma_{M3})]^2} \quad (5.2.6)$$

These three error terms can now be used to correct any measured reflection to find the reflection from the DUT. The equation for the reflection from the DUT is given by (5.2.7).

$$\Gamma_{DUT} = \frac{\Gamma_M - e_{00}}{\Gamma_M e_{11} - (e_{00}e_{11} - e_{10}e_{01})} \quad (5.2.7)$$

Two-tier SOL calibration does what the VNA usually automatically does for the user, but does not have the restrictions enforced by the VNA.

### 5.2.3 SOL standards

SOL calibration standards have been built in-house and a photo of the standards is shown in Figure 5.5. These standards have been developed to fit on the face of the coaxial probe so that calibration is done at the measurement plane. The standards have locating pins that fit in small holes in the probe to help with alignment and improve repeatability. The standards have also been designed so that they are tightened from the top to prevent cable movement.

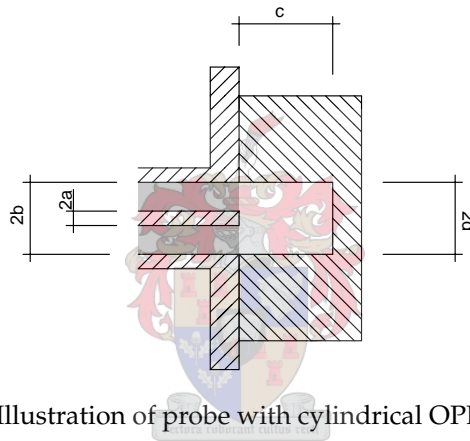


Figure 5.5: Photograph of coaxial probe standards used for SOL calibration.

#### OPEN standard

The OPEN standard that is most commonly used for coaxial probes is simply the probe open into air. This standard generally has radiation and is also susceptible to microwave interference from outside sources. Although the radiation is extremely low at the frequencies of operation, it was decided to remove the radiation term completely. The elimination of the radiation allows the standard to be described by a lossless capacitance as required for the HP8510c VNA.

Otto and Chew[39] suggested the use of a coaxial line terminating into a shorted cylindrical transmission line as depicted in Figure 5.6. This standard ensures that no energy is radiated and prohibits any microwave interference from outside sources effecting the calibration. The reflection coefficient of the cylindrical cavity is calculated through a mode matching method by considering a TEM wave and any number of  $TM_{0n}$  modes inside the coaxial line. Only  $TM_{0n}$  modes are assumed to exist inside the cylindrical cavity. The absence of an inner conductor in the cylindrical cavity prevents a TEM mode in the cavity. The calculations by Otto and Chew were only for situations where the dielectric inside the coaxial line and the cavity are identical. The calculation is easily adapted for general coaxial lines and cavity materials. The calculation of the reflection from the OPEN standard is presented in Appendix A.1.



**Figure 5.6:** Illustration of probe with cylindrical OPEN standard.

Three OPEN standards have been developed, one for each probe. The diameter of the cylindrical cavity is the same as the outer diameter of the coaxial lines. The cavity depth for all the OPEN standards have been chosen as 10 mm. The depth of the cavity is not a sensitive parameter as long as it is large.

Figure 5.2.3 shows the measured and calculated reflection from the SMA probe with OPEN standard. The OPEN standard for the SMA probe was measured after a careful TRL calibration (this calibration is discussed in section 5.3). The calculated and measured values are in excellent agreement. This serves as a confirmation of the calculations and the mode matching method used to calculate the reflection coefficient.

A second "test" standard can be constructed where the depth is a fraction of a millimetre, compared to the 10 mm cavity of the OPEN standard described above. This standard can then be used to test the calibration since the capacitance is much higher for the short cavity, but the radiation is still suppressed. When high permittivity samples

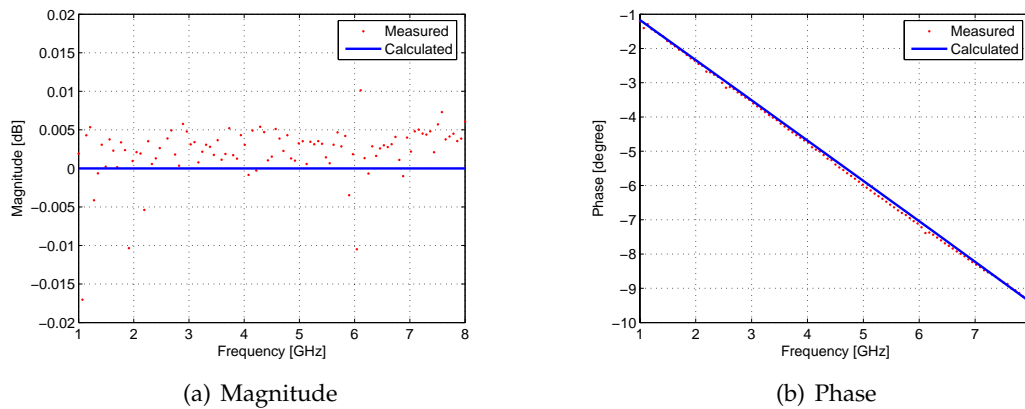


**Figure 5.7:** Measured response of OPEN standard compared to calculated response.

are to be measured the standard can also be used during calibration instead of the the usual OPEN standard. The capacitance used in the calibration is then closer to the expected measured capacitance and thus greater accuracy can be achieved. Construction tolerances are important for this standard, since small changes in cavity depth have a large influence on the measured capacitance. This standard has not been built due to time constraints.

### Short standard

A SHORT standard should supply a good short circuit path between the probe's centre and outer conductor. Wei and Sridhar[45] used mercury as a SHORT standard. This would definitely eliminate contact problems, but Mercury has a few drawbacks. Mercury must be handled with care and good ventilation is necessary to minimize human exposure to mercury vapour. The probe also has to be cleaned once the standard has been measured.

An easier to handle, inexpensive SHORT standard has been used instead. The SHORT standard is an aluminium foil on sheet cardboard. The cardboard is then mounted on a solid metal block. The combination of the rigid metal block and the slightly deformable cardboard ensures that a good repeatable short is established. Earlier versions of the SHORT standard consisted only of the metal block, but occasionally the SHORT did not make good contact with the probe. This caused great problems during calibration and also subsequent measurements. The SHORT standard along with the probe is illustrated in Figure 5.8.

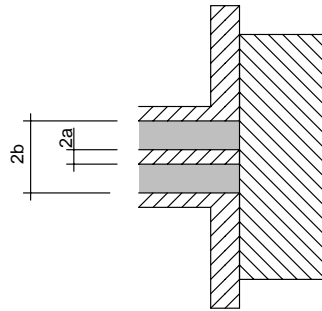


**Figure 5.8:** Illustration of probe with SHORT standard.

No attempt has been made to estimate the losses due to the current in the SHORT and the standard is assumed to have zero inductance as would be expected for a perfectly conducting sheet. The SHORT standard was measured after performing a careful TRL calibration to determine the validity of the assumptions. The measured reflection is shown in Figures 5.9(a) and 5.9(b). The SHORT is not as perfect as was assumed. The losses remain almost constant with frequency, but the inductance increases fast at frequencies above 5 GHz. The deviation is not too much and the effect of this deviation on the calibration is not expected to be great. The most important standard is the LOAD standard and for coaxial probe measurements, the OPEN standard greatly affects low permittivity measurements.

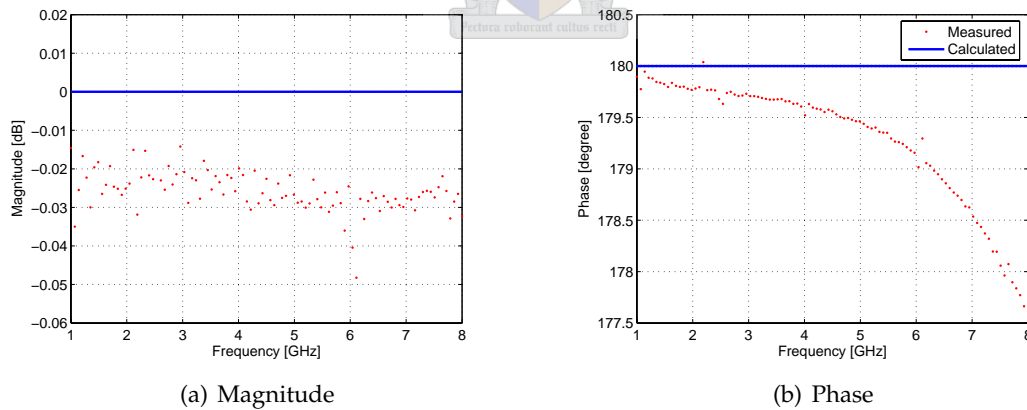


**Figure 5.9:** Measured response of SHORT standard compared to ideal response.

### Load standard

The LOAD standard allows a lot more options than the other two standards. Some authors have suggested the use of well defined materials for calibration, while others emphasized the importance of using many materials for the calibration so that an average of these can be used. A great advantage of using materials for calibration is the fact that measurement accuracy is improved when the measured reflection is similar to one of the calibration standards. This means that calibrating with water when a sample with high water content is to be measured improves the accuracy compared to the same measurement that has been calibrated with a low permittivity sample. Misra *et al.*[46] have expressed their concerns about these possibly incorrect calibrations that produce good results. This incorrect calibration can lead to incorrect cancellation of resonance-type reflections. Materials can deteriorate over time and also become contaminated. They also require temperature controlled storage. Methanol has been reported to have a 0.8% change in dielectric constant for a change in temperature of 1°C[3]. Reference liquids were used in the past due to difficulties in manufacturing a matched termination.

These difficulties have been overcome and a LOAD has been built in-house as suggested by Rimbi[8]. The matched LOAD is manufactured from a commercially available matched termination. The centre pin is spring loaded to ensure a good contact at all frequencies. This method is better than using a reference material, since uncertainty in the permittivity of the reference material is removed. This standard also allows for easy storage and calibration when compared to other possible calibration standards. The LOAD standard along with the probe is illustrated in Figure 5.10(a). A 7/16 size termination could not be found from any of the distributors. The N LOAD standard can be used for both the N and 7/16 probe. Due to dimension differences, the N LOAD on the 7/16 probe has a configuration as shown in Figure 5.10(b). This definitely influences the quality of the LOAD and should be kept in mind during data evaluations.

The disadvantage of this LOAD is the limited quality of terminations that are available from manufacturers. The terminations are specified to have a voltage standing wave ratio of 1.05 (equivalent to a -26 dB termination). The effect of this uncertainty is investigated in detail in section 5.6. An accuracy of -26 dB is not good enough for most coaxial probe measurements. If the response of the termination can be measured, this can be used during two-tier SOL calibrations. It is thus possible to have a highly repeatable, robust LOAD that does not deteriorate with time without sacrificing accuracy. The SMA LOAD standard has been measured after a careful TRL calibration. The measured reflection magnitude is shown in Figure 5.11(a) and a Smith-chart with the LOAD response is shown in Figure 5.11(b). Due to time constraints, TRL calibration standards have not



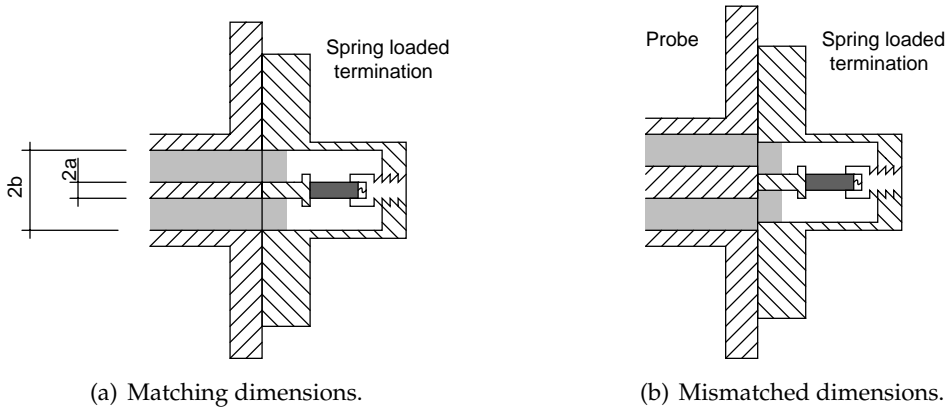


Figure 5.10: Illustration of LOAD standards.

been developed for the other two probes. They have to be assumed perfect or can be estimated by using other materials for calibration.

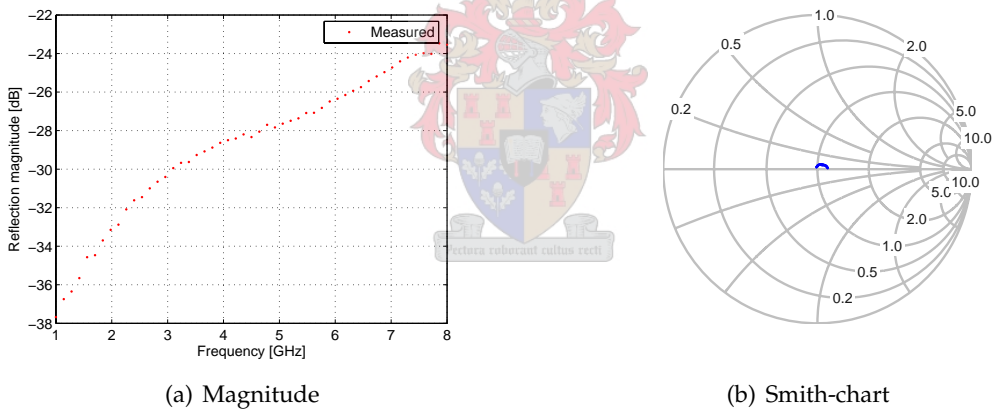


Figure 5.11: Reflection from SMA LOAD standard.

### 5.3 TRL Calibration and Standards

TRL calibration or self calibration is a two port calibration procedure that was first suggested by Engen and Hoer[47] in 1979. It uses three standards to determine the the unknown error terms, where two-port SOLT calibration would require four standards. TRL calibration is considered the most accurate calibration technique when high quality

standards, cables and connectors are used. This accuracy stems from the simplicity of the three standards. The three standards are a *Thru*, *Reflect* and *Line* that form the acronym TRL. Other variations on TRL calibration have also been suggested. These include LRL (Line-Reflect-Line), LRM (Line-Reflect-Match) and TRM (Through-Reflect-Match).

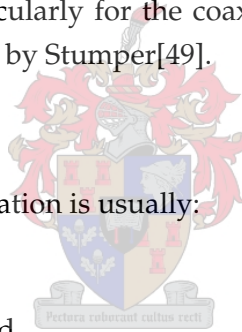
TRL calibration is mostly used in non-coaxial transmission line environments due to difficulty of realizing SOLT standards for these environments. The great power of TRL calibration is the ease of making the calibration standards and the fact that the standards do not need to be known exactly. Only one well defined TRL standard is required since 16 measurements are made to quantify 12 error terms[48].

TRL calibration makes a few assumptions that have to be kept in mind. All standards have to have the same characteristic impedance, because the measured s-parameters are calculated in the characteristic impedance environment of the LINE standard. This is not a great restriction for coaxial geometries since the impedance is not sensitive to the line geometry. The THRU and LINE standards are assumed to have perfect transitions. This could be quite a restriction, particularly for the coaxial probe. The effect of imperfect transitions have been investigated by Stumper[49].

### 5.3.1 TRL standards

The standards used for TRL calibration is usually:

- Zero length THRU
- Correct length LINE standard
- Identical REFLECT standard on both ports



Each of these standards are presented with the model that describes them in the TRL calculation.

#### THRU Standard

The THRU standard is a zero length THRU. The standard is not physically built and is realised by placing the two coaxial probes face to face. The model for the THRU standard used by the TRL calibration is given by (5.3.1). Here it is clearly seen that a perfect transition is assumed.

$$[S_{THRU}] = \begin{bmatrix} 0 & 1 \\ 1 & 0 \end{bmatrix} \quad (5.3.1)$$

The transition between the probes has been measured by utilising a time domain gate

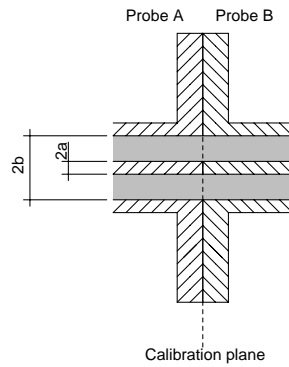
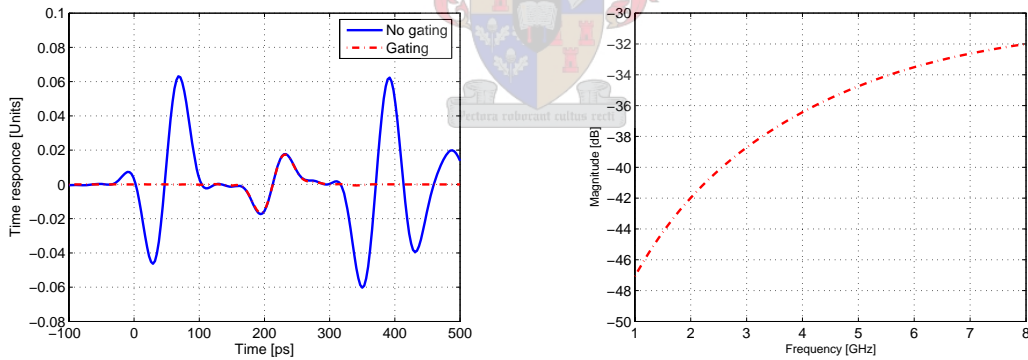


**Figure 5.12:** Illustration of probes forming the THRU standard.

over the transition after performing a SMA SOLT calibration up to the probe edges. The measurements are shown in Figure 5.13(a) and 5.13(b). The transition deteriorates with frequency, but is surprisingly good at low frequencies. The gated response of the SMA transition to the probe ground is shown in Figure 5.14. It is interesting to note that the reflection from the SMA-Probe transition is approximately 10dB larger than the transition between the probes. Fortunately the SMA-Probe transitions are calibrated out of the measurements.



(a) Time domain reflection from THRU connection.

(b) Frequency domain response of gated THRU.

**Figure 5.13:** Time and frequency domain response of the THRU standard.

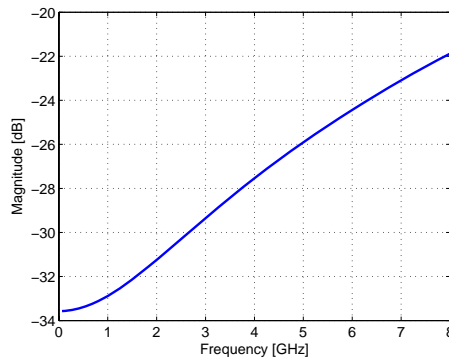


Figure 5.14: Frequency response of SMA transition.

### REFLECT Standard

The reflect standards do not have to be known accurately. Ideally the reflection should have a unity reflection magnitude. The standards only have to be known within a quarter wavelength and both standards have to be identical.

$$S_{11} = S_{22} \quad (5.3.2)$$

The REFLECT standard has been chosen as a shorted cavity. It was found that the OPEN standard is easier to realise than a SHORT standard due to contact issues. The standard has identical cylindrical cavities on both sides and also has locating pins for easy alignment. This allows the standard to be connected and then both ports calibrated without interruption. The diameter of the cavities has been made slightly larger than the outer diameter of the coaxial line. This reduces the effect of small misalignments and thus improves accuracy. The capacitance from the cavities has been calculated using the adapted solution by Otto and Chew[39]. Only the first term of the capacitance polynomial has been included since this is enough to describe the reflection to within a quarter wavelength. Figure 5.15 illustrates the reflection standard.

### LINE Standard

The LINE standard is a coaxial transmission line that is placed between the two probes. The exact propagation characteristic is not required, but an approximate time delay has to be specified during calibration.

$$[S_{LINE}] = \begin{bmatrix} 0 & e^{-\gamma l} \\ e^{-\gamma l} & 0 \end{bmatrix} \quad (5.3.3)$$

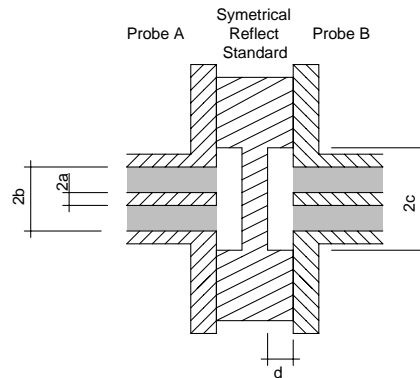


**Figure 5.15:** Illustration of probes with the REFLECT standard.

Accurate calibration requires that the phase change of the line standard should be between -20 degrees to -160 degrees. Phase deviations that are out of these limits cause the LINE and THRU standards to become electrically similar. This is analogous to doing a SOLT calibration, where two of the standards are close on a Smith-chart. This places a 8:1 bandwidth restriction on single LINE TRL calibrations. The calibration is the most accurate at the geometric mean of the upper and lower frequency or where the LINE standard has a -90 degree phase deviation. Closer to the edges of the frequency range the calibration becomes less accurate.

A single LINE standard has been designed to work from 1 GHz to 8 GHz. The required line length is calculated from (5.3.4)[42]. The LINE standard is illustrated in Figure 5.16. The LINE standard is 11.5 mm long and a electrical delay of approximately 54 pico seconds.

$$L = \frac{15(10^7)}{\sqrt{2.1}(f_1+f_2)} \quad (5.3.4)$$

The model of the LINE standard assumes perfect transitions as can be seen in (5.3.3). These transitions have been measured and the quality of the transitions are similar to the transition measured for the THRU standard.

## 5.4 Alternative calibration procedures

The difficulties of building calibration standards in-house have been overcome, but the quality of these standards do not compare to commercially available calibration kits. Other calibration methods where commercially available calibration kits can be used is briefly presented.

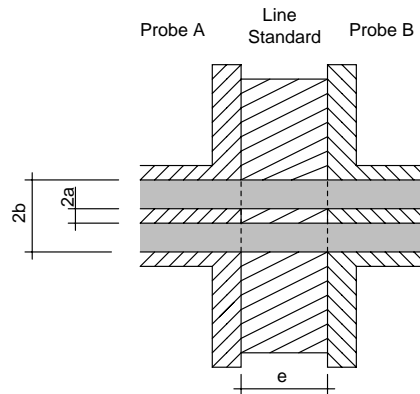


Figure 5.16: Illustration of probes with the LINE standard.

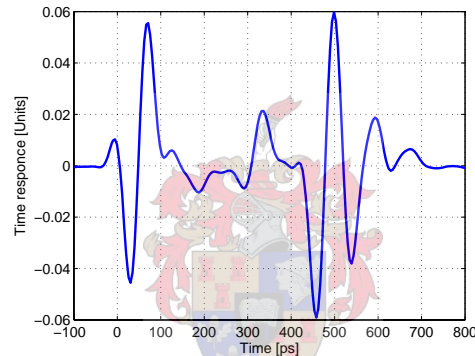


Figure 5.17: Time domain response of the LINE standard.

Figure 5.18 illustrates a possible calibration configuration. The adapter fits onto the coaxial probe and allows commercially available calibration kits to be connected to the other side. The difficulty with this method is that the adapter has to be well characterised in order to remove any delay, loss and reflections. Simple port extensions are not expected to achieve the required accuracy in calibration.

## 5.5 Calibration repeatability and verification

After every calibration a verification should be performed to gain confidence in the measurement integrity, but this requires high quality standards that have not been used in the calibration procedure[48]. Usually calibration consistency checks and repeatability measurements are the only tests that are performed. These are not verifications, but they can indicate if something has gone wrong during calibration. Bad self-consistency data in-

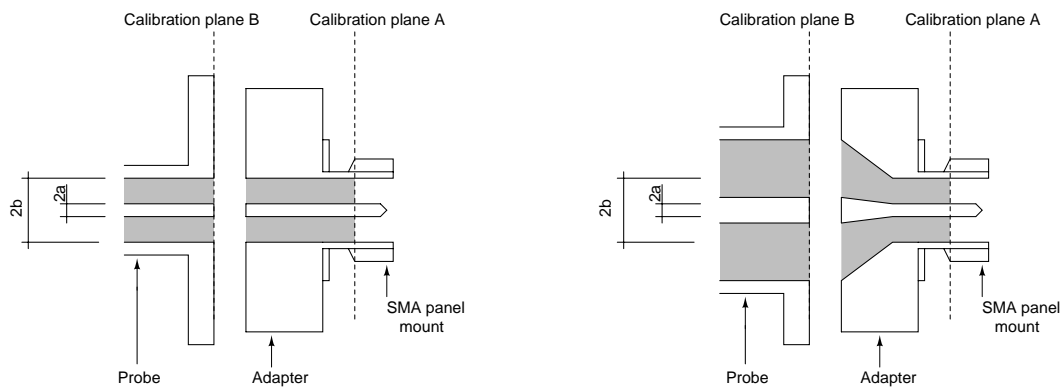


Figure 5.18: Other ways to calibrate.

indicate an incorrect calibration, but good self-consistency data does not guarantee correct calibration.

### 5.5.1 Repeatability

Repeatability of the system is checked by measuring and saving the reflection from one of the standards after calibration without dismantling the setup. The connection between the standard and the probe is then broken, reconnected and remeasured. The difference between the measurements is known as the repeatability. This is an indication of the errors introduced into the system by changing the connections.

Repeatability is the largest factor limiting the calibration effectiveness[48] because there is no way to remove errors due to repeatability problems. The repeatability of the SMA coaxial probe has been measured using the LOAD standard and the results are shown in Figure 5.19. The measurements show that the measurements are repeatable down to -60 dB. This means that measurements can be made with the probe with a repeatability of at least -50 dB, 10 dB higher than the measured repeatability. The repeatability of the LOAD was measured on several occasions and the results were always below -60 dB. The LOAD standard was used to do repeatability measurements because this standard has moving parts, thus being the most unrepeatable standard in the calibration kit.

### 5.5.2 Verification

Verification refers to the process of checking the quality of the calibration. Verification is possible using a combination of the TRL and SOL standards that have been built. Calibration standards in the one procedure can be used to verify the other calibration. After a

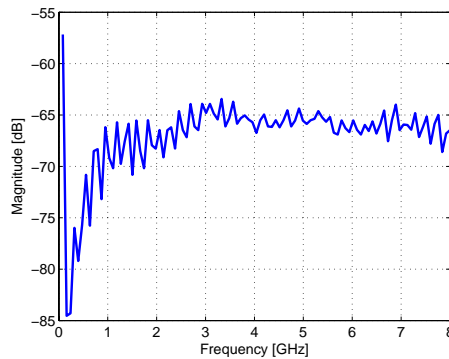


**Figure 5.19:** Measured repeatability of SMA coaxial probe using the LOAD standard.

TRL calibration, the SOL standards can be measured and compared to expected results. After a SOL calibration, the TRL standards such as the coaxial line and probe can be used to verify the calibration.

The quality of the calibration is directly related to the quality of the standards used during calibration. In the same way, the quality of the verification is directly related to the quality of the standards used for verification. Usually high quality air lines and sliding loads are used for verification. Unfortunately such high quality standards are not available for the coaxial probe geometry. The results obtained from the calibration verification has to be viewed critically and compared to the quality of the standards.

An estimate of the residual errors in the measurement setup can be obtained by measuring the residual directivity and source mismatch. The first and significant second order error terms that contribute to systematic errors are given by (5.5.1)[50]. Figure 5.4 shows the error model of systematic errors in a one-port measurement. Equation (5.5.1) assumes that the VNA is operated such that the dynamic range does not add to the systematic errors.

$$e_r = e_{00r} + e_{10r}e_{01r}\Gamma + e_{11r}\Gamma^2 \quad (5.5.1)$$

It is seen that measurements on the edge of the Smith-chart ( $\Gamma \approx 1$ ) are the most difficult to perform accurately. When the reflection magnitude is close to unity, all the error terms are present in the measurements. Unfortunately coaxial probe measurements are highly reflective.



### Residual directivity error

Residual directivity error can be measured by noting that it is the only systematic error present when a perfectly matched termination is connected to the test port.

$$e_r = \lim_{\Gamma \rightarrow 0} [e_{00r} + e_{10r}e_{01r}\Gamma + e_{11r}\Gamma^2] = e_{00r} \quad (5.5.2)$$

The reflection from a perfectly matched termination is zero. Measuring an independent good matched termination after calibration would reveal the residual directivity error. The matched termination is moved away from the calibration plane by connecting a high quality transmission line between the termination and the test port. Any reflected signals then add constructively and destructively with a change in frequency. This produces a periodic ripple in a frequency domain measurement. A longer transmission line produces more frequent ripples.

Residual directivity is 6 dB less than the peak of these ripples unless the verification termination is better than the calibration LOAD[51]. In this case no ripple is observed and the residual directivity is the measured reflection. An illustration of the expected measurement is shown in Figure 5.20(a).

Residual directivity measurements of both the SOL and TRL calibrations have been performed. These measurements are shown in Figure 5.20(b). Due to the relatively large reflections from the SMA-Probe transitions the measurements do not give an indication of the residual directivity. The measured residual directivity is of the same magnitude as the SMA-Probe transitions. See Figure 5.14 for the measured magnitude response of the SMA-Probe transition. The quality of the standards used for verification is the limiting factor.

### Residual source match error

Residual source match can not be measured directly, but the sum of all the errors can be measured by connecting a highly reflective standard to the test port. The residual source match can then be determined by subtracting the other error terms if they are known.

$$\begin{aligned} e_r &= \lim_{\Gamma \rightarrow 1} [e_{00r} + e_{10r}e_{01r}\Gamma + e_{11r}\Gamma^2] \\ &= e_{00r} + e_{10r}e_{01r} + e_{11r} \end{aligned} \quad (5.5.3)$$

The reflection from a lossless OPEN or SHORT standard is unity. Added to this unit vector are the error terms in (5.5.3). If the SHORT or OPEN standard is connected to the system via a high quality transmission line, the unit vector rotates along the edge

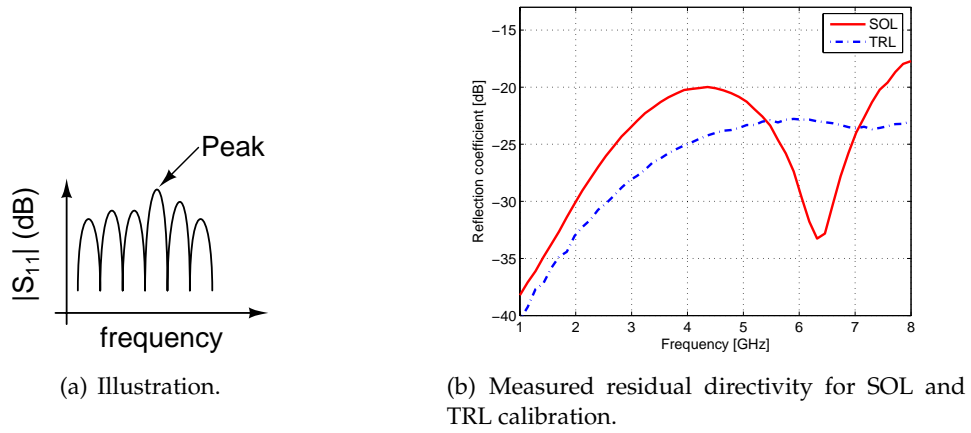


Figure 5.20: Residual directivity error.

of the Smith-chart as the distance to the generator changes with respect to frequency. At the same time the error vector also rotates. The vector sum of these two vectors is measured. The measurement is a sinusoidal variation in magnitude close 0 dB. The size of the error vector can then be determined by measuring the magnitude of the ripple and substituting  $\Delta$  into (5.5.4)[51]. A graphical representation is shown in Figures 5.21(a) and 5.21(b).

$$e_{rsm} \approx \frac{1 - 10^{-\Delta/20}}{1 + 10^{-\Delta/20}} \tag{5.5.4}$$

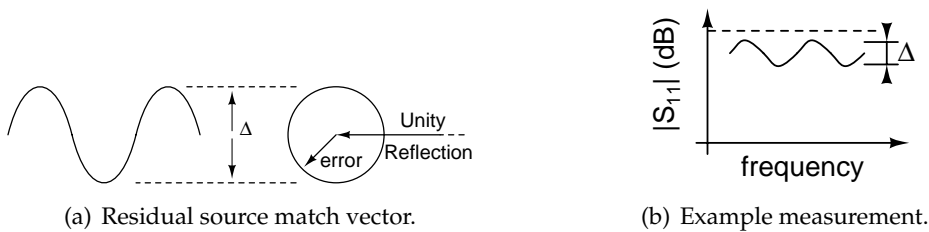


Figure 5.21: Residual source match error measurement.

The total residual error has been measured for both the SOL and the TRL calibrations. The other error terms are usually an order of magnitude lower than the residual source match[52]. The residual source match error can thus be said to be approximately

equal to the measured error. The measurements are shown in Figure 5.22. The residual source mismatch is approximately -24 dB for the SOL calibration and -50 dB for the TRL calibration. A residual source match mismatch less than -44 dB is considered a good calibration[52]. This shows that the on-line calibration by the VNA can not be used unless an accurate matched termination is used as the LOAD standard.

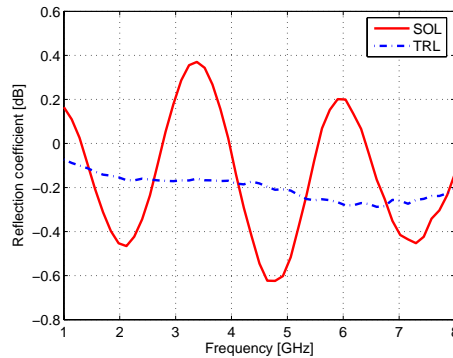


Figure 5.22: Measured residual error for SOL and TRL calibration.

## 5.6 Uncertainty and Accuracy

Every measurement has an associated error and uncertainty[53]. The difference between error and uncertainty is important. Uncertainty refers to the deviation in results observed by repeated measurements by the same person, measurement device, sample and conditions at different times. Error or accuracy refers to the difference between the expected (correct) value and the measured value. Error or accuracy is a qualitative attribute that can only be said to be in good agreement with expected results. Associating a quantitative value to the accuracy of the measurement assumes that the correct value is known precisely, but this is seldom the case.

### 5.6.1 Measurement uncertainty

A quotation from [54] best describes uncertainty and its necessity: "the result of a measurement is only an approximation or estimate of the value of the specific quantity subject to measurement, that is, the measurand, and thus the result is complete only when accompanied by a quantitative statement of its uncertainty."

Measurement uncertainty is divided in two categories according to the method used to derive the uncertainty. The two categories are:

- Type A - Evaluated through statistical methods
- Type B - Evaluated through any other means

Type A evaluation is done by repeating the measurement enough times to estimate the uncertainty associated with the measurement. Type B evaluation uses any other information such as the accuracy of the calibration standards, experience from previous measurements or manufacturer specifications. The measurement repeatability of the SMA probe is the greatest restriction, since the residual source mismatch is of the same order of magnitude as the errors in calibration. This information is used to estimate measurement uncertainty and then related to the extracted permittivity uncertainty.

### 5.6.2 Measurement error due to incorrect calibration

As discussed in section 5.1, measurement errors are divided into raw and residual errors. Residual errors include systematic, random and drift errors. In all the calculations that follow, drift and random errors are going to be assumed small compared to residual errors. This is a valid assumption since careful climate control and enough averaging can minimise these error contributions.

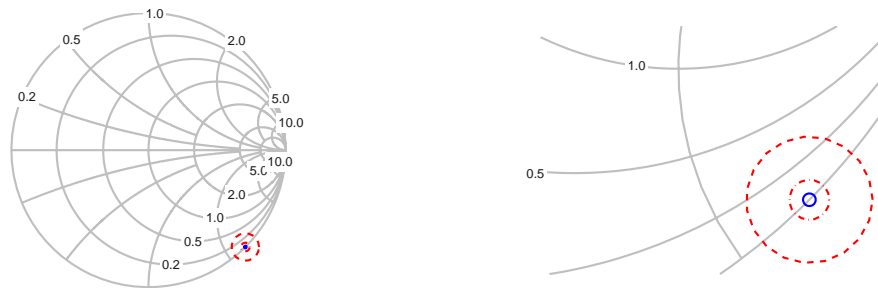
Measurement uncertainty is discussed in two parts. Magnitude uncertainty is discussed first and then phase uncertainty is presented. Reflection uncertainty is defined as a combination of systematic, random and drift errors[55].

$$E_{rm} = \text{systematic} + \sqrt{(\text{random})^2 + (\text{drift})^2} \quad (5.6.1)$$

The first and significant second order error terms that contribute to systematic errors are shown in (5.6.2). After calibration the systematic errors are residual errors as indicated by the subscript "r". The last term in (5.6.2) represents the dynamic accuracy of the VNA.

$$\text{systematic} = e_r = e_{00r} + e_{10r}e_{01r}\Gamma + e_{11r}\Gamma^2 + \Gamma D \quad (5.6.2)$$

The magnitude of the reflection from a coaxial probe is close to unity when low and medium loss samples are measured. The total residual error can then be approximated by a circle of uncertainty that does not change as long as the reflection magnitude is large. Figures 5.23(a) and 5.23(b) show a Smith-chart with -20 dB, -30 dB and -40 dB uncertainty circles. These circles indicate that a measurement at the centre of the circle could in actual fact be from an impedance within or on the circle.



(a) Uncertainty on the Smith-chart.

(b) Enlarged Smith-chart.

Figure 5.23: Circle of uncertainty for uncertainty of -20dB, -30dB and -40dB.

**Magnitude error**

The maximum and minimum reflection magnitudes occur when the uncertainty,  $U$ , is added in phase and out of phase with the measurement. This occurs on the edge of the uncertainty circle unless the circle includes the zero reflection point. Figure 5.24 illustrates how the maximum and minimum reflection magnitude can be calculated. The equations for  $\Gamma_{max}$  and  $\Gamma_{min}$  are given by (5.6.3) and (5.6.4).

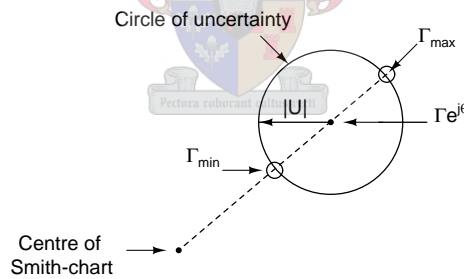


Figure 5.24: Diagram illustrating how the magnitude uncertainty is calculated.

$$\Gamma_{max} = |\Gamma| + |U| \tag{5.6.3}$$

$$\Gamma_{min} = |\Gamma| - |U| \quad : \quad |\Gamma| > |U| \tag{5.6.4}$$

$$= 0 \quad : \quad |\Gamma| \leq |U|$$

**Phase error**

The maximum and minimum phase can also be calculated through simple trigonometric identities. Figure 5.25 illustrates how the maximum and minimum phase is calculated. The equations for the maximum and minimum phases are given by (5.6.5) and (5.6.6) respectively.

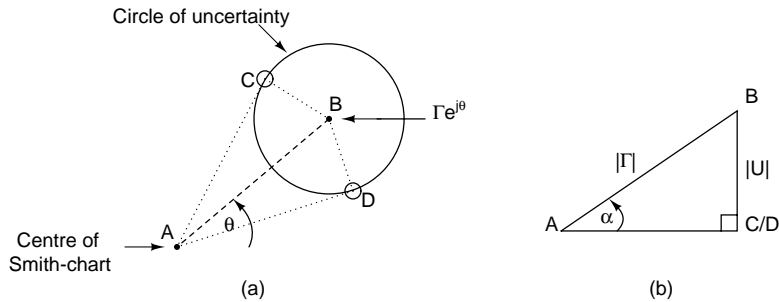


**Figure 5.25:** Diagram illustrating how the phase uncertainty is calculated.

$$\begin{aligned} \theta_{max} &= \theta + \arcsin\left(\frac{|U|}{|\Gamma|}\right) & : |\Gamma| > |U| & \quad (5.6.5) \\ &= \theta + \pi & : |\Gamma| \leq |U| & \end{aligned}$$

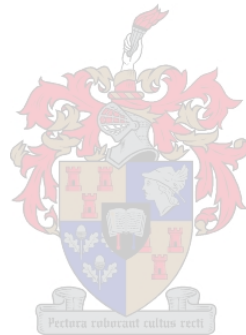
$$\begin{aligned} \theta_{min} &= \theta - \arcsin\left(\frac{|U|}{|\Gamma|}\right) & : |\Gamma| > |U| & \quad (5.6.6) \\ &= \theta - \pi & : |\Gamma| \leq |U| & \end{aligned}$$

**5.7 Conclusion**

Two possible calibration procedures were presented that can perform accurate calibrations on the open-ended coaxial probe. The first is the two-tier SOL calibration and secondly the TRL calibration. On-line calibration has been proven to be inadequate unless a high quality matched termination can be fabricated or emulated using a sliding load. The two-tier SOL calibration is fast, easy and the standards are not sensitive to environmental changes. TRL calibration is a two-port calibration and requires more time and care to perform accurately. A combination of these two calibration procedures should be used to benefit from both the accuracy of the TRL calibration and also the calibration ease of the SOL calibration. This is done by measuring the SOL standards after a TRL calibration and then using the SOL calibration for subsequent measurements.

The combination of TRL and SOL calibrations also allows the quality of the calibration to be checked and the residual errors in the system determined. The residual errors in measurement is then used to determine the possible errors in the extracted permittivity.

The TRL calibration has been proven to be a great calibration method for the coaxial probe, but there is room for improvement. Multiple TRL LINE standards should be used to improve calibration accuracy and extend the calibration range beyond the 8:1 frequency limit so that measurement at lower frequencies can also be performed.



## Chapter 6

# Measurement

The components of a permittivity measurement system has been presented and used to design the probes. This chapter evaluates the probes by measuring known materials.

Measurements are not complete unless they are accompanied by an associated uncertainty, but the uncertainty can only be estimated for the SMA-probe because the combination of TRL and SOL standards allow the errors in the calibration to be determined. A statistical uncertainty analysis could be used for this and the other probes, but time restrictions prohibited sufficient measurements for this kind of analysis.

Section 6.1 presents the materials that have been measured with the probes. Each of the probes is then used to measure the permittivity of the samples in sections 6.2 to 6.5. It is important to remember that only the SMA-probe has been accurately calibrated. Although great effort has been made to calibrate the other probes using a reference material, the results are not expected to be as accurate as the SMA-probe.

### 6.1 Measured Samples

Six sample materials have been chosen to test the operation of the probes. These samples cover a wide permittivity range. Four of the samples are solids and the other two are liquids. The combination of these samples allows many aspects of the probes to be tested and compared. All measurements were performed at 22 °C. The samples were stored in the Metrology lab with the air conditioning on for more than a day before measurement to ensure that the samples are at the same temperature as the probes. The VNA was switched on for more than two hours before measurement started. This ensures that the components of the VNA have reached their steady-state temperatures and system drift is expected to be minimal.



The solid samples are presented first, followed by the liquid samples.

### 6.1.1 Solids

The permittivities of the solid samples are listed in Table 6.1. All the samples have been machined flat, but they were not polished. It is doubtful that a HF laboratory would polish the sample for routine measurements. The samples are thus a good representation of what a HF laboratory would attempt to measure.

**Table 6.1:** Permittivity of solid samples quoted in literature

Sample	Frequency	Temp.[°C]	$\epsilon'_r$	$\epsilon''_r$	Source
PTFE	3 GHz	22	2.1	0.000315	Von Hippel[10]
	10 GHz	22	2.08	0.00077	Von Hippel[10]
PVC	3 GHz	20	2.84	0.0156	Von Hippel[10]
Polyester	3 GHz	25	2.85	0.0285	Von Hippel[10]
	10 GHz	25	2.85	0.0228	Von Hippel[10]
	3 GHz	-	2.817	0.0243	Fouché[56]
PVDF	1 MHz	25	6	0.99	Symalit[57]
	10 MHz	-	5	1.125	Rütschlin[21]
	25 MHz	-	4	0.88	Rütschlin[21]

#### Polytetrafluoroethylene

Polytetrafluoroethylene (PTFE) is a well known material with a relative dielectric constant close to 2.1. It has low loss at microwave frequencies and is often used in coaxial transmission lines to supply mechanical support. The sample used during the measurement has been supplied by Cape Plastics.

#### Polyvinyl chloride

Polyvinyl chloride (PVC) is well established as a dielectric. It is often combined with other plastics for improved mechanical or electrical properties[10]. The sample used during the measurement was also supplied by Cape Plastics.

#### Polyester

The polyester sample is clear and brittle at room temperature. It is available from any hardware store. A catalyst is mixed with the polyester and left for a few hours to harden. The brittleness at room temperature made machining difficult. The sample was sanded

to ensure a flat, smooth surface. This sample has been chosen because it has previously been measured using a rectangular waveguide in the 3 GHz range at the University of Stellenbosch[56]. This allows direct comparison of measurements with the coaxial probe and another technique using the same sample.

### Polyvinylidene Fluoride

Polyvinylidene Fluoride (PVDF) is a cream coloured, high loss solid. It has previously been measured at the University of Stellenbosch in the frequency range 1 MHz to 25 MHz. This frequency range is much lower than the measurements in this thesis, but the information does give an indication of the material properties. The sample has been manufactured by Symalit[57].

### 6.1.2 Liquids

The liquid samples and their associated Cole-Cole model parameters are listed in Table 6.2. The Cole-Cole model is repeated here for easy reference.

$$\epsilon^* = \epsilon_\infty + \frac{\epsilon_s - \epsilon_\infty}{1 + (j\frac{f}{f_r})^{1-\alpha}} \quad (6.1.1)$$

Most of the references used a Debye model to describe the materials, but as mentioned in chapter 2 the Cole-Cole model is equivalent to the Debye model when  $\alpha = 0$ .

**Table 6.2:** Permittivity of liquid samples quoted in literature

Sample	Temp.[°C]	$\epsilon_s$	$\epsilon_\infty$	$f_r$	$\alpha$	Source
Methyl alcohol	25	33.7	4.4	3.22 GHz	0.0036	Grant[1]
	20	33.64	5.7	3 GHz	0	Belhadj-Tahar[2]
	20	34.8	4.5	2.8 GHz	0	Jordan[3]
Water	15	82.033	6.604	14.455 GHz	0	Ellison[58]
	20	80.181	6.507	16.527 GHz	0	Ellison[58]
	25	78.404	6.640	18.835 GHz	0	Ellison[58]

### Methyl alcohol

Methyl alcohol or methanol is a interesting sample because it has a relaxation frequency in the middle of the measured frequency range. This provides a great variety of permittivity and loss factor values and allows the data to be graphically presented on an Argand diagram.

The sample has been obtained from the Chemical Engineering department. The glass containers were cleaned three times with the methanol before filling the containers. Although every effort has been made to eliminate any contamination of the methanol, the quality and purity of the original sample is unknown.

### Water

Distilled water was also supplied by the Chemical Engineering department. The same procedure has been followed to minimise contamination of the sample as was done for the methanol. The water was stored in a plastic container for a long period at the Chemical Engineering department and thus its purity is unknown. Deionised water from the Electrical and Electronic department has also been measured on an earlier occasion. The extracted permittivity of the deionised water was identical to the measurement presented here.

## 6.2 SMA-Probe

The response of the LOAD standard used for the two-tier SOL calibration was measured after a careful TRL calibration from 1 GHz to 8 GHz. The load response is shown in Figure 5.11(a). The response was then extrapolated below 1 GHz to allow measurement at these frequencies. The accuracy of the extrapolation is questionable, but the measured results indicate that the extrapolation was successful. This extrapolation can be avoided by using multiple LINE standards during the TRL calibration to increase the calibrated frequency range.

Measurements are presented displaying the relative dielectric constant ( $\epsilon'_r = \kappa'$ ) and the relative loss term ( $\epsilon''_r = \kappa''$ ). The loss factor,  $\tan \delta$ , was not used since it is a function of  $\epsilon'_r$ . Errors in  $\epsilon'_r$  would then also be displayed in the loss term.

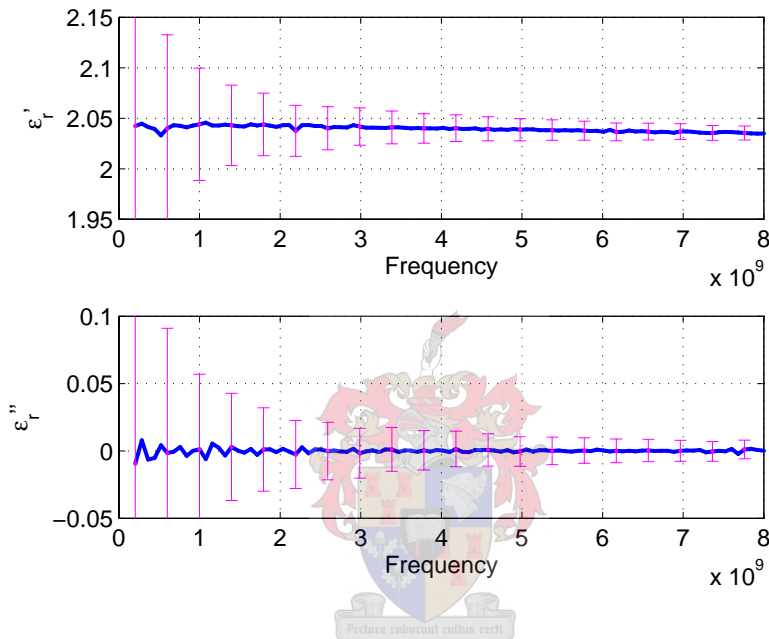
All measurements performed on the SMA-probe are presented with a measurement uncertainty of -50 dB. This measurement uncertainty is the maximum expected uncertainty due to measurement repeatability and residual systematic errors.

### 6.2.1 Solids

The SMA-probe was first calibrated with the probe facing upward to measure the solid samples. A summary of the SMA measurements is listed in Table 6.3. These measurements are in excellent agreement with the expected values listed in Table 6.1. The extracted permittivity for measurements are shown in Figures 6.2.1 to 6.2.1. The extracted

**Table 6.3:** Measured average permittivity of solid samples (SMA-probe).

Sample	Temp.[°C]	$\epsilon'_r$	$\epsilon''_r$
PTFE	22	2.04	$\approx 0$
PVC	22	2.78	0.019
Polyester	22	2.83	0.032
PVDF	22	2.9 - 2.6	0.29 - 0.09

**Figure 6.1:** Measured permittivity of PTFE using the SMA-probe.

real permittivity is within 3% from the expected results. This difference can be attributed to a combination of lift-off and manufacturer tolerances. The PVDF sample can not be compared to expected results, but the permittivity is expected to drop from 25 MHz to 200 MHz and even further as the frequency increases. Once the loss term has reached a steady state, the permittivity should also remain constant. This characteristic is clearly seen in Figure 6.2.1.

## 6.2.2 Liquids

After completion of the solid measurements, the probe was disconnected from the VNA and reconnected facing down in order to measure liquid samples. The probe was then recalibrated and the first liquid sample was measured. The probe was carefully cleaned

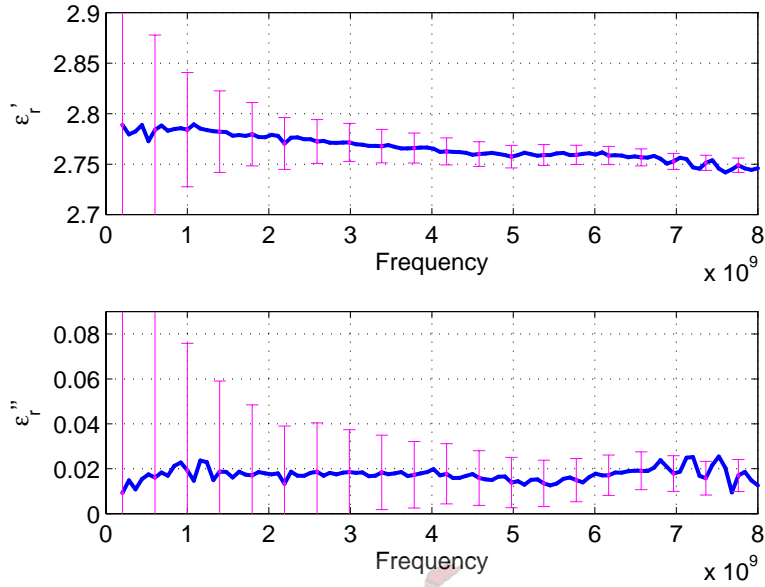


Figure 6.2: Measured permittivity of PVC using the SMA-probe.

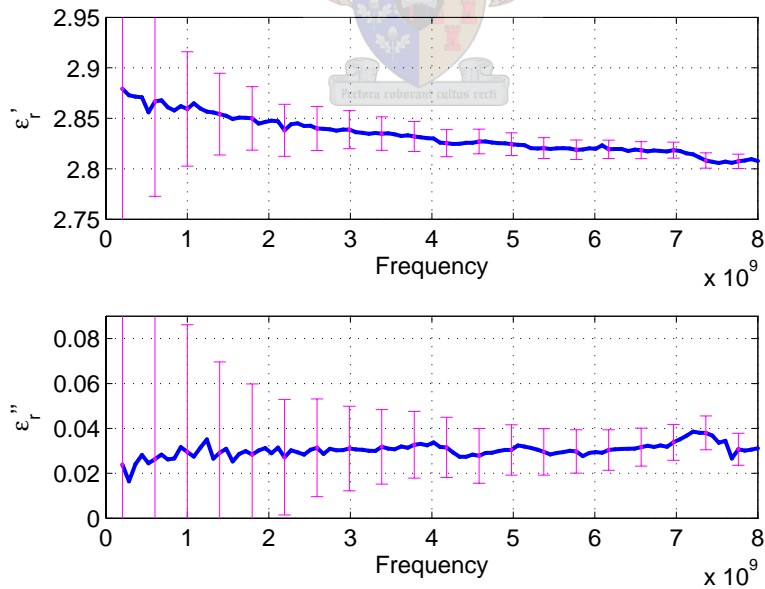
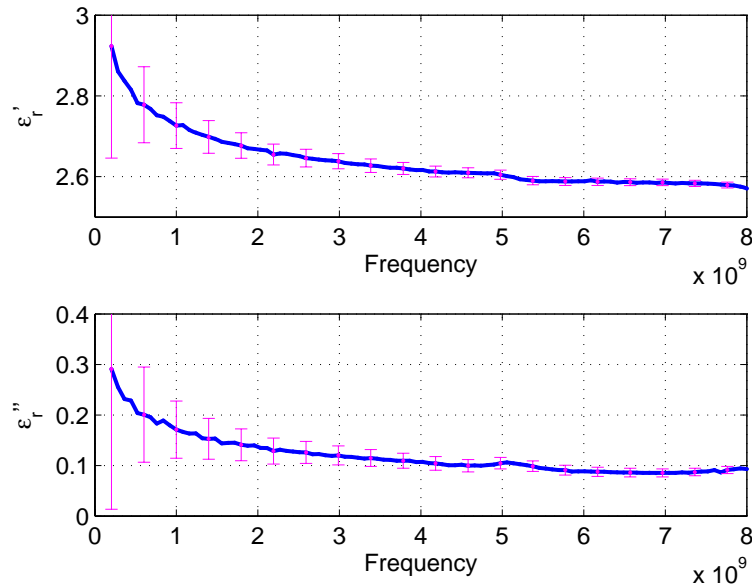


Figure 6.3: Measured permittivity of Polyester using the SMA-probe.



**Figure 6.4:** Measured permittivity of PVDF using the SMA-probe.

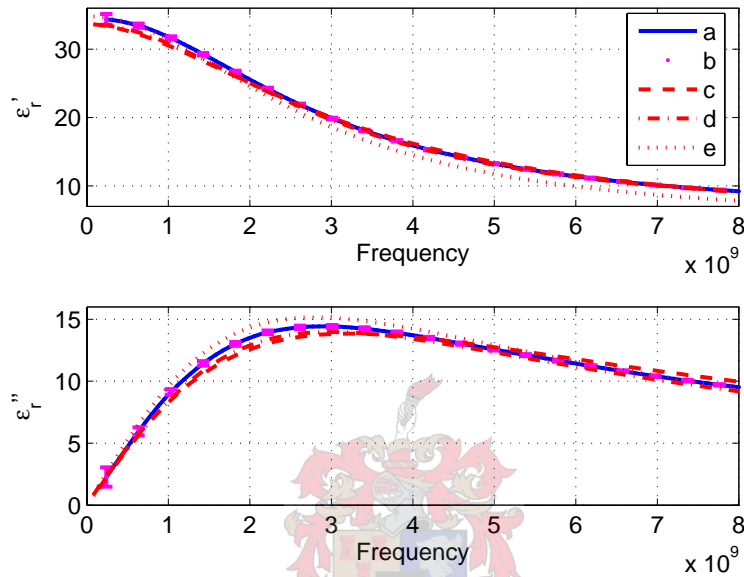
and given time to reach a steady state temperature before recalibrating and measuring the second sample.

Due to radiation the measurements are only valid over a limited frequency range, but this frequency range can be extended for high loss samples. This topic was not mentioned during the solid measurements because none of the solid samples have a dielectric constant above 3.5 and thus the measurements are valid up to 8 GHz. The liquid samples have permittivities far above 3.5 and thus the frequency range is reduced. The extracted permittivities are shown in Figures 6.2.2 and 6.2.2 over the entire frequency range to illustrate where the radiation becomes a significant problem. Table 6.4 summarises the measurements. The Debye model of water was only fitted over the valid frequency range. The high frequency permittivity,  $\epsilon_\infty$ , and the relaxation frequency,  $f_r$ , was not part of the least squares fit because an infinite number of combinations exist that fit the data. They were chosen close to the literature values and then the static permittivity,  $\epsilon_s$ , was fitted to the measured data.

The valid frequency range for the methanol is from 44 MHz to 4 GHz. The frequency range is calculated using equations (4.2.2) and (4.2.3). It is clear from the measurements the loss in methanol is high enough to allow measurement over the entire frequency range since the extracted permittivity is within the bounds of previously measured val-

**Table 6.4:** Measured Debye model parameters of liquid samples (SMA-probe).

Sample	Temp.[°C]	$\epsilon_s$	$\epsilon_\infty$	$f_r$	$\alpha$
Methyl alcohol	22	34.72	5.79	2.935 GHz	0
Water	22	82.34	6.5	17.0 GHz	0

**Figure 6.5:** Measured permittivity of Methyl alcohol using the SMA-probe. (a) Measured, (b) Uncertainty, (c) Grant[1], (d) Belhadj-Tahar[2], (e) Jordan[3].

ues for methanol. The Debye model in Table 6.4 was fitted over the entire frequency range. Figure 6.2.2 is an Argand diagram of the measured and quoted permittivity of methanol.

The valid frequency range of water is from 20 MHz to 1.7 GHz. The measured results in Figure 6.2.2 indicate that frequency range can be extended to 4 GHz. The extracted permittivity decreases fast above 4 GHz and this is probably due to the interference by the radiated energy. Figure 6.2.2 shows the measurements up to 3 GHz. These measurements are in good agreement and differ by less than 3% from expected results at 20 °C.

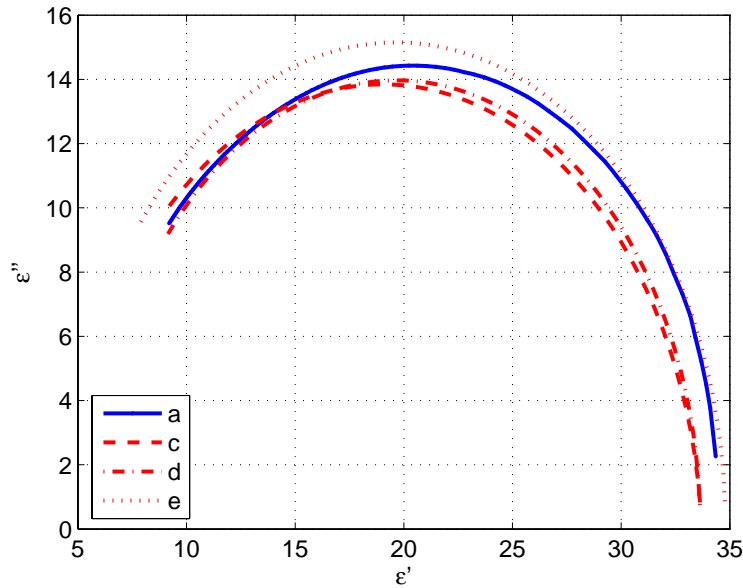


**Figure 6.6:** Argand diagram of the measured permittivity of Methyl alcohol using the SMA-probe. (a) Measured, (b) Uncertainty, (c) Grant[1], (d) Belhadj-Tahar[2], (e) Jordan[3].

### 6.3 N-Probe

The N-probe does not have a TRL calibration set to perform an accurate calibration. The LOAD standard has to be assumed perfect or calibration can be performed with some of the sample materials. Calibration with the assumption of a perfect load resulted in poor agreement with the expected values, especially for low permittivity and low loss samples. Two of the samples namely methanol and PTFE were used to estimate a response for the LOAD standard. The reflection from the load standard was determined from both standards and then an average value was used. This calibration is not expected to be accurate, but shows the type of errors caused by incorrect calibration. It is stressed that the measurements in this and the following sections be viewed qualitatively and that the measurements are not accurate.

#### 6.3.1 Solids

The same measurement procedure was followed for the N-probe measurements as was done for the SMA-probe. Table 6.5 lists the average extracted permittivity over the valid frequency ranges. Unlike the SMA-probe the N-probe measurements of the solids are



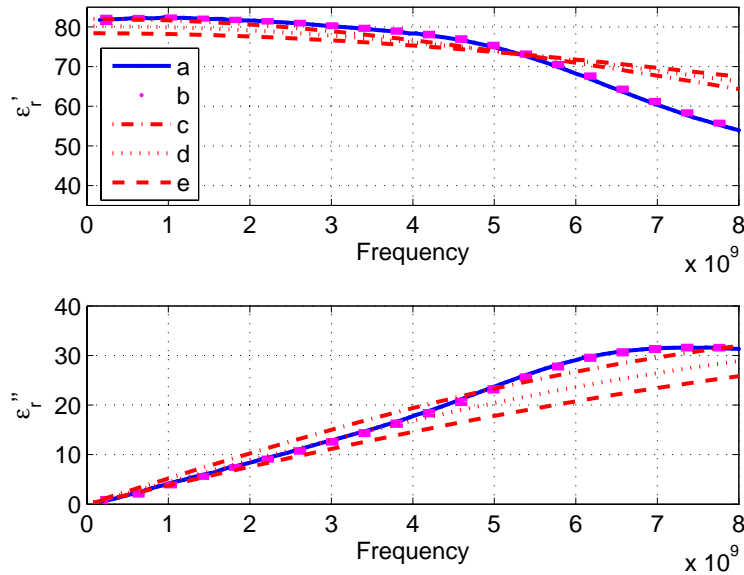


**Figure 6.7:** Measured permittivity of water over from 100 MHz to 8 GHz using the SMA-probe. (a) Measured, (b) Uncertainty bars, (c) Cole-Cole model form literature at 15 °C, (d) 20 °C, (e) 25 °C.

not valid over the entire measured frequency range. Inadequate calibration accuracy seems to be the greater limitation than the radiation of the probe. At frequencies above 3 GHz the measurements show deviations from the expected results due to incorrect cancellation of reflections in the measurement setup.

The permittivity of the solid samples differ by less than 7% with the literature. The greatest difference is seen with permittivity of polyester. The PTFE and PVC samples differ by less than 1% from measurements with the SMA-probe. This can be misleading since the PTFE sample played an important role during the calibration. It is thus expected that the measured PTFE be close to the SMA-probe measurements.

### 6.3.2 Liquids

The valid frequency range for methanol using the N-probe is from 20 MHz to about 1.2 GHz. The measurements seem to be valid over the entire frequency range due to the high loss factor of the methanol sample. The measurements are in good agreement with the expected results, but it should be pointed out that the methanol played an important part in the calibration of the probe.

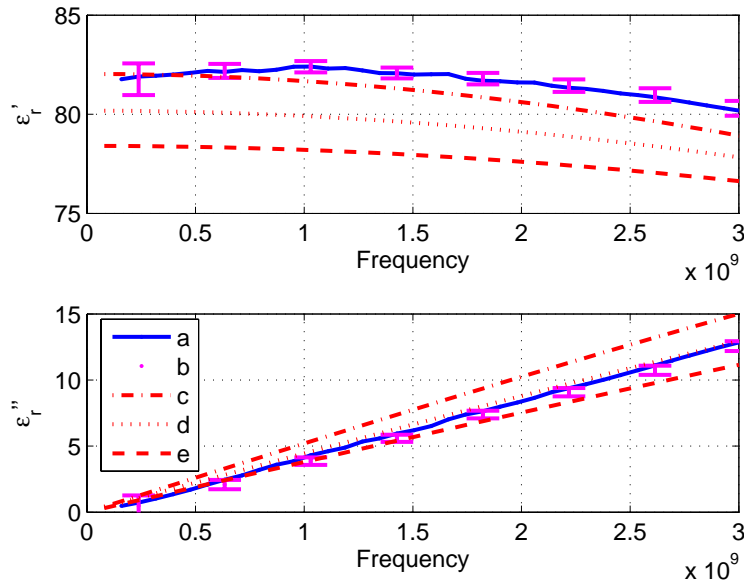


**Figure 6.8:** Measured permittivity of water form 100 MHz to 3 GHz using the SMA-probe. (a) Measured, (b) Uncertainty bars, (c) Cole-Cole model form literature at 15 °C, (d) 20 °C, (e) 25 °C.

**Table 6.5:** Measured average permittivity of solid samples (N-probe).

Sample	Temp.[°C]	$\epsilon'_r$	$\epsilon''_r$
PTFE	22	2.05	$\approx 0$
PVC	22	2.76	0.019
Polyester	22	2.98	0.03
PVDF	22	3 - 2.7	0.34 - 0.11

The water measurement shows an interesting and unexpected ripple starting at 500 MHz and ending close to 2.5 GHz. The valid frequency range for the probe in water is from 10 MHz to 670 MHz. This means that the ripple starts even before radiation is significant. Figure 6.3.2 shows the measurement up to 3 GHz. Here it is clearly seen that the ripple is superimposed on the correct results.

Otto[39] also had similar ripples in his data above 500 MHz. He attributed it to a finite sample size and the high polarisation characteristic of water. If this is the correct reason the ripple should be present in the measurements using the SMA-probe as well, but this it is not the case. Incorrect calibration is probably the cause of the ripple in these measurements.

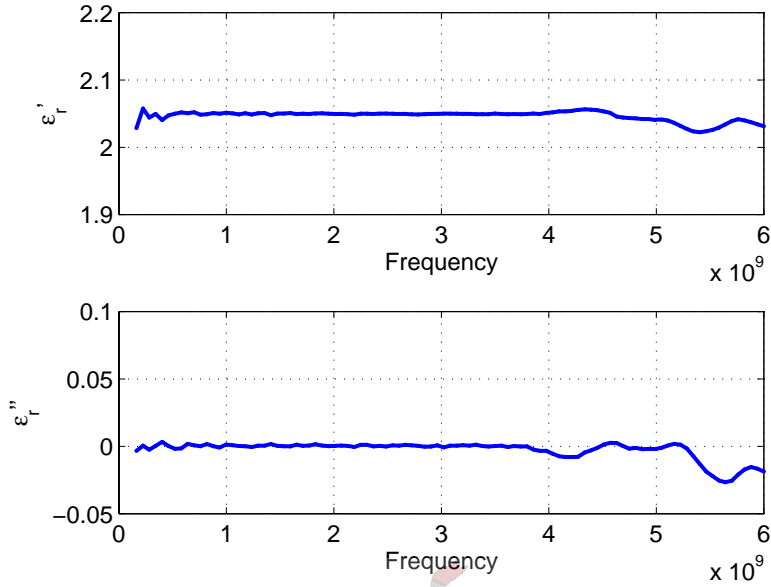


Figure 6.9: Measured permittivity of PTFE using the N-probe

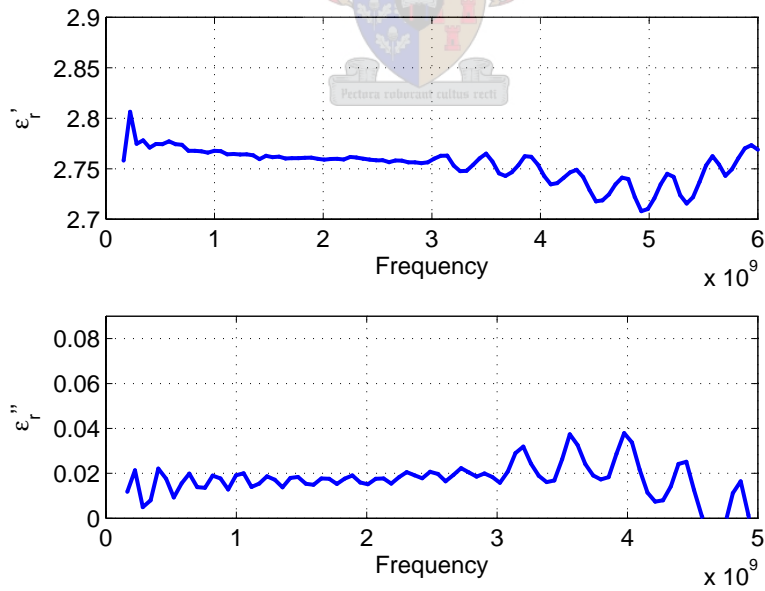


Figure 6.10: Measured permittivity of PVC using the N-probe

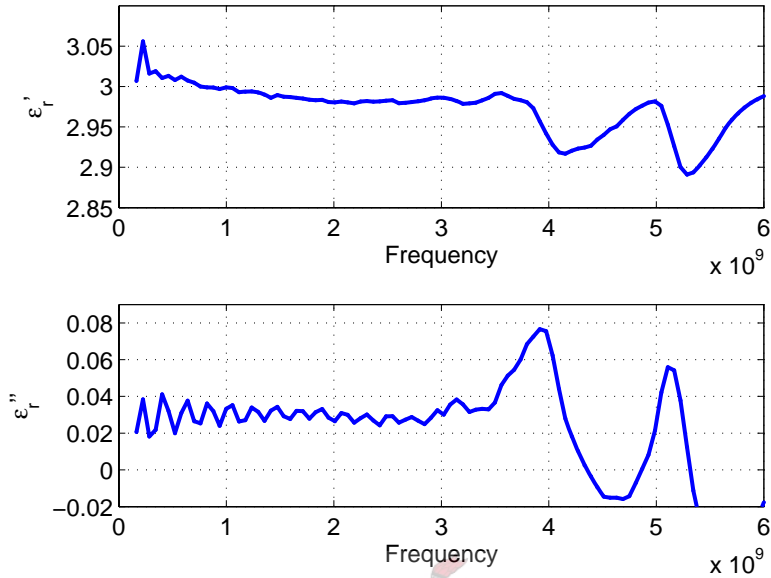


Figure 6.11: Measured permittivity of Polyester using the N-probe

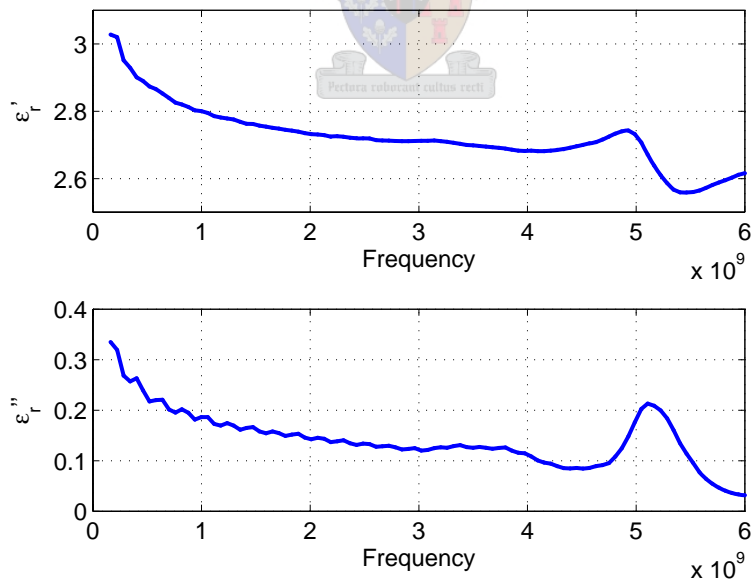
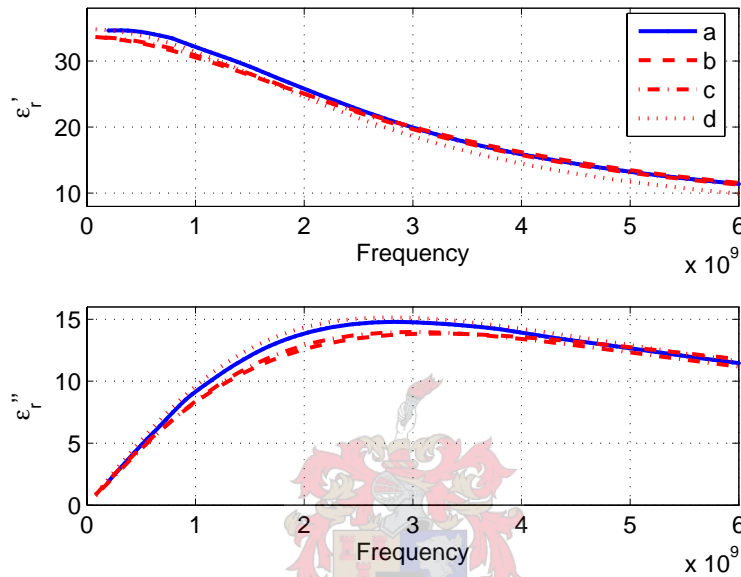


Figure 6.12: Measured permittivity of PVDF using the N-probe

**Table 6.6:** Measured Debye model parameters of liquid samples (N-probe).

Sample	Temp.[°C]	$\epsilon_s$	$\epsilon_\infty$	$f_r$	$\alpha$
Methyl alcohol	22	35.28	5.884	2.88 GHz	0
Water	22	84.13	6.5	17.0 GHz	0

**Figure 6.13:** Measured permittivity of Methyl alcohol using the N-probe. (a) Measured, (b) Grant[1], (c) Belhadj-Tahar[2], (d) Jordan[3].

## 6.4 7/16-Probe

The 7/16-probe has the same problem as the N-probe. A TRL calibration set has not been developed and the response of the LOAD standard is not known accurately. The problem is worsened by the fact that the LOAD standard for the N-probe is used to calibrate the 7/16-probe. The dimension mismatch causes more reflections that make the probe less ideal. The PTFE sample was used to calibrate the probe and thus it is not displayed in any of the N-probe measurements.

### 6.4.1 Solids

The extracted permittivity of the solid samples are shown in Figures 6.17, 6.4.1 and 6.4.1. The limited calibration was good enough to measure the dielectric constants of the samples to within 10% of the literature values.

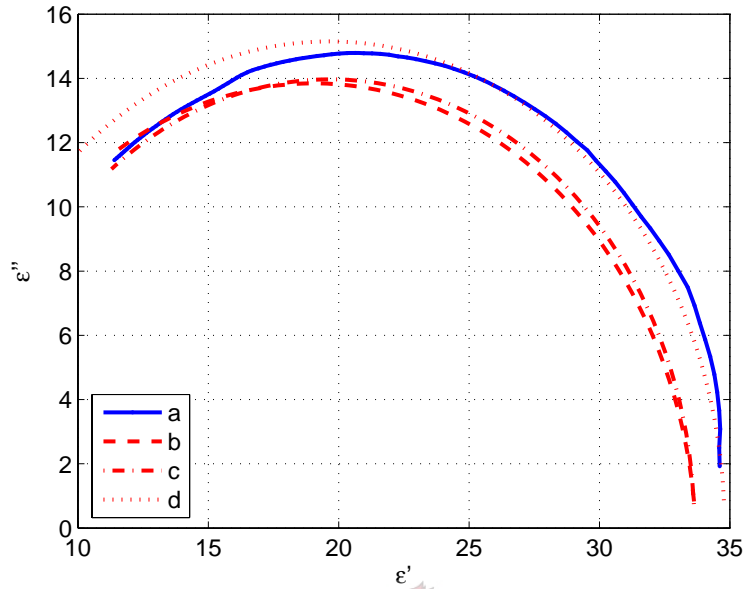


**Figure 6.14:** Argand diagram of the measured permittivity of Methyl alcohol using the N-probe. (a) Measured, (b) Grant[1], (c) Belhadj-Tahar[2], (d) Jordan[3].

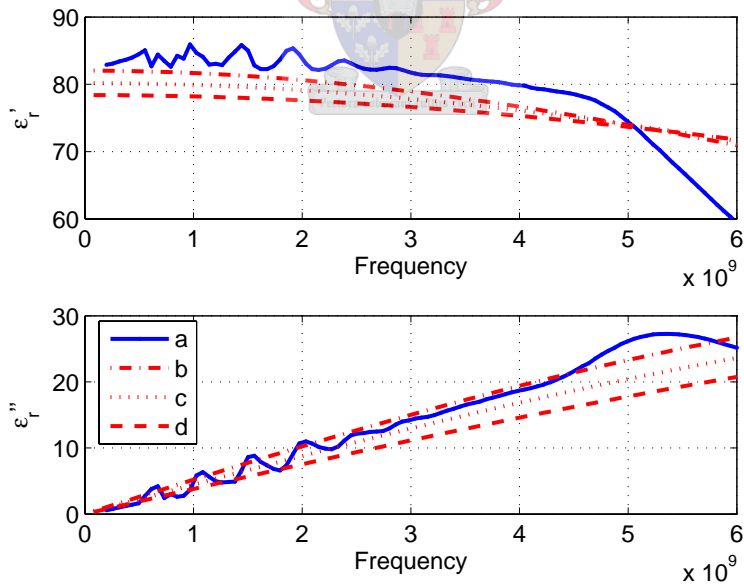


**Figure 6.15:** Measured permittivity of water from 100 MHz to 6 GHz using the N-probe. (a) Measured, (b) Cole-Cole model form literature at 15 °C, (c) 20 °C, (d) 25 °C.

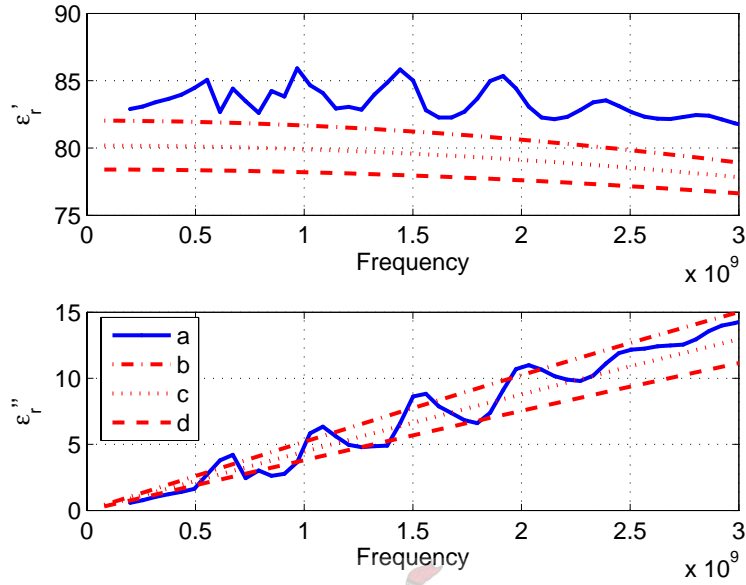


**Figure 6.16:** Measured permittivity of water from 100 MHz to 3 GHz using the N-probe. (a) Measured, (b) Cole-Cole model form literature at 15 °C, (c) 20 °C, (d) 25 °C.

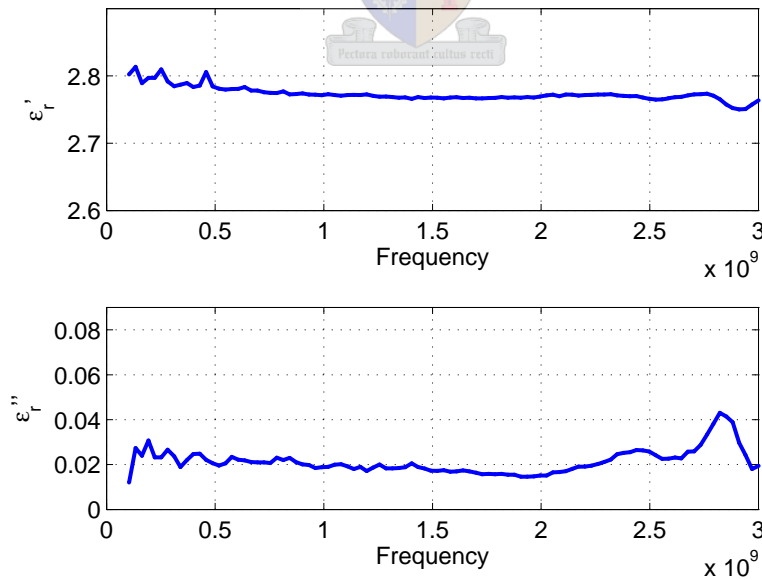


**Figure 6.17:** Measured permittivity of PVC using the 716 probe

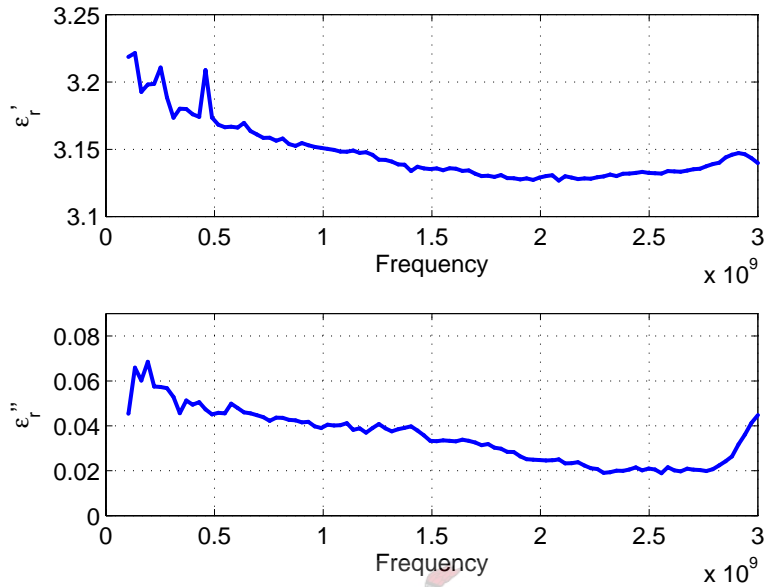


Figure 6.18: Measured permittivity of Polyester using the 716 probe.

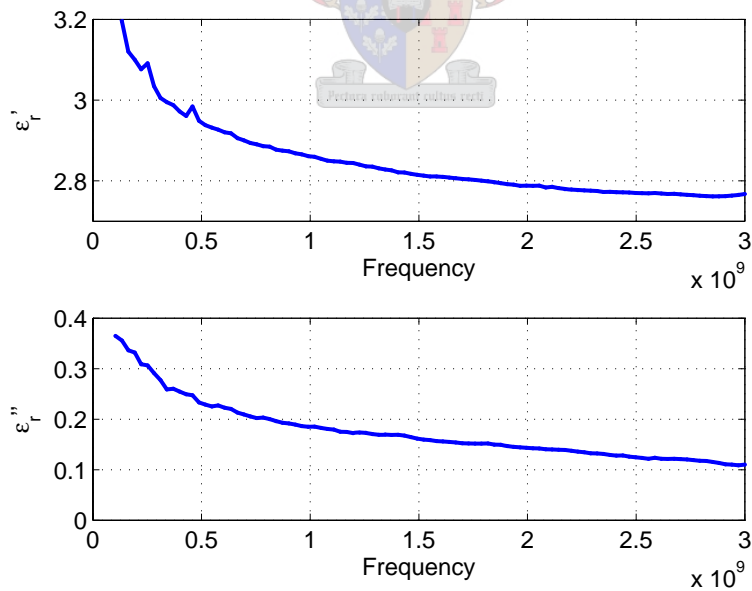
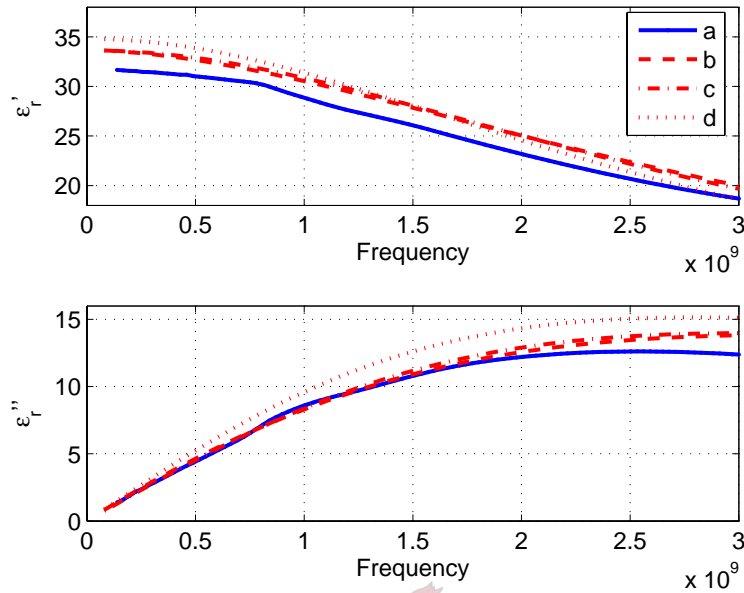


Figure 6.19: Measured permittivity of PVDF using the 716 probe.





**Figure 6.20:** Measured permittivity of Methyl alcohol using the 7/16-probe. (a) Measured, (b) Grant[1], (c) Belhadj-Tahar[2], (d) Jordan[3].

## 6.4.2 Liquids

The methanol measurement shows reasonable agreement up to 1.5 GHz even though the upper frequency limit for the probe with a sample dielectric constant close to 30 being only 550 MHz.

The water measurement is only valid up to 340 MHz. In the valid frequency range the extracted permittivity is 7.5% less than the expected permittivity. The ripple seen in the N-probe measurements of water is also seen in the 7/16-probe measurements.

## 6.5 7/16-Probe with extended centre pin

Due to the inaccurate calibration of the 7/16-probe it was decided not to drill holes in the solid samples. The permittivity of air, methanol and water was measured assuming a perfect LOAD standard. The permittivity of air is expected to be close to one with no measurable loss. Figure 6.24 shows the measured permittivity of air.

The highest valid frequency for the 7/16 probe with extended centre pin in methanol is 300 MHz. The measurements seem reasonable up 500 MHz, but at higher frequencies the measured loss increases rapidly.

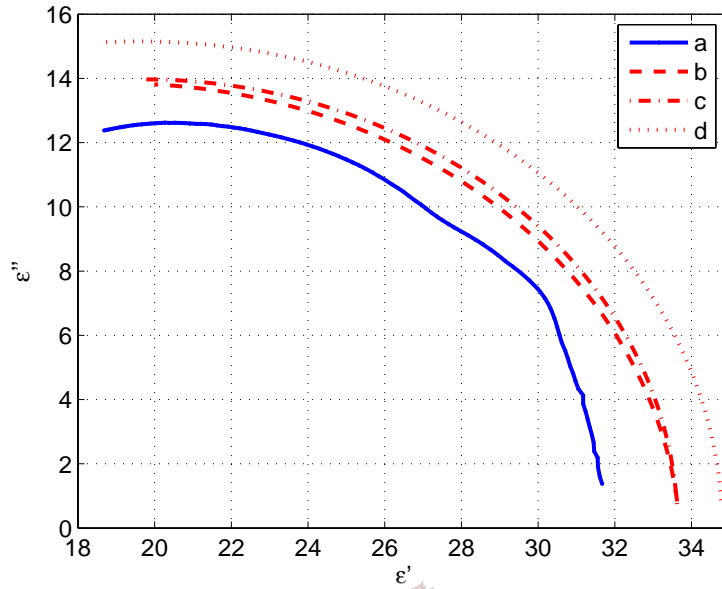


**Figure 6.21:** Argand diagram of the measured permittivity of Methyl alcohol using the 7/16-probe. (a) Measured, (b) Grant[1], (c) Belhadj-Tahar[2], (d) Jordan[3].

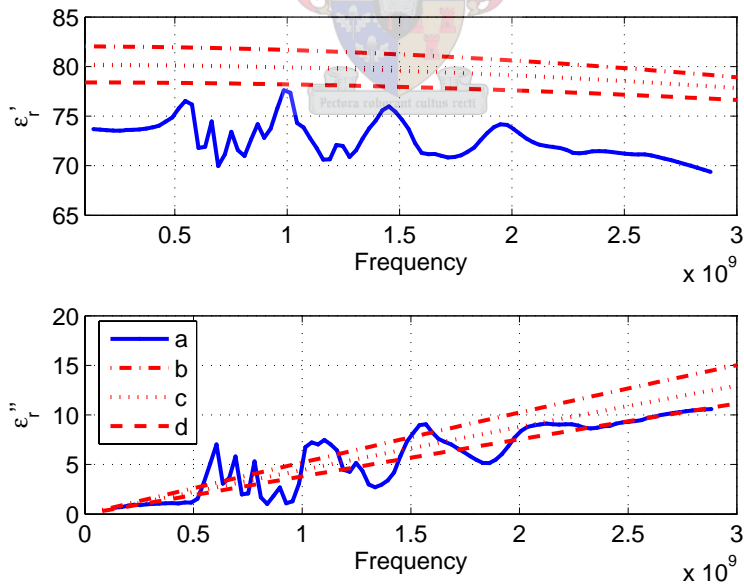


**Figure 6.22:** Measured permittivity of water from 130 MHz to 3 GHz using the 7/16-probe. (a) Measured, (b) Cole-Cole model form literature at 15 °C, (c) 20 °C, (d) 25 °C.

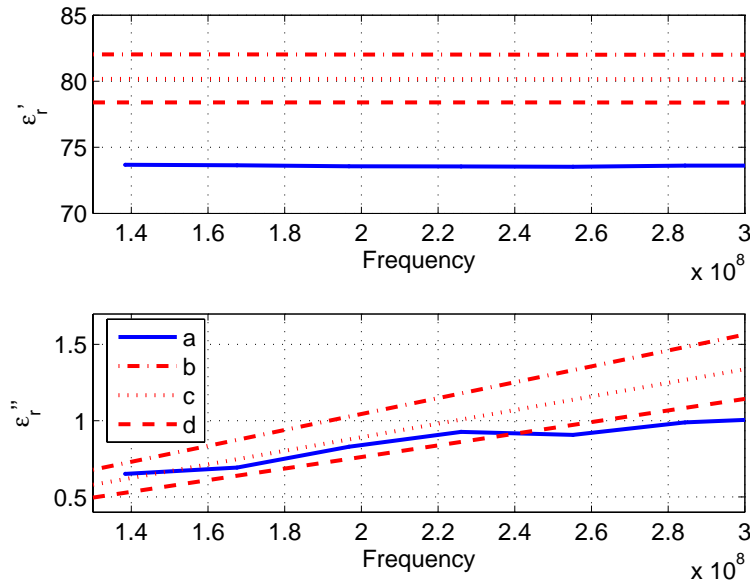


**Figure 6.23:** Measured permittivity of water from 130 MHz to 300 MHz using the 7/16-probe. (a) Measured, (b) Cole-Cole model form literature at 15 °C, (c) 20 °C, (d) 25 °C.

Water measurements are shown in Figures 6.5 and 6.5. The maximum valid frequency for the probe in water 170 MHz. The real permittivity measurements are 5% less than the expected results. The loss measurement is inaccurate as can be expected for this limited calibration.

## 6.6 Conclusion

The measurements have shown that the coaxial probe can measure permittivity over extremely wide frequency and sample ranges, but requires accurate calibration. The TRL calibration has proven to be a great method to determine an accurate response for the calibration standards. The measured response is then later used together with the two-tier SOL calibration to improve calibration speed and ease.

The inability to calibrate the larger probes accurately deters from the excellent measurement abilities of these probes. The accuracy of the larger probes were seen to be much lower, but were still able to determine the dielectric constant to within 10%. It was also illustrated that calibrating with a material similar to the one being measured improves the accuracy of the extracted permittivity. Care should be taken not to mistake this for

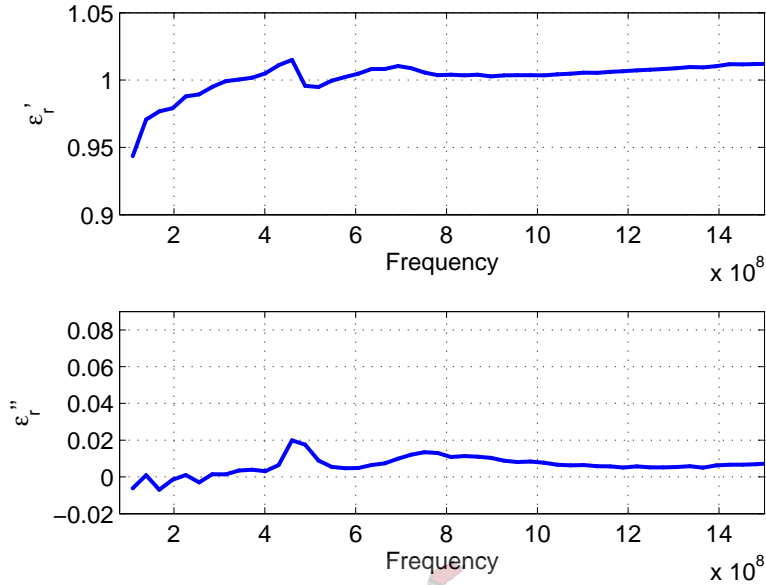


Figure 6.24: Measured permittivity of air using the 7/16 probe with extended centre pin.

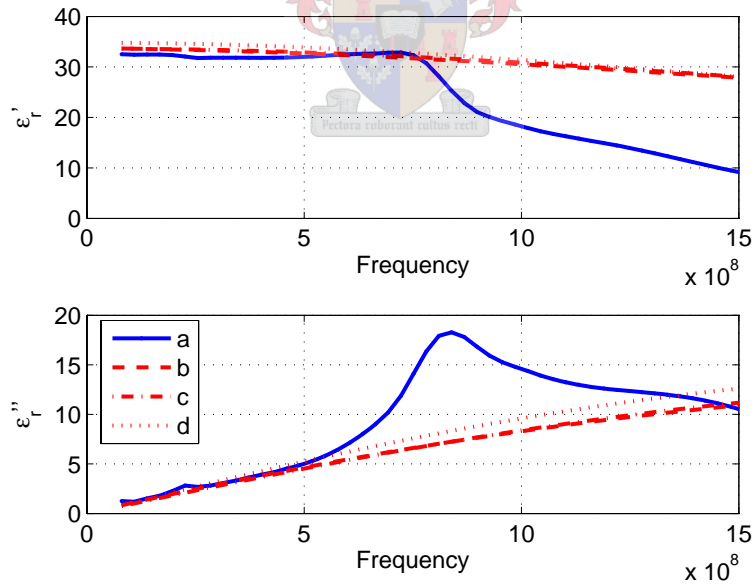
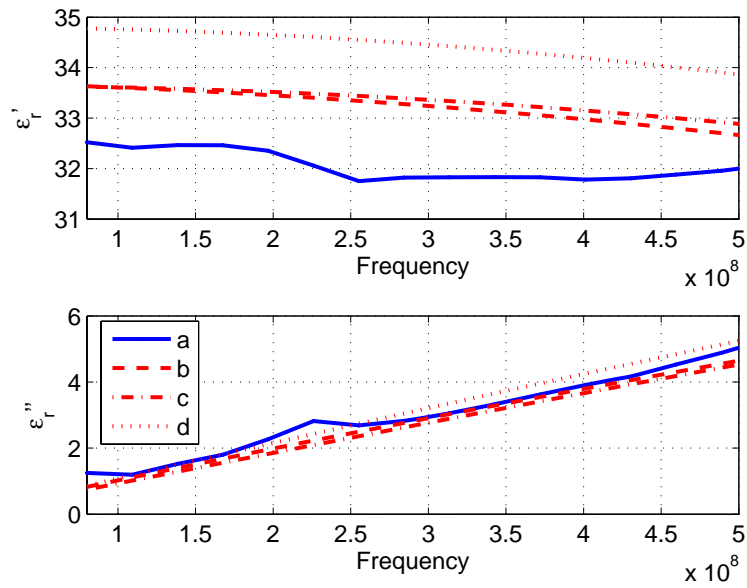
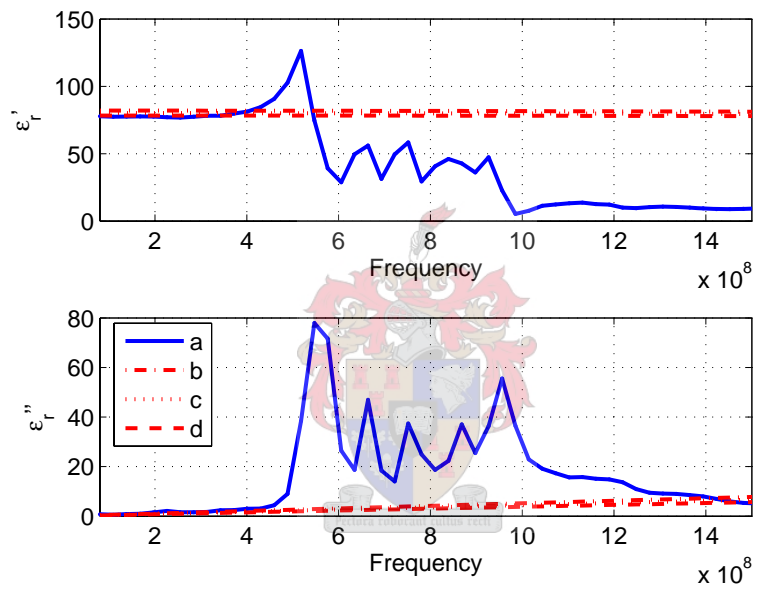


Figure 6.25: Measured permittivity of Methyl alcohol from 100 MHz to 1.5 GHz using the 7/16-probe with extended centre pin. (a) Measured, (b) Grant[1], (c) Belhadj-Tahar[2], (d) Jordan[3].



**Figure 6.26:** Measured permittivity of Methyl alcohol from 100 MHz to 500 MHz using the 7/16-probe with extended centre pin. (a) Measured, (b) Grant[1], (c) Belhadj-Tahar[2], (d) Jordan[3].

a correct calibration. This is still an incorrect calibration, but the effect on the results are minimised when the measurement is close to one of the standards.



**Figure 6.27:** Measured permittivity of water from 100 MHz to 3 GHz using the 7/16-probe with extended centre pin. (a) Measured, (b) Cole-Cole model form literature at 15 °C, (c) 20 °C, (d) 25 °C.

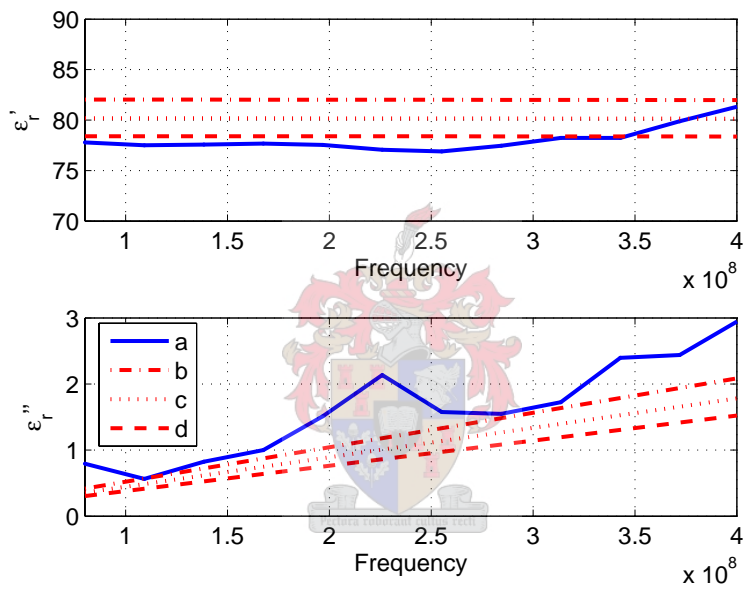


**Figure 6.28:** Measured permittivity of water from 100 MHz to 300 MHz using the 7/16-probe with extended centre pin. (a) Measured, (b) Cole-Cole model form literature at 15 °C, (c) 20 °C, (d) 25 °C.

## Chapter 7

# Conclusion

The project goal set out in chapter 1 was to find and develop a permittivity measurement system that can be used for permittivity measurement of a large variety of permittivity samples over a broad frequency range. It has been shown that the open-ended coaxial probe can measure solids and liquids with dielectric constants ranging from 1 to 80 over more than a decade frequency range. The SMA measurements were seen to deviate less than 3% from values found in literature. These differences are not necessarily measurement errors because variations in manufacturing processes and tolerances and sample quality can also be a source of error. The measurements consisted of both solids and liquids and both were measured to the same degree of accuracy. The permittivity extraction is performed in less than 10 seconds for 101 independent frequency points.

Great improvements have been made to various aspects of the open-ended coaxial probe system to allow fast and accurate permittivity extraction. Part of this thesis was the development of a calculation code in order to calculate the reflection coefficient accurately in a fraction of the time required by other full wave codes. A new model has also been presented that better describes the capacitance behaviour of the open-ended coaxial probe over narrow frequency ranges. This model can be used when extremely fast permittivity extraction is required.

A combination of TRL and SOLT calibration has also been suggested to allow accurate calibration using robust calibration standards. This is a great improvement over previously used calibration schemes where the standards either had to be a perfectly matched termination or a known material. The combination of TRL and SOLT standards also allows the residual errors to be determined and used for uncertainty and error analysis.

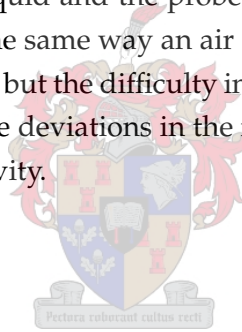


## 7.1 Recommendations

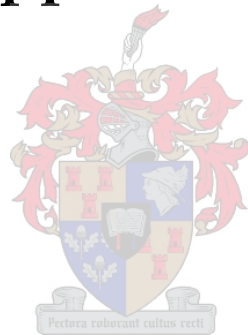
Although great improvements have been made towards the open-ended coaxial probe, some recommendations can be made for future developments.

Calibration of the SMA-probe using TRL standards has allowed accurate data extractions. The frequency range of the TRL calibration is however limited to a 8:1 bandwidth. This bandwidth restriction can be overcome by performing a multi-line TRL calibration. Multi-line TRL calibration does not only increase the measured frequency range but also improves the accuracy of the calibration. It is most accurate when the line length is a quarter wavelength. TRL standards should also be developed for the other probes to allow measurement at lower frequencies. The larger probes would also be less susceptible to errors caused by lift-off.

Liquid samples have been measured with great success, but when corrosive samples have to be measured, it is advisable to protect the probe. This can be done by placing a thin film between the sample liquid and the probe. The series capacitance caused by the film can then be removed in the same way an air gap would be removed. Tests have been performed with plastic films, but the difficulty in applying sufficient and repeatable pressure on the liquid caused large deviations in the measured reflection coefficient and thus also in the extracted permittivity.



# Appendices



# Appendix A

## Calculations

### A.1 Modal analysis of a short cavity termination

Otto and Chew[39] suggested the use of a small shorted cylindrical cavity as an improved calibration standard. Figure A.1 illustrates the configuration of the probe and the shorted cavity. They also presented a modal analysis of the shorted cavity termination to calculate the reflection from the coaxial line. During their derivation they assumed that the permittivity of the dielectric in the coaxial line is identical to the permittivity of the material filling the cavity. It is easy to adapt their solution to find the reflection when the permittivity in the different regions are not the same.

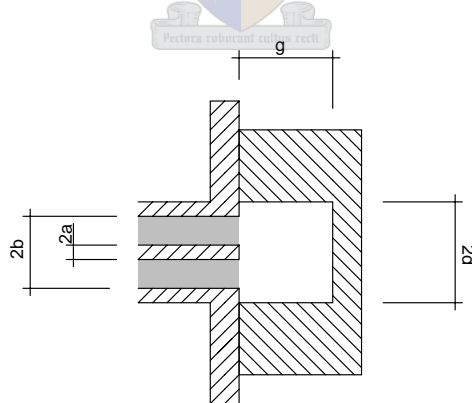


Figure A.1: Illustration of probe with a short cavity termination.

The total magnetic field in the region of the discontinuity with TEM excitation is an infinite sum of incident and reflected axial-symmetric TM modes. The magnetic field can be written in matrix form assuming  $e^{-j\omega t}$  time dependence and is given by (A.1.1) and

(A.1.2). Equation (A.1.1) is the magnetic field inside the coaxial line and (A.1.2) is the magnetic field inside the cylinder.

$$H_\phi(\rho, z)|_{z \leq 0} = \bar{\Phi}^t(\rho) \left( e^{j\mathbf{K}_z z} - e^{j\mathbf{K}_z z} \mathbf{R} \right) \bar{\mathbf{a}} \quad (\text{A.1.1})$$

$$H_\phi(\rho, z)|_{0 \leq z \leq g} = \bar{\Psi}^t(\rho) \left( e^{j\mathbf{K}_{lz} z} - e^{j\mathbf{K}_{lz}(z-2g)} \mathbf{R} \right) \bar{\mathbf{a}} \quad (\text{A.1.2})$$

$\bar{\Phi}^t$  and  $\bar{\Psi}^t$  are real vectors containing the radial dependence of the axial-symmetric TM modes.  $\mathbf{R}$  is the generalised reflection operator for the electric field of the modes in the coaxial line.  $\mathbf{R}_{00}$  is the required TEM reflection from the discontinuity.  $\mathbf{K}_z$  and  $\mathbf{K}_{lz}$  are diagonal matrices with the corresponding wavenumbers for each region. The wavenumbers are give by (A.1.3) and (A.1.4).

$$k_z = \sqrt{k_0^2 - k_{\rho n}^2} \quad (\text{A.1.3})$$

$$k_{lz} = \sqrt{k_1^2 - x_n^2} \quad (\text{A.1.4})$$

The radial function for the dominant TEM mode is given by (A.1.5).

$$\phi_0(\rho) = \frac{c_0}{\rho} \quad (\text{A.1.5})$$

$$c_0 = \frac{1}{\sqrt{\ln(b/a)}} \quad (\text{A.1.6})$$

The radial functions for the higher order  $\text{TM}_{0n}$  modes in the coaxial line are given by (A.1.7).  $J_n$  is the  $n^{\text{th}}$  order Bessel function of the first kind and  $Y_n$  is the  $n^{\text{th}}$  order Bessel function of the second kind. The Bessel function of the second kind is also represented by  $N_n$  in some literature.

$$\phi_n(\rho) = c_n [J_1(k_{\rho n} \rho) Y_0(k_{\rho n} a) - Y_1(k_{\rho n} \rho) J_0(k_{\rho n} a)] \quad (\text{A.1.7})$$

$$c_n = \frac{\pi k_{\rho n}}{\sqrt{2}} \left[ \frac{J_0^2(k_{\rho n} a)}{J_0^2(k_{\rho n} b)} - 1 \right]^{-\frac{1}{2}} \quad (\text{A.1.8})$$

The coaxial guidance condition is used to determine the eigenvalues for the  $\text{TM}_{0n}$  modes ( $n \geq 1$ ).  $\phi_n$  forms an orthonormal set in the coaxial line.

$$Y_0(k_{\rho n} a) J_0(k_{\rho n} b) = J_0(k_{\rho n} a) Y_0(k_{\rho n} b) \quad (\text{A.1.9})$$

The radial functions for the  $\text{TM}_{0n}$  modes in the cylinder is given by (A.1.10). No TEM

mode can exist in the cylinder because the waveguide consists of a single conductor.

$$\psi_n(\rho) = \frac{J_1(x_n\rho)}{\frac{d}{\sqrt{2}}J_1(x_nd)} \quad (\text{A.1.10})$$

The eigenvalues in the cylinder are determined by solving (A.1.11) for  $n \geq 1$ .

$$J_0(x_nd) = 0 \quad (\text{A.1.11})$$

The boundary conditions can now be applied at the interface. The tangential electric and magnetic fields have to be continuous over the aperture of the coaxial line and the tangential electric field has to be zero on the flange. The tangential electric field is found by substituting  $H_\phi(\rho, z)$  into (A.1.12).

$$E_\rho(\rho, z) = \frac{i}{\omega\epsilon} \frac{\partial H_\phi}{\partial z} \quad (\text{A.1.12})$$

The resulting equations are solved by eliminating the the  $\rho$  variable. This is done using the Hankel transform (also known as a Fourier-Bessel transform) given by (A.1.13). The inverse Hankel transform is given by (A.1.14).

$$\tilde{f}(x_n) = \int_0^d \rho J_1(x_n\rho) f(\rho) d\rho \quad (\text{A.1.13})$$

$$f(\rho) = \sum_{n=1}^{\infty} \frac{J_1(x_n\rho)}{\frac{d^2}{2} J_1^2(x_nd)} \tilde{f}(x_n) \quad (\text{A.1.14})$$

Continuity of  $E_\rho$  at  $z = 0$  is used to determine  $\bar{\mathbf{b}}$ .  $\mathbf{R}$  is then solved through continuity of  $H_\phi$  in the aperture. The solution is given by (A.1.15).  $\mathbf{G}$  is a square matrix with the elements given by (A.1.16)

$$\mathbf{R} = (\mathbf{I} + \mathbf{G})^{-1}(\mathbf{I} - \mathbf{G}) \quad (\text{A.1.15})$$

$$\mathbf{G}_{mn} = \sum_{q=1}^{N_{cylin}} \left[ \frac{\epsilon_{cylin}}{\epsilon_{coax}} \left( \frac{\tilde{\Phi}_m(x_q)\tilde{\Phi}_n(x_q)}{\frac{d^2}{2} J_1^2(x_qd)} \right) \frac{\sqrt{k_0^2 - k_{\rho n}^2}}{\sqrt{k_1^2 - x_q^2}} \left( \frac{1 + e^{i2g\sqrt{k_1^2 - x_q^2}}}{1 - e^{i2g\sqrt{k_1^2 - x_q^2}}} \right) \right] \quad (\text{A.1.16})$$

The number of  $\text{TM}_{0n}$  modes inside the cylinder should be more than the number of  $\text{TM}_{0n}$  modes in the coaxial line for the same level of accuracy. Equation (A.1.17) is an approximation to the number of modes used inside cylinder and the coaxial line.

$N_{coax} \geq 15$  has been used and is in good agreement with measurements.

$$N_{cylin} = \frac{N_{coax}d}{b-a} \quad (\text{A.1.17})$$

## A.2 Reflection from a coaxial line terminating in a non-magnetic material

Only the quasi-static solution is presented here. The full wave solution is presented in section 3.3.1 on page 30.

### A.2.1 Quasi-static solution

A quasi-static analysis of an open-ended coaxial line terminated by a semi-infinite medium has been done by Misra[27]. The quasi-static solution by Marcuvitz[26] is valid only for the homogeneous problem and not an open-ended coaxial line open to an arbitrary medium. The analysis is based on a variational formulation of the problem. The normalized admittance of the probe at the interface is calculated without any regard for higher order modes in the coaxial line that could be generated at the interface. This admittance is given by (A.2.1). The primed coordinates represent, as usual, coordinates of the source and the unprimed coordinates represent field points. The wave numbers inside and outside the coaxial line are given by  $k_c = \omega\sqrt{\mu_0\epsilon_0}$  and  $k = \omega\sqrt{\mu_0\epsilon_m}$  respectively.

$$\bar{Y}_L = j \frac{k^2}{\pi k_c \ln(\frac{b}{a})} \int_a^b \int_a^b \int_0^\pi \cos(\phi') \frac{e^{-jkR}}{R} d\phi' d\rho' d\rho \quad (\text{A.2.1})$$

$$R = \sqrt{\rho^2 + \rho'^2 - 2\rho\rho' \cos(\phi')} \quad (\text{A.2.2})$$

The exponent in (A.2.1) can be approximated by the first few terms of a power series[59]. Only the first four terms are considered by Misra. Even these four terms are a good approximation for the quasi-static solution since the quasi-static solution is only valid at frequencies where higher order modes have little effect on the reflection coefficient. At low frequencies the exponent is small and the approximation valid. The second term in the series reduces to zero during integration over  $\phi'$ . The fourth term has an analytical solution for integration and does not need to be calculated numerically. Now only two integrals remain that need to be calculated numerically.

The characteristic admittance of a coaxial line is used to find the admittance at the

interface from the normalised admittance in (A.2.1).

$$Y_L = j \frac{2\omega\epsilon_m}{[\ln(\frac{b}{a})]^2} \left[ I_1 - \frac{k^2 I_3}{2} \right] + \frac{k^3 \pi \omega \epsilon_m}{12} \left[ \frac{b^2 - a^2}{\ln(\frac{b}{a})} \right]^2 \quad (\text{A.2.3})$$

$$I_1 = \int_a^b \int_a^b \int_0^\pi \frac{\cos(\phi')}{R} d\phi' d\rho' d\rho \quad (\text{A.2.4})$$

$$I_3 = \int_a^b \int_a^b \int_0^\pi \cos(\phi') R d\phi' d\rho' d\rho \quad (\text{A.2.5})$$

The integrals  $I_1$  and  $I_3$  need to be calculated numerically, but they only need to be calculated once for a specific probe since they are dependent only on the dimensions of the probe.  $I_1$  has a singularity when  $\phi = 0$  and  $\rho = \rho'$ . The time required for calculation can be reduced greatly by removing this singularity. This has been done in [60], resulting in (A.2.6).  $K$  is the complete elliptic integral of the first kind that can be approximated by a polynomial [61, page 591] for fast and accurate calculation.

$$I_1 = 2 \int_a^b \int_a^b \frac{K(p^2)}{\rho + \rho'} d\rho' d\rho + \int_a^b \int_a^b \int_0^\pi \frac{\cos(\phi') - 1}{R} d\phi' d\rho' d\rho \quad (\text{A.2.6})$$

$$p^2 = \frac{4\rho\rho'}{(\rho + \rho')^2} \quad (\text{A.2.7})$$

The polynomial approximation for  $K$  is repeated here. The values for  $a_n$  and  $b_n$  are listed in Table A.1. This approximation is valid for  $0 \leq m < 1$  and is in error by less than  $2 * 10^{-8}$ .

$$K(m) = [a_0 + a_1 m_1 + a_2 m_1^2 + a_3 m_1^3 + a_4 m_1^4] + \dots \quad (\text{A.2.8})$$

$$\ln\left(\frac{1}{m_1}\right) [b_0 + b_1 m_1 + b_2 m_1^2 + b_3 m_1^3 + b_4 m_1^4] \quad (\text{A.2.9})$$

$$m_1 = 1 - m \quad (\text{A.2.9})$$

**Table A.1:** Coefficients used to approximate the elliptic integral of the first kind.

<b>n</b>	<b>0</b>	<b>1</b>	<b>2</b>	<b>3</b>	<b>4</b>
$a_n$	1.38629436112	0.09666344259	0.03590092383	0.03742563713	0.01451196212
$b_n$	0.5	0.12498593597	0.06880248576	0.03328355346	0.00441787012

### A.3 Equations for direct permittivity extraction

The equation presented here can be used as a fast approximation to the full wave solution. These equations are only valid for relatively narrow frequency ranges. The frequency range limitation becomes greater with an increase in centre frequency. This is explained fully in section 3.3.2 on page 36. The parameters of the equations should be determined through a least squares fit of the equation to the reflection from a full wave solution over the required frequency range.

#### A.3.1 Quasi-static

The quasi-static solution has been reduced to a polynomial in permittivity. The permittivity is determined by solving the equations (A.3.3) and (A.3.4).

$$A = \frac{2\omega\epsilon_0 I_1}{\ln^2(b/a)} \quad (\text{A.3.1})$$

$$B = \frac{\omega^2\epsilon_0\mu_0 I_3}{2I_1} \quad (\text{A.3.2})$$

$$\epsilon_r'' = \sqrt{\frac{Y_i}{2AB} - \frac{1}{8B^2} + \sqrt{\left(\frac{A}{4B}\right)^2 - \frac{Y_i A}{2B} + Y_r^2 + \frac{Y_i^2}{4A^2 B^2}}} \quad (\text{A.3.3})$$

$$\epsilon_r' = \frac{1}{2B} + \sqrt{\left(\frac{1}{2B}\right)^2 - \frac{Y_i}{AB} - \epsilon_r''^2} \quad (\text{A.3.4})$$

$$\epsilon_m = \epsilon_0(\epsilon_r' - j\epsilon_r'') \quad (\text{A.3.5})$$

#### A.3.2 Constant fringing capacitance

This simple equivalent circuit allows rapid permittivity calculation using the Deschamps antenna modelling theorem. The circuit can be used with and without the radiation conductance.

The inversion without the radiation conductance is simple and was first suggested by Stuchly[32]. The unknown variables are determined using a least squares fit of the model to one of the full wave solutions at a particular frequency. The equations for permittivity



is given by (A.3.6) and (A.3.7).

$$\epsilon'' = \frac{-2\Gamma \sin \phi}{\omega C_0 Z_0 (1 + 2\Gamma \cos \phi + \Gamma^2)} - \frac{C_f}{C_0} \equiv A \quad (\text{A.3.6})$$

$$\epsilon' = \frac{1 - \Gamma^2}{\omega C_0 Z_0 (1 + 2\Gamma \cos \phi + \Gamma^2)} \equiv B \quad (\text{A.3.7})$$

Stuchly *et al.*[32] also derived a way to incorporate the radiation into the model. This relies on an iterative solution, but should be fast on any personal computer. The procedure is described by Equations (A.3.6) through (A.3.13).

$$\epsilon'' = A - \frac{G_r b}{\omega C_0} \quad (\text{A.3.8})$$

$$\epsilon' = B - \frac{G_r g}{\omega C_0} \quad (\text{A.3.9})$$

$$g = \epsilon'^{5/2} [\alpha (1 - \tan^2 \delta) - 2\beta \tan \delta] \quad (\text{A.3.10})$$

$$b = -\epsilon'^{5/2} [\alpha (1 - \tan^2 \delta) + 2\beta \tan \delta] \quad (\text{A.3.11})$$

$$\alpha = \sqrt{\frac{\sqrt{1 + \tan^2 \delta} + 1}{2}} \quad (\text{A.3.12})$$

$$\beta = \sqrt{\frac{\sqrt{1 + \tan^2 \delta} - 1}{2}} \quad (\text{A.3.13})$$

Stuchly found that including the radiation term greatly improves the extraction accuracy and should be included for accurate results. The model is fast and easy to implement, but requires a full wave solution to determine the model parameters.

### A.3.3 Four capacitor model

The four capacitor model was shown to be only a slight improvement over the constant fringing capacitor model and thus is not recommended. The inversion equations are included here for completeness and because they were not given by Stuchly[33].

The capacitance in (3.3.25) is of a lossy capacitor. The capacitance is written as an

admittance.

$$Y = j\omega \left( C_{fp} + C_0\epsilon_m + \frac{C_{fs1}\epsilon_m}{1 + \frac{\epsilon_m C_{fs1}}{C_{fs2}}} \right) \quad (\text{A.3.14})$$

The material permittivity can now be found by solving the second order polynomial. The solution is shown in (A.3.18).

$$A = C_0 \quad (\text{A.3.15})$$

$$B = C_{fp} + C_{fs2} \left( 1 + \frac{C_0}{C_{fs1}} + \frac{jY}{\omega} \right) \quad (\text{A.3.16})$$

$$C = \frac{C_{fs2}}{C_{fs1}} \left( C_{fp} + \frac{jY}{\omega} \right) \quad (\text{A.3.17})$$

$$\epsilon_m = \frac{-B + \sqrt{B^2 - 4AC}}{2A} \quad (\text{A.3.18})$$

The second root gives negative real permittivity and thus is not valid for a real world solution.

#### A.3.4 New model

This function has been shown to fit the impedance of the open-ended coaxial line the best. Once again the capacitance is written as an admittance and rewritten so that the sample permittivity is the subject of the function. The admittance is shown in (A.3.19) and the resulting equation for the sample permittivity is given by (A.3.20).

$$Y = j\omega \left( \epsilon_c C_f + \epsilon_m C_0 + \frac{C_2}{k + \epsilon_m} \right) \quad (\text{A.3.19})$$

$$\epsilon_m = 0.5 \sqrt{(kC_0)^2 + C_f^2 + \frac{j2Y(C_f - kC_0)}{\omega} - 2C_0(kC_f + 2C_2) - \left( \frac{Y}{\omega} \right)^2} - 0.5 \left( C_f + kC_0 + \frac{jY}{\omega} \right) \quad (\text{A.3.20})$$

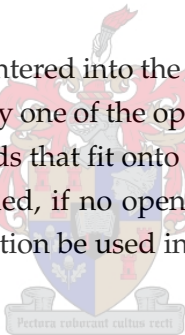
# Appendix B

## Tables & Data

### B.1 Calibration Definitions

#### B.1.1 SOL

The calibration definitions that are entered into the 8510c VNA to describe the three SOL standards are listed in Table B.1. Only one of the open standards are used during calibration, but for convenience all standards that fit onto the probes can be used. A calibration for the probes into air is also included, if no open standard is available. It is however recommended that a two-tier calibration be used instead of the on-line VNA calibration.



#### B.1.2 TRL

The SMA TRL standards have been designed to work from 1 GHz to 8 GHz. TRL calibration requires little information from the user. The line and reflect standard only have to be defined approximately. The line standard is 11.5 mm long and has a propagation delay of 54 ps. The reflect standards are described to within a quarter wavelength by a 29.8 pF capacitor.

**Table B.1:** SOL Calibration Definitions for 8510c VNA

<b>Standard</b>	<b>Coefficient</b>	<b>SMA</b>	<b>N</b>	<b>7/16</b>
<b>Load</b>		50 $\Omega$	50 $\Omega$	50 $\Omega$
<b>Short</b>	L0	0	0	0
	L1	0	0	0
	L2	0	0	0
	L3	0	0	0
<b>Open SMA</b>	C0	32.5535	n.a.	n.a.
	C1	0.2961	n.a.	n.a.
	C2	4.5108	n.a.	n.a.
	C3	0.0195	n.a.	n.a.
<b>Open N</b>	C0	29.7496	81.5413	n.a.
	C1	2.1404	11.0685	n.a.
	C2	5.8778	65.0268	n.a.
	C3	0.1273	1.4229	n.a.
<b>Open 7/16</b>	C0	29.7809	74.4939	125.8974
	C1	-0.7997	47.2092	22.1255
	C2	8.3704	70.4296	254.1688
	C3	-0.0572	5.3971	8.4206
<b>Air</b>	C0	29.7809	73.4741	115.2859
	C1	-0.7997	-45.6163	-239.1596
	C2	8.3704	148.7223	580.7292
	C3	-0.0572	-4.2619	-27.8177

# Bibliography

- [1] J. P. Grant, R. N. Clarke, G. T. Symm, and N. M. Spyrou, "A critical study of the open-ended coaxial line sensor technique for RF and microwave complex permittivity measurements," *J. Phys. E: Sci. Instrum.*, vol. 22, no. unknown, pp. 757–770, 1989.
- [2] N. Belhadj-Tahar, O. Meyer, and A. Fourier-Lamer, "Broadband microwave characterisation of bilayered materials using a coaxial discontinuity with application for thin conductive films for microelectronics and material in air-tight cell," *IEEE Transactions on Microwave Theory and Techniques*, vol. 45, no. unknown, pp. 260–267, 1997.
- [3] B. P. Jordan, R. J. Sheppard, and S. Szwarnowski, "The dielectric properties of formamide, ethonedia and methanol," *J. Phys. D: Appl. Phys.*, vol. 11, no. unknown, pp. 695–701, 1978.
- [4] H. A. Haus and J. R. Melcher, *Electromagnetic Fields and Energy*, 1st ed. Prentice-Hall, 1988.
- [5] R. Coelho, *Physics of dielectrics for the Engineer*, 1st ed. Elsevier Scientific Publishing Company, 1979.
- [6] A. R. von Hippel, *Dielectrics and Waves*. Artech House, 1995.
- [7] S. Ramo, J. R. Whinnery, and T. V. Duzer, *Fields and Waves in Communication Electronics*, 3rd ed. John Wiley & Sons, Inc., 1994.
- [8] M. Rimbi, "Wood microwave dielectric heating and measurement of material properties," Ph.D. dissertation, University of Stellenbosch, South Africa, 2004.
- [9] D. M. Pozar, *Microwave Engineering*, 3rd ed. John Wiley & Sons, Inc., 2005.
- [10] A. R. von Hippel, *Dielectric materials and applications*, 3rd ed. M.I.T. Press, 1961.
- [11] R. E. Diàz, "An analytic continuation method for the analysis and design of dispersive materials," *IEEE Transactions on Antennas and Propagation*, vol. 45, no. 11, pp. 1602–1610, 1997.
- [12] N. Braithwaite and G. Waver, *Electronic Materials inside electronic devices*, 2nd ed. Butterworth-Heinemann, 1998.

- [13] K. S. Cole and R. H. Cole, "Dispersion and absorption in dielectrics," *Journal of Chemical Physics*, vol. 9, no. unknown, pp. 341–351, 1941.
- [14] J. Baker-Jarvis, M. D. Janezic, J. H. Grosvenor, and R. G. Geyer, "Transmission/reflection and short-circuit line methods for measuring permittivity and permeability: Technical note 1355-r," National Institute of Standards and Technology, Tech. Rep., 1994.
- [15] M. R. Taherian, W. E. Kenyon, and K. A. Safinya, "Measurement of dielectric response of water-saturated rocks," *Geophysics*, vol. 55, no. 12, pp. 1530–1541, 1990.
- [16] J. Baker-Jarvis, C. Jones, B. Riddle, M. Janezic, R. G. Geyer, J. H. Grosvenor, and C. M. Weil, "Dielectric and magnetic measurements: A survey of nondestructive, quasi-nondestructive, and process-control techniques," *American Society for Nondestructive Testing*, vol. 7, p. 117 136, 1995.
- [17] "Basics of measuring the dielectric properties of materials." [Online]. Available: <http://www.agilent.com>
- [18] G. Roussy and J. Pearce, *Foundations and industrial applications of microwaves and radio frequency fields : Physical and Chemical Processes*, 1st ed. John Wiley & Sons, Inc., 1995.
- [19] M. Afsar, J. Birch, R. Clarke, and G. Chantry, "The measurement of the properties of materials," *Proceedings of the IEEE*, vol. 74, no. 1, pp. 183–199, 1986.
- [20] H. Bussey, "Measurement of RF properties of materials: A survey," *Proceedings of the IEEE*, vol. 55, no. 6, pp. 1046–1053, 1967.
- [21] M. Rütshlin, "The non-destructive measurement of the radio frequency properties of hard rock borehole cores," Ph.D. dissertation, University of Stellenbosch, South Africa, 2005.
- [22] M. A. Stuchly and S. S. Stuchly, "Coaxial line reflection methods for measuring dielectric properties of biological substrates at radio and microwave frequencies - a review," *IEEE Transactions on Instrumentation and Measurement*, vol. 29, no. 3, pp. 176–183, 1980.
- [23] E. C. Burdette, F. L. Cain, and J. Seals, "In vivo probe measurement technique for determining dielectric properties at VHF through microwave frequencies," *IEEE Transactions on Microwave Theory and Techniques*, vol. 28, no. 4, pp. 414–427, 1980.
- [24] G. A. Deschamps, "Impedance of an antenna in a conducting medium," *IRE Transactions of Antennas and Propagation*, pp. 648–650, 1962.
- [25] R. Olmi, G. Pelosi, C. Riminesi, and M. Tedesco, "A neural network approach to real-time dielectric characterization of materials," *Microwave and Optical Technology Letters*, vol. 35, no. 6, pp. 463–465, 2002.

- [26] N. Marcutitz, *Waveguide Handbook*, 1st ed. Peter Peregrinus Ltd., London, UK, 1951.
- [27] D. K. Misra, "A quasi-static analysis of open-ended coaxial lines," *IEEE Transactions on Microwave Theory and Techniques*, vol. 35, no. 10, pp. 925–928, 1987.
- [28] J. R. Mosig, J. E. Besson, M. Gex-Fabry, and F. E. Gardiol, "Reflection of an open-ended coaxial line and application to nondestructive measurement of materials," *IEEE Transactions on Instrumentation and Measurement*, vol. 30, no. 1, pp. 46–51, 1981.
- [29] J. Baker-Jarvis, C. Jones, M. D. Janezic, R. G. Geyer, and P. D. Domich, "Analysis of an open-ended coaxial probe with lift-off for nondestructive testing," *IEEE Transactions on Instrumentation and Measurement*, vol. 43, no. 5, pp. 711–718, 1994.
- [30] G. B. Gajda and S. S. Stuchly, "Numerical analysis of open-ended coaxial lines," *IEEE Transactions on Microwave Theory and Techniques*, vol. 31, no. 5, pp. 380–384, 1983.
- [31] P. D. Langhe, L. Martens, and D. D. Zutter, "Design rules for an experimental setup using an open-ended coaxial probe based on theoretical modeling," *IEEE Transactions on Instrumentation and Measurement*, vol. 43, no. 6, pp. 810–817, 1994.
- [32] M. A. Stuchly, M. M. Brady, S. S. Stuchly, and G. Gajda, "Equivalent circuit of an open-ended coaxial line in a lossy dielectric," *M.I.T. Press*, vol. 31, no. 2, pp. 116–119, 1982.
- [33] G. Gajda and S. S. Stuchly, "An equivalent circuit of an open-ended coaxial line," *M.I.T. Press*, vol. 32, no. 4, pp. 506–508, 1983.
- [34] S. S. Stuchly, C. L. Sibbald, and J. M. Anderson, "A new aperture admittance model for open-ended waveguides," *IEEE Transactions on Microwave Theory and Techniques*, vol. 42, no. 2, pp. 192–198, 1994.
- [35] J. M. Anderson, C. L. Sibbald, and S. S. Stuchly, "Dielectric measurements using a rational function model," *IEEE Transactions on Microwave Theory and Techniques*, vol. 42, no. 2, pp. 199–204, 1994.
- [36] "Root-finding algorithm: Secant method," wikipedia, the free encyclopedia. [Online]. Available: [http://en.wikipedia.org/wiki/Secant\\_method](http://en.wikipedia.org/wiki/Secant_method)
- [37] H. Jasik, *Antenna engineering handbook*, 1st ed. McGraw-Hill, 1961.
- [38] L. O. Chua, C. A. Desoer, and E. S. Kuh, *Linear and Nonlinear Circuits*, 1st ed. McGraw-Hill, 1987.
- [39] G. P. Otto and W. C. Chew, "Improved calibration of a large open-ended coaxial probe for dielectric measurements," *IEEE Transactions on Microwave Theory and Techniques*, vol. 40, no. 4, pp. 742–746, 1991.
- [40] I. J. Bahl and S. S. Stuchly, "Effect of finite size ground plane on the impedance of a monopole immersed in a lossy medium," *Electronic Letters*, vol. 15, no. 22, pp. 728–729, 1979.

- [41] M. Arai, J. G. P. Minner, and T. E. Cross, "Estimating errors due to sample surface roughness in microwave complex permittivity measurements obtained using a coaxial probe," *Electronic Letters*, vol. 31, no. 2, pp. 115–117, 1995.
- [42] "Specifying calibration standards for the agilent 8510 network analyzer," Application Note 8510-5B. [Online]. Available: <http://www.agilent.com>
- [43] "Network analyzer error models and calibration methods," Agilent Presentation.
- [44] G. Kwan, "Sensitivity analysis of one-port characterized devices in vector network analyzer calibrations: Theory and computational analysis," 2002, presented at 2002 NCSL International Workshop and Symposium.
- [45] Y.-Z. Wei and S. Sridhar, "Radiation-corrected open-ended coax line technique for dielectric measurements of liquids up to 20 GHz," *IEEE Transactions on Microwave Theory and Techniques*, vol. 39, no. 3, pp. 526–531, 1991.
- [46] D. K. Misra, M. Chhabra, B. R. Epstein, M. Mirotznik, and K. R. Foster, "Noninvasive electrical characterization of materials at microwave frequencies using an open-ended coaxial line: Test of an improved calibration technique," *IEEE Transactions on Microwave Theory and Techniques*, vol. 38, no. 1, pp. 8–14, 1990.
- [47] G. F. Engen and C. A. Hoer, "'thru-reflect-line': An improved technique for calibrating the dual six-port automatic network analyser," *IEEE Transactions on Microwave Theory and Techniques*, vol. 27, no. 12, pp. 987–993, 1979.
- [48] "Agilent network analysis applying the 8510 TRL calibration for non-coaxial measurements," Application Note 8510-8A. [Online]. Available: <http://www.agilent.com>
- [49] U. Stamper, "Uncertainty of VNA S-parameter measurement due to nonideal TRL calibration items," *IEEE Transactions on Microwave Theory and Techniques*, vol. 54, no. 2, pp. 676–679, 2005.
- [50] "Applying error correction to network analyzer measurements," Application Note 8510-AN1287-3. [Online]. Available: <http://www.agilent.com>
- [51] "Defining and verifying solt calibration standards," HF Measurements 813 Course Notes.
- [52] "Verifying the performance of vector network analyzers." [Online]. Available: <http://www.maurymw.com>
- [53] "Expression of uncertainty of measurement in calibration: Reference ea-4/02," 1999. [Online]. Available: <http://www.european-accreditation.org>
- [54] B. N. Taylor and C. E. Kuyatt, "Guidelines for evaluating and expressing the uncertainty of NIST measurement results: Technical note 1297," National Institute of Standards and Technology, Tech. Rep., 1994.



- [55] "HP 8510c user manual," Performance Verification and Specification.
- [56] C. Fouché, "S-band meting van die permittiwiteit van poliëster," 2005, Internal Report to GeoMole.
- [57] "Symalit PVDF," 2003. [Online]. Available: <http://www.symalit.com>
- [58] W. J. Ellison, K. Lamkaouchi, and J. M. Moreau, "Water: A dielectric reference," *Journal of Molecular Liquids.*, vol. 68, pp. 171–279, 1996.
- [59] M. R. Spiegel and J. Liu, *Mathematical handbook of Formulas and Tables*, 2nd ed. McGraw-Hill, 1999.
- [60] L. L. Tsai, "A numerical solution for the near and far fields of an annular ring of magnetic current," *IEEE Transactions on Antennas and Propagation*, vol. 20, no. 5, pp. 569–576, 1972.
- [61] M. Abramowitz and I. A. Stegun, *Handbook of Mathematical Functions*, 1st ed. Dover Publications, Inc., 1965.

